Universiteit Antwerpen

Faculteit Wetenschappen
Departement Chemie

Mathematical Simulation of the Deposition of Diamond-like carbon (DLC) Films

Wiskundige Simulatie van de Depositie van Diamond-like carbon (DLC) Filmen

Proefschrift voorgelegd tot het behalen van de graad van doctor in de Wetenschappen aan de Universiteit Antwerpen te verdedigen door

Erik NEYTS

Promotor: Prof. Dr. Annemie Bogaerts

Antwerpen, 2006

Contents

Acknowledgments **xvii**

1 Amorphous (hydrogenated) Carbon **1**

1.1 Structure and terminology 1

1.2 Current understanding of the deposition mechanism 3

1.3 Properties and applications 7

1.4 Deposition techniques 9

1.4.1 Ion beam deposition 9

1.4.2 Mass selected ion beam deposition 10

1.4.3 Sputter deposition 11

1.4.4 Plasma enhanced chemical vapor deposition 11

1.4.5 The expanding thermal plasma 13

1.5 Simulation techniques 15

1.5.1 Quantum-based simulations 16

1.5.2 Molecular dynamics simulations 17

1.5.3 Monte Carlo simulations 19

2 MD simulation techniques **21**

2.1 Introduction 21

2.2 Elements of Molecular Dynamics 23

2.2.1 Introduction 23

2.2.2 Classical dynamics 23

2.2.3 Statistical mechanics 24
2.2.4 Interatomic potentials 26
2.2.5 Numerical integration 28
2.2.6 Temperature control 29
2.2.7 Periodic boundaries 31
2.3 The Brenner potential 33
2.3.1 Functional form of the Brenner potential 33
2.3.2 Disadvantages of the Brenner potential 42
2.4 Validation of the interatomic potential implementation in the model 45
2.4.1 Atomization energies 45
2.4.2 Conservation of energy 47
2.4.3 Chemisorption 52
2.4.4 Bond energies and bond lengths 53
2.5 Methodology for simulating thin film growth 54
2.6 Speeding up the code 59
2.7 Aim of this work and structure of the thesis 61

3 Initial simulation of the growth of a-C:H films from hydrocarbon radicals 65
3.1 Introduction 66
3.2 Results and discussion 69
3.2.1 General microscopic structure of the deposited films 69
3.2.2 Coordination in the films and mechanisms of film growth . . 70
3.2.3 The Radial Distribution Function 76
3.2.4 Hydrogen content of the films 79
3.2.5 Density of the films 79
3.3 Conclusion 81

4 **Reaction mechanisms of a-C:H growth precursors on selected a-C:H sites** **85**

4.1 Introduction 86

4.2 Results and discussion 88

4.2.1 Sites O_1, O_2 and O_3 88

4.2.2 Sites O_4 and O_5 96

4.2.3 Site O_6 99

4.2.4 Sites O_7 and O_8 101

4.2.5 Site O_9 103

4.2.6 Sites O_{10} and O_{11} 106

4.3 Conclusion 110

5 **Influence of internal energy and impact angle on the reaction mechanisms for a-C:H growth precursors** **113**

5.1 Introduction 114

5.2 Results and discussion 116

5.2.1 Effect of the internal energy 116

5.2.2 Effect of the impact angle 120

5.3 Conclusion 120

6 **Reaction behaviour of linear and cyclic C_3 and C_3H radicals and simulation of a-C:H film growth due to these species** **123**

6.1 Introduction 124

6.2 Results and discussion 127

6.2.1 Calculated film properties 127

6.2.2 Deposition characteristics of the *l*-C_3, *c*-C_3, *l*-C_3H and *c*-C_3H radicals 132

6.3 Conclusion 138

7 Influence of the H-flux on thin a-C:H film growth under $F < 1$ conditions 141

7.1 Introduction . . . 142

7.2 Results and discussion . . . 143

7.3 Conclusion . . . 149

8 Generalized effect of an additional H-flux, as well as a C-fluxes on the growth of thin a-C:H films, under $F \geq 1$ conditions 151

8.1 Introduction . . . 152

8.2 Results and discussion . . . 154

8.2.1 Simulation set 1: Influence of the H-flux without additional C-flux . . . 154

8.2.2 Simulation set 2: Influence of the H-flux with additional C-flux of 10% . . . 160

8.3 Conclusion . . . 162

9 General conclusions 165

Summary 171

Samenvatting 175

List of Publications 179

Contribution to conferences 181

List of Figures

1.1 The sp^3, sp^2 and sp carbon hybridisations. 2
1.2 Ternary phase diagram of amorphous carbon-hydrogen structures [1]. 4
1.3 Schematic representation of the deposition processes in a-C:H film growth [2]. DB stands for dangling bond. The open circles represent H atoms, and the filled circles represent C atoms. 5
1.4 Schematic drawing of the Expanding Thermal Plasma set-up. . . . 14
1.5 Comparison among the different simulation techniques used for thin film growth, in terms of time and length scales. 18

2.1 Periodic boundary conditions for the two-dimensional case. 31
2.2 The minimum image criterion. 32
2.3 Cutoff functions for the C-C interaction of Brenner (dashed line) and Murty-Atwater(full line). 35
2.4 Number of citations to the most popular carbon potentials since their publication. 44
2.5 Napthalene, and the time evolution of its total energy, potential energy and temperature. 49
2.6 Diamond {111} surface, and the time evolution of its total energy, potential energy and temperature. 50
2.7 Diamond {111} surface passivated with H, and the time evolution of its total energy, potential energy and temperature. 50

2.8 a-C:H surface, and the time evolution of its total energy, potential energy and temperature. 51

2.9 Impact of a 10eV CH_3 radical on an a-C:H surface, and the time evolution of its total energy, potential energy and temperature. . . . 52

2.10 Diamond {111} substrate, containing 728 atoms (lefthand side), and a thin a-C:H layer, containing 1000 atoms (righthand side). The grey {x,y}-planes are the periodic boundaries. Blue balls are 4-coordinated C-atoms, red balls, green balls and yellow balls are 3-, 2- and 1-coordinated C-atoms, respectively, and the small grey balls are H-atoms. 56

2.11 Flow-chart representing the basis execution of an MD program. . . 58

2.12 Effect of speeding up the code, using the cell-method and the split-method (see text). The calculation time (in hours) reflects the time needed to simulate the deposition of 2188 atoms initiated on a 500 atom substrate on a single AMD Athlon MP 2600+ processor. . . . 60

3.1 Side view of the simulated films for condition 1 (figure 1a) and condition 2 (figure 1b). It can be seen that the film of condition 1 shows fewer voids in its structure, and contains a much higher fraction of 4-fold coordinated carbon atoms, as compared to the film of condition 2. 70

3.2 Calculated fraction of 4-fold coordinated carbon atoms for condition 1 (dashed line) and condition 2 (solid line) as a function of position in the film. The initial substrate on which the film was grown starts at 0.0 Å, and extends to the left (not shown). 71

3.3 Calculated sticking and desorption efficiencies of the main growth species under condition 1 (left panel) and condition 2 (right panel). The black areas indicate the sticking efficiencies, the dark grey areas indicate the etching efficiencies, and the light grey areas indicate the fraction of events where neither sticking nor etching occurred. Only the species with a high sticking efficiency are shown. 74

3.4 Calculated contribution of the different species to the growth of the film, in terms of the fraction of carbon atoms and hydrogen atoms added to the film by each species, under condition 1 (left panel) and condition 2 (right panel). 75

3.5 Calculated 4-4 RDF for film 1 (dashed line) and film 2 (solid line). . 77

3.6 Calculated total carbon-carbon RDF for film 1 (dashed line) and film 2 (solid line). The H-atoms are not included in this RDF. . . . 78

3.7 Calculated H-fractions for film 1 (dashed line) and film 2 (solid line), as a function of position in the film. The initial substrate starts at 0.0 Å, and extends to the left (not shown). 80

3.8 Calculated density for film 1 (dashed line) and film 2 (solid line), as a function of position in the film. The initial substrate starts at 0.0 Å, extending to the left (not shown). 81

4.1 Schematic representation of the sites studied in this work. The 11 impact locations are denoted as O_1 to O_{11}. Locations O_7 and O_8, and O_{10} and O_{11} share the same site, but the impact position of the hydrocarbon radical on the site is different. The exact impact location is indicated by the arrows. The dots in the figure indicate surface carbon atoms, and the wavy lines symbolize dangling bonds. 87

4.2 Resonance contributors for the C_2 radical after sticking to the surface. The sp^2 resonance contributor (a) shifts towards the sp contributor (b) after sticking. 92

4.3 Evolution of the binding energy between a surface atom and an impinging C_2 radical (C_S-C), and the change from a double C-C bond in C_2 before the impact ($\sim$ 6 eV) to a triple C-C bond after the impact ($\sim$ 7.8 eV). 92
4.4 Bridge formation upon impact and sticking of a l-C_3H radical. The main resonance contributor (in the brackets) is on the top-right. . 95
4.5 Schematic representation of the sticking and break-up mechanism of the c-C_3H radical, leaving the surface binding atom 3-coordinated. 96

5.1 Calculated accumulated sticking coefficients for the C_3H radical at an impact angle of 0°, for different internal energies (top). Also shown is the procentual difference between the running accumulated sticking coefficient and the final value after 500 impacts (bottom). The dashed horizontal lines denote the ± 5% boundaries, and the full horizontal lines the ± 2% boundaries. The final sticking coefficients for the different energies are given in Fig. 5.2. 116
5.2 Calculated sticking coefficients of the different species as a function of their internal energy (in the legend given in eV), distributed among vibrational and rotational motion. 117
5.3 Calculated fraction of sticking radicals that break up upon impact for different internal energies (in eV). 119
5.4 Calculated sticking coefficients of the different species as a function of their impact angle. 121

6.1 Calculated structure of film 1. The lefthand side shows the total structure. The righthand side shows two regions in detail, illustrating different structural properties. 128
6.2 Average carbon coordination number Z_C as a function of the film thickness. 130
6.3 Calculated C-C coordination numbers in the five films. 131

6.4 Calculated fractions of C-C bonds with certain energy, relative to the total number of C-C bonds, in the five structures. 131

6.5 Time evolution of the bond energies in the C_3H radical upon impact and sticking on the surface. 134

6.6 Schematic representation of the sticking and breaking up of an impacting cyclic C_3 radical. In this illustration, the C_1-C_3 bond breaks up, but obviously the C_1-C_2 or C_2-C_3 bonds can also break up upon impact. 136

7.1 Calculated hydrogen distribution among the C-atoms as a function of the H content in the film; the calculated H content in the films as a function of the H-flux is shown in the inset. 144

7.2 Calculated mass densities and atom densities as a function of the H content in the films. 146

7.3 Calculated sp^1, sp^2 and sp^3 C-fractions as a function of the H-content in the films. 147

7.4 Calculated sticking coefficients of the various C-containing growth species, as a function of the H-content in the films. 148

8.1 Calculated H content in the simulated films as a function of the H-flux towards the substrate, with and without additional C-flux. . 154

8.2 Calculated mass densities of the simulated films as a function of the H-flux towards the substrate, with and without additional C-flux. . 155

8.3 Calculated average C-C bond energy (BE) and average C-coordination number in the different simulated films, as a function of the H-flux towards the substrate, with and without additional C-flux. 157

8.4 Calculated C-C coordination numbers of the different films, for different H-fluxes towards the substrate (as given in the legend), without additional C-flux. The bars show the fraction of m-coordinated C-atoms connected to n-coordinated C-atoms. The values on the abscissa denote m and n. 158

8.5 Calculated fraction of C-C bond energies in the different films, for different H-fluxes towards the substrate (as given in the legend), without additional C-flux. The bin interval is 0.5 eV. 158

8.6 Calculated fractions of sp-type, sp^2-type and sp^3-type carbon atoms in the films, as a function of the H-flux towards the substrate, with and without additional C-flux. Here, the sp-hybridisation is identified with 1- and 2-coordinated C-atoms. Likewise, 3-coordinated C-atoms are denoted here as sp^2 and 4-coordinated C-atoms are denoted as sp^3 C-atoms. 159

8.7 Calculated fractions of C, CH and CH_2 fragments in the films as a function of the H-flux towards the substrate, with and without additional C-flux. 160

8.8 Schematic picture of the structure of three simulated films. For the sake of clarity, only a representative part of the films is shown. The red balls are three-coordinated C-atoms, and the green balls are two-coordinated C-atoms. Four-coordinated C-atoms appear to be absent. The small grey balls represent H-atoms. 162

List of Tables

2.1 Two-body parameters in Brenner's hydrocarbon potential. 38

2.2 Values of F_{CC} at integer points. The integer points (x, y, z) denote N^t_{ij}, N^t_{ji} and N^{conj}_{ij} from eq. 2.18, respectively. $F_{CC}(x, y, z) = F_{CC}(y, x, z)$ and $F_{CC}(x, y, z > 2) = F_{CC}(x, y, z = 2)$. All values not given are 0. Derivatives (required for tricubic interpolation) are found by 2^{nd} order finite differences. 39

2.3 Values of H_{CC} and H_{CH} at integer points. The integer points (x, y) denote N^H_{ij} and N^C_{ji} from eq. 2.19, respectively. All values not given are 0. Derivatives (required for bicubic interpolation) are found by 2^{nd} order finite differences. 40

2.4 Parameters for the repulsive spline function. 41

2.5 Calculated atomization energies for various hydrocarbon molecules (in eV), and the values reported by Brenner [3]. Also given are the experimental values. 46

2.6 Chemisorption energy values (in eV) on a diamond {111} surface for several species. 53

2.7 Calculated C-C bond lengths (in Å) of the chemisorbed species from Table 2.6. 53

2.8 Calculated bond energies (*BE*) and bond lengths (*BL*) for basic hydrocarbons and for diamond, and the corresponding values as reported by Brenner [3]. Bond energies are expressed in eV, and bond lengths in Å. 55

3.1 Species, fluxes and energies of particles arriving at the substrate for both conditions, adopted from the experiments. 67
3.2 Calculated occurrence of rings for both conditions. 71
3.3 Calculated CH_x fractions in both films. 80

4.1 Main resonance contributors for the species investigated. 88
4.2 The investigated species and their calculated binding energies. The carbon atom to which the H-atom of the radical is bound, is denoted as C_3 in the *l*-C_3H radical and as C_1 in the *c*-C_3H radical. Note that the binding energy of a single, double and triple C-C bond typically corresponds to -3.60 eV, -6.36 eV and -8.70 eV, respectively. 89
4.3 Calculated sticking and reflection coefficients, and sticking structures on sites O_1 and O_2. 90
4.4 Calculated sticking and reflection coefficients, and sticking structures on sites O_4 and O_5. 97
4.5 Calculated sticking and reflection coefficients, and sticking structures on site O_6. 100
4.6 Calculated sticking and reflection coefficients, and sticking structures on sites O_7 and O_8. 102
4.7 Calculated sticking and reflection coefficients, and sticking structures on site O_9. 104
4.8 Calculated sticking and reflection coefficients, and sticking structures on sites O_{10} and O_{11}. 107

6.1 Relative fluxes of the different growth species in the five films. . . . 125

6.2 Calculated mass density, average carbon coordination number, sp and sp^2 content of the five films. 129

6.3 Calculated sticking coefficients of the simulated species. 133

7.1 Relative fluxes for the different C-containing growth species, as obtained from experiment [4]. $\Phi_{H,rel}$ denotes the relative H-flux, varied in the range between 0.0 and 0.45. 143

8.1 Selected growth species and their relative fluxes towards the substrate. $\Phi_{H,rel}$ is the relative H-flux towards the substrate, in the range between 0 and 0.45. 153

Acknowledgments

In the past four year preparing this thesis, many people have crossed my path, contributing at some moment in time in one way or another to this work. It is a virtually impossible task to acknowledge all these people, for this list is quasi infinite. Nevertheless, I do feel like some people have been really essential, and this is the place where I would like to express my gratitude to all of them.

First of all, I would like to thank my promotor, prof. Annemie Bogaerts. If for nothing else, she was the one who truly guided me on this journey. Annemie, thank you for all your ideas, your infectuous enthusiasm, and your incessant support. Thank you for your belief in me.

My thanks also go to prof. Renaat Gijbels. His words of wisdom have always been inspiring, enabling one to see things from a different perspective – an invaluable quality in science!

I would also like to thank prof. Richard van de Sanden, from the ETP group in the Technical University of Eindhoven, and dr. Ir. Jan Benedikt, who worked in the ETP group during my thesis. Many of the ideas presented in this thesis find their origin in the work performed in the ETP group. Richard, Jan, I am very grateful to you for your ideas, your support and our many discussions and visits.

The simulations presented in this work have been performed using a code originally written by prof. Cameron Abrams. It is quite obvious that this is a truly major contribution to this work. Cameron, thank you very much for sharing your original code and our many email conversations.

Further, I would also like to thank prof. Dirk Lamoen and dr. John Titantah from the Physics Department, and prof. Barend Thijsse, from the Technical University of Delft, for our interesting and helpful discussions.

Three persons deserve a special word of thanks. Koen De Cauwsemaeker and Luc Van't dack, the former and present computer technicians at our own PLASMANT group, respectively, and Tom Docx, the sysadmin from the CALCUA supercomputer. They are the ones that keep the computer facilities running – an absolutely necessary ingredient for any thesis on computer simulations! Koen, Luc and Tom, thank you very much.

I would also like to thank all of our former and present group members, for they are the people you daily meet with, discuss with, and work with: Myriam (thanks for the coffee!), Neyda, Kathleen, Violeta, Liu, with whom I really enjoyed working together, Dieter, Upendra, Andriy, Ivan, Chen, David, Tom, Davide, and Evi. Many thanks to all of you! A special word is reserved for Min Yan. Min Yan, you have introduced me to computer simulations during my M.Sc. thesis, and you have taught me so many things. Thank you very much. Two more people from our group have also taught me a lot: Maarten and Maxie, "my" thesis students. Maarten and Maxie, I am grateful that I had the opportunity to help you – as such, you have taught me more than you probably think.

I am also very grateful to the people from the secretariat. Nelly, Tania and Ingrid, thank you for helping me getting past the hurdles of bureaucracy.

I would also like to acknowledge the financial support granted by the *Institute for the promotion of innovation through science and technology in Flanders (IWT-Vlaanderen).*

Besides the people who helped me on the scientific and the university level, I would also like to thank a couple of people from my non-scientific life. First of all my parents – thank you so very much for all of your everlasting support, and for being there for me whenever I need you.

My family, especially Kris, Annemie, Nicole, and Arlette, for always being there for me. Special friends, that I was lucky enough to meet: Gino, Davy, Jan, Sofie and Aline, for the many hours that we spent together. All of you are important to me, and contributed as such to this work. Thank you.

Finally, I would also sincerely like to thank Daniël and Lin, from La Luna: teaching tango, you have added a new dimension to my life – it feels like I have found what I was looking for. Last, but not least, I would like to thank my regular dance partners, for the many hours of heart-warming tango-ing: Hannah, my first and dearest dance partner, Judith, Viona and Nele.

Chapter 1

Amorphous (hydrogenated) Carbon

1.1 Structure and terminology

Carbon forms a great variety of materials, ranging from crystalline to amorphous structures. This plethora of materials exists due to the different hybridisations carbon can exist in [2].

In the *sp^3 hybridisation*, as in diamond, each of the four valence electrons of a carbon atom is assigned to a tetrahedrally directed sp^3 orbital, forming a strong covalent σ bond to each of its four neighbouring atoms. In the *sp^2 hybridisation*, as in graphite, each carbon atom is three-coordinated. Three of the four valence electrons enter trigonally directed sp^2 orbitals, which form three σ bonds in a plane. The fourth valence electron lies in a p orbital, normal to the plane formed by the σ bonds. This p orbital forms a π bond with a p orbital from one of its neighbouring atoms. In the *sp hybridisation*, two of the four valence electrons enter σ bonds, while the remaining two electrons enter p orbitals in the orthogonal directions, forming two π bonds. A schematic representation of the different C-hybridisations is shown in Fig. 1.1. Ultimately, the properties of any carbon material are determined by the structure of the material, which is in turn determined by the carbon hybridisation, and of course by other elements present in the material.

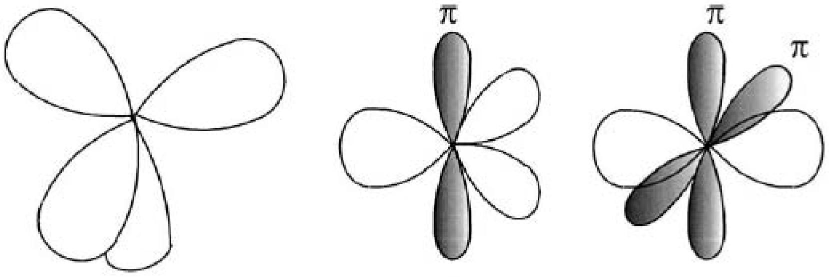

Figure 1.1: The sp^3, sp^2 and sp carbon hybridisations.

Important carbon materials include crystalline diamond and graphite, carbon nanotubes, fullerenes, polymers, and a broad class of amorphous materials. The amorphous materials can be devided into those that consist of carbon only, and those that consist of carbon and one or several other elements, such as hydrogen, nitrogen, or metals. Even limiting ourselves here to those materials containing only carbon and hydrogen, many different classes of materials exist, each with their own specific properties.

Following Casiraghi [5], hydrogenated amorphous carbons (a-C:H) can be classified into four groups:

1. a-C:H films with the highest H content (40-50%). These films can have sp^3 fractions up to 60%. However, most of the sp^3 bonds are H-terminated. Hence, there is no strongly interconnected C_{sp^3} - C_{sp^3} network, and these films are soft and porous. Their hardness is usually below 10 GPa [6]. They are referred to as polymeric a-C:H (PLCH).

2. a-C:H films with intermediate H content (20-40%). Although these films have generally a lower sp^3 content, the C-C sp^3 network is more extensive as compared to PLCH films. Hence, these films are denser and harder. Hardness values of up to 20 GPa can be obtained [6]. They are often referred to as diamondlike a-C:H (DLCH).

3. ta-C:H, or hydrogenated tetrahedral amorphous carbon. They contain up to 70% sp^3 bonds, and a H fraction of 25%. These films have the highest density and hardness of all a-C:H's, with a hardness of up to 50 GPa [7].
4. a-C:H with low H content ($< 20\%$). They have a high sp^2 content, and are referred to as graphitic a-C:H, or GLCH. Their hardness is usually only a few GPa [8].

Obviously, these categories are not defined by sharp boundaries. Furthermore, the overall structure is not necessarily homogeneous. For example, ta-C:H can locally contain crystalline fractions, embedded in a more amorphous matrix. DLCH can contain clusters of sp^2 carbons, embedded in a sp^3 matrix.

A convenient representation of the different amorphous carbons can be displayed on a ternary phase diagram as shown in Fig. 1.2 [1]. Materials with a disordered graphitic structure, such as soot or glassy carbon lie in the lower left hand corner. Hydrocarbon polymers, such as polyethylene and polyacetylene, define the limits of the diagram in which films can exist. Beyond these limits, in the lower right hand corner of the diagram, interconnected C-C networks cannot form, and only molecules can be formed. The softer types of a-C's and a-C:H's are found in the bottom half of the triangle, while the harder ta-C and ta-C:H are found in the top half of the diagram.

1.2 Current understanding of the deposition mechanism

Since their first preparation by Aisenberg and Chabot [9] in the early '70s, DLCs have received a lot of attention. Much is already known regarding their deposition mechanisms. For hard films, the key property is the sp^3 fraction. The sp^3

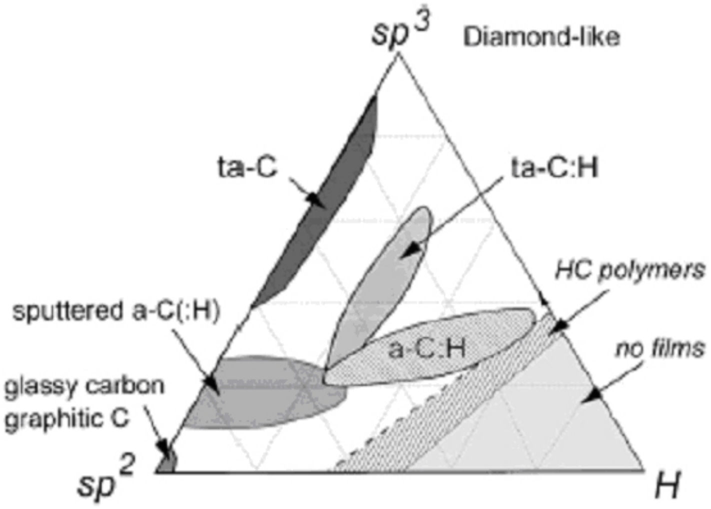

Figure 1.2: Ternary phase diagram of amorphous carbon-hydrogen structures [1].

matrix of hard DLCs forms a rigid, strongly cross-linked network, determining the mechanical properties of the film. The deposition process which promotes sp^3 bonding is a physical process: ion bombardment [10–14]. The highest sp^3 fractions are obtained using C$^+$ ions with an ion energy around 100 eV [2].

The deposition mechanism of these hard ta-C(:H) layers is currently understood in terms of the so-called “subplantation model”. Robertson proposed that the subplantation created a metastable increase in density, leading to a local change in bonding to sp^3 [15, 16]. Various simulations demonstrated the basic idea of subplantation, see *e.g.* [17–20]. Carbon ions in the energy range of 10-1000 eV, can penetrate up to a few nm into the growing film, loosing their energy mainly by elastic collisions with the target atoms (nuclear stopping). Hence, the carbon ions penetrate the surface, and enter a subsurface interstitial site. This increases the local density. The local bonding will then reform around that atom according to this new density. The whole process consists of three stages: (a) a collisional stage ($\sim$ 0.1 ps); (b) a thermalisation stage ($\sim$ 1 ps); (c) a relaxation stage ($\sim$ ns range). The thermalisation and relaxation stages are presumed to allow the excess density to relax again, causing a loss of sp^3 bonding at higher ion energies. At low ion energies, the increased sp^3 content is explained by the increasing penetration probability. At high ion energies, the decreased sp^3 content is controlled by the relaxation.

Although this model can explain the energy dependence of the sp^3 fraction, the relaxation stage of this process is not yet fully understood. Furthermore, the model cannot explain the transition temperature to sp^2 bonding (at around 400-500 K), nor its dependence on the ion energy.

In the softer a-C(:H) films, the deposition mechanisms are different. In Fig. 1.3, a schematic drawing is shown indicating various processes occurring at an a-C:H surface.

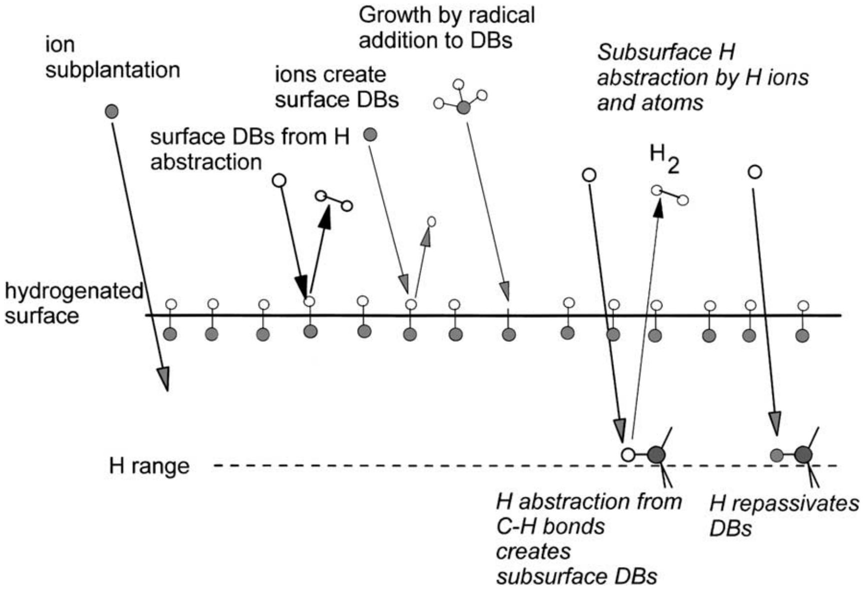
ion subplantation
Growth by radical addition to DBs
ions create surface DBs
surface DBs from H abstraction
Subsurface H abstraction by H ions and atoms
H_2
hydrogenated surface
H range
H abstraction from C-H bonds creates subsurface DBs
H repassivates DBs

Figure 1.3: Schematic representation of the deposition processes in a-C:H film growth [2]. DB stands for dangling bond. The open circles represent H atoms, and the filled circles represent C atoms.

In contrast to ta-C deposition, the ion flux fraction is now much less than 100%, and may be as low as only a few percents [6, 21]. The role of the ions remains the same as for the deposition of hard layers, i.e., if they have enough energy, they will penetrate the surface in order to become subplanted and they will locally increase the density, leading to an increase in the local sp^3 fraction. However, in systems involving not only ions but also neutrals, such as in *e.g.* PECVD deposition (see below), the neutral species also contribute to the growth. In contrast to subplantation, which is a physical process, this is a chemical process. Indeed, the contribution of each neutral species to the growth rate depends on its sticking coefficient, which is in turn determined by its chemical surface reactivity [2].

The a-C:H surface is essentially fully covered by C-H bonds, so it is chemically passive. Diradicals, such as CH_2, can insert directly into C-C and C-H surface bonds. Hence, these species have sticking coefficients approaching 1. Closed shell neutrals, on the other hand, such as CH_4, have very low sticking coefficients and their effect is negligible. Monoradicals, such as CH_3, have a moderate effect. They can react with the film surface if dangling bonds are present, since they cannot insert directly into surface bonds. These dangling bonds can be created by removal of H-atoms at the surface. Hydrogen atoms can be removed either by an ion displacing the H-atom, or by an H-atom abstracting H from the C-H surface bond, or by an incoming radical such as CH_3. The latter mechanism is shown to be responsible for the synergistic effect of H on the sticking coefficient of CH_3 [22, 23]. Neutral hydrocarbon radicals can only react at the surface, since they are too large to penetrate into the layer. Hydrogen atoms, on the other hand, can penetrate about 2 nm into the film [24]. There, they can create subsurface dangling bonds, abstracting H from subsurface C-H bonds, with the formation of H_2, which can desorb from the film, or become trapped interstitially. In sources where no substrate bias is used, and ion bombardment of the substrate is negligible (*e.g.* in the so-called "expanding thermal plasma", or ETP, see below, section 1.4.5), growth proceeds entirely through chemical surface reactions.

1.3 Properties and applications

The properties of a given material ultimately depend on the structure of the material. Since amorphous carbons can exist in many different structures, the properties of these materials also vary accordingly. Obviously, the properties of the material also determine the possible applications.

The *mechanical properties* of DLCs are of great importance because of their extensive use as protective coatings. Mechanical properties include *e.g.* hardness, density, adhesion, wear, and friction. The *hardness* of DLCs ranges from very soft (a few GPa) to very hard (up to values of 88 GPa) [2]. The hardness is mainly determined by the sp^3 fraction and the H fraction. While polymeric a-C:H can contain a large sp^3 fraction, the C-C sp^3 fraction is rather low due to the incorporated H-atoms. Hence, these films will be soft and porous. ta-C:H on the other hand also contains a large sp^3 fraction, but significantly less H, increasing the extent of the C-C sp^3 network, and hence increasing the hardness. For comparison, diamond is the hardest material known (100 GPa), while graphite is among the softest materials known.

Closely related to the hardness of a-C(:H) and ta-C(:H) is its *density*. The density varies between 1.2 $g.cm^{-3}$ for soft a-C:H films up to 3.3 $g.cm^{-3}$ for superhard ta-C [12]. Again, the main factors are the sp^3 fraction and the H content in the film. For comparison, the density of diamond is 3.52 $g.cm^{-3}$, and the density of graphite is 2.25 $g.cm^{-3}$.

Since the main application of (hard) films is their use as protective coatings, a good *adhesion* to the substrate is crucial, requiring low compressive stresses. However, the compressive stress in the film is proportional to the hardness of the film. The compressive stress limits the maximum thickness of the film, since thick films with high compressive stress will easily delaminate. Several solutions can be thought of to circumvent this problem. One solution is to first deposit one or several adhesion layers on the substrate, onto which the protective coating can then be deposited [25–28]. Another solution is to cause ion beam mixing between film and substrate in order to ensure a mixed interface. This can be accomplished by using a high ion energy in the first stage of the deposition process [28].

Amorphous carbon films are also notable for their low *friction coefficients*. For a-C:H, values as low as 0.01 [29, 30] and 0.002 [31] have been reported. However, usually values between 0.02 and 0.15 are found for a-C:H. For comparison, the friction for steel on steel is about 0.8. It is believed that these low friction coefficiens are due to the hydrophobic nature of the a-C:H surface: contact with a different surface causes the formation of a transfer layer of a-C:H to be formed on the other surface. Thus, the contact is essentially between two hydrophobic a-C:H layers, which only interact with each other through van der Waals forces. Hence, the friction force is rather adhesive/deformative than abrasive in nature. The surface of ta-C on the other hand is believed to transform into graphitic layers upon contact and wear. These graphitic layers then behave as a solid lubricant. These mechanisms also account for the resistance of these films to wear.

DLC films also show excellent *chemical resistance*. At room temperature, DLC films are chemically inert to practically any solvent, acid or base, even to strong acidic mixtures, such as the so-called “acid etch” (HNO_3:HF = 7:2). Because of this chemical resistance and their continuity, DLC films can be used as corrosion-resistant coatings [32].

These mechanical, tribological and chemical properties enable amorphous carbons to be used in a variety of applications. As mentioned above, one of the main applications is their use as *protective coatings*, *e.g.* on magnetic hard disks. DLC is used because it can be made very thin, and it exhibits an extreme smoothness, it is continuous and chemically inert. Presently, there are no competitors as a coating material for this application. They are also used as protective coatings on *e.g.* razor blades [33], sunglasses [34] and bar-code scanners. This is possible due to the optical transparancy of DLCs in the IR region (apart from the absorbing C-H bands).

Furthermore, DLC can also be used as a *biocompatible coating*, on parts such as hip joints, hart valves and stents, due to the fact that the carbon material is biocompatible, has a low friction coefficient, and does not produce metallic wear debris [35–37].

Besides the applications of amorphous carbons based on their mechanical, tribological and chemical properties, they are also used in *electronic applications*, although to a much lesser extent. One example is their use as antifuses. An antifuse changes from high to low electrical resistance when they pass a large current. This process in a-C's is believed to involve a change to more sp^2 bonding as the large current passes. Amorphous carbons have been shown to make useful antifuses [38, 39].

1.4 Deposition techniques

Many different deposition techniques have been devised to deposit thin amorphous carbon films. Depending on the technique used, different types of films can be deposited. The most popular techniques include ion beam deposition, mass selected ion beam deposition, sputtering, and plasma enhanced chemical vapor deposition (PECVD).

1.4.1 Ion beam deposition

In 1971, Aisenberg and Chabot [9] were the first to deposit DLCs using ion beam deposition (IB). In fact, ion beam deposition is a term used to group several similar deposition techniques. The common feature of these techniques is to use a beam of carbon or hydrocarbon ions with medium energy (tens to hunderds of eV).

Essentially any technique using medium energy ions to grow the film, whatever their origin, could be categorized as ion beam deposition.

Typically however, the ions are produced by plasma sputtering of a graphitic cathode in an ion source [9, 40]. Alternatively, a hydrocarbon gas can be ionised in a plasma [41, 42]. The ion beam can then be extracted from the plasma source through a grid by a bias voltage. The ions are then accelerated in a high vacuum deposition chamber to form the actual ion beam. Since the ion source runs at finite pressure, the beam also contains a fraction of neutral species. This reduces the flux ratio of ions to neutrals to values as low as a few percents. A more controlled version of the ion beam deposition technique is the mass selected ion beam deposition. Typically, ion beam deposition systems produce films that are hard, dense and have a low surface roughness. Hence, films produced by these sources are well suited for use as protective coatings.

1.4.2 Mass selected ion beam deposition

Mass selected ion beam deposition (MSIB) allows the deposition process to be much more controlled [12, 43]. Again, carbon ions are created in an ion source. These ions are subsequently accelerated to 5-40 keV, and passed through a magnetic filter. Hence, neutrals are filtered out, and ions with an e/m ratio of the C^+ ion are selected. Using an electrostatic lens, the ions are decelerated to the desired ion energy. The film is produced by focusing the resulting ion beam onto the substrate in a vacuum.

The MSIB techniques has several advantages over IB. It allows to select the ion species as well as their energies, thereby controlling the deposition to a much larger extent than the IB method does, and hence allowing the deposition of the hardest and most dense films. Also, neutral species are filtered out, and the film can be doped by switching to other ion species. The main disadvantages, especially in an industrial enviroment, is the very low deposition rate in the order of 0.001 Å.s^{-1} and the high cost of the apparatus.

1.4.3 Sputter deposition

The most common industrial deposition technique for amorphous carbons is sputter deposition [44–46]. The central idea is to sputter material from a graphite electrode, which can deposit on the substrate. The sputtering is accomplished by an Ar plasma, or, as in ion beam sputtering, by an Ar ion beam. A second Ar ion beam can be used to bombard the growing film. This is called ion beam assisted deposition (IBAD) [47]. Alternatively, a magnetic field can be applied to increase the sputtering from the target (magnetron sputtering). Ion bombardment of the substrate can be further enhanced by configuring the magnetic field across the substrate, such that the Ar ions will also bombard the substrate. This is called an "unbalanced magnetron" [48].

Sputter sources generally have a rather low ion to neutral flux ratio towards the substrate, such that very hard films cannot be produced in these sources. On the other hand, these sources are very versatile and are easy to scale up. Also, the deposition conditions can be controlled by the plasma power and the pressure, and they are reasonably independent of the substrate geometry.

1.4.4 Plasma enhanced chemical vapor deposition

One of the most popular (laboratory) deposition techniques nowadays is radio frequency plasma enhanced chemical vapor deposition (rf PECVD) [49,50]. While in IB and MSIB the substrate is placed in a deposition chamber separated from the ion source, in PECVD the substrate is mounted on one of the electrodes in the same reactor where the species are created. The reactor essentially consists of two electrodes of different area. The substrate is placed on the smaller electrode, to which the power is capacitively coupled. The rf power creates a plasma between the electrodes. Due to the higher mobility of the electrons than the ions, a sheath is created next to the electrodes containing an excess of ions. Hence, the sheath has a positive space charge, and the plasma creates a positive voltage with respect to the electrodes. The electrodes therefore each acquire a dc self-bias equal to their peak rf voltage. The ratio of the dc self-bias voltages is inversely proportional to the ratio of the squared electrode areas:

$$\frac{V_1}{V_2} = \left(\frac{A_2}{A_1}\right)^2 \tag{1.1}$$

Hence, the smaller electrode acquires a larger bias voltage and becomes negative with respect to the larger electrode. The negative sheath voltage accelerates the positive ions towards the substrate which is mounted on this smaller electrode, allowing the substrate to become bombarded by energetic ions promoting the sp^3 bonding.

In order to maximize the ion to neutral ratio of the plasma, the plasma must be operated at the lowest possible pressure. Nevertheless, the ions are only about 10 percent of the film-forming flux even at pressures as low as 50 mTorr. Lower pressures cannot be used as the plasma will not longer strike. A second disadvantage of this source is the energy spread in the ion energy distribution, prohibiting a controlled deposition. This energy spread is due to inelastic collisions as the ions are accelerated towards the substrate. The effect of this energy spread is to lower the mean ion energy to about 0.4 of the sheath voltage. Yet another disadvantage of the rf PECVD source is that it is not possible to have independent control over the ion energy and the ion current, as they both vary with the rf power. On the other hand, PECVD allows the deposition of uniform films over large areas, and PECVD systems can be easily scaled up. Films deposited by this source are generally medium hard, up to values of 30 GPa [51].

In order to overcome the disadvantages of rf PECVD, several similar techniques have been developed. Examples include microwave induced PECVD, allowing for a lower gas pressure and a higher ion-to-neutral ratio [52], and electron cyclotron resonance microwave plasma CVD (ECR-MPCVD). The latter technique also allows for a higher plasma density, and control over the ion energy separately from the ion current [53–56].

1.4.5 The expanding thermal plasma

The expanding thermal plasma, or ETP, is a remote PECVD source. Essentially, it consists of two parts: a cascaded arc in which the plasma is created, and a reaction chamber, in which the substrate is placed [57]. A schematic drawing of the set-up is shown in Fig. 1.4. An Ar thermal plasma is created in the cascaded arc plasma source, operated at sub-atmospheric pressure, typically 0.4 bar. The argon plasma expands into the low pressure reaction vessel (typically at 0.3 mbar). At the top of the reaction vessel an injection ring is placed. The hydrocarbon gas is admixed into the emanating plasma by means of this injection ring. In the expanding plasma, many chemical reactions take place, and the growth species are created. These species subsequently reach the substrate where they are deposited.

In [4, 58–65], the ETP source was used with acetylene as the hydrocarbon gas. Since no substrate bias was applied, ion bombardment of the substate is precluded. Nevertheless, medium hard films could be obtained with a hardness of 14 GPa, Young's modulus of 120 GPa, a refractive index of 2.2 and a density of 1.7 g.cm^{-3}. Furthermore, the films showed good adhesion on glass and crystalline silicon, as well as chemical stability. The main advantage of this technique, however, is the ultra-high deposition rate of 70 nm.s^{-1}. It has also been shown that the film quality is improved under high deposition rate conditions [59, 62]. Several studies have been carried out to elucidate the plasma chemistry and the growth species

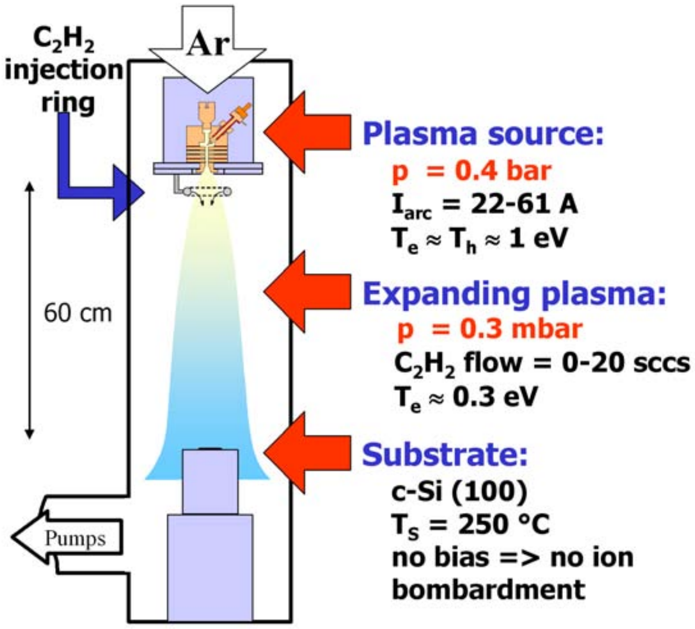

C2H2 injection ring
Ar
Plasma source:
p = 0.4 bar
Iarc = 22-61 A
Te ≈ Th ≈ 1 eV
60 cm
Expanding plasma:
p = 0.3 mbar
C2H2 flow = 0-20 sccs
Te ≈ 0.3 eV
Substrate:
c-Si (100)
Ts = 250 °C
no bias => no ion bombardment
Pumps

Figure 1.4: Schematic drawing of the Expanding Thermal Plasma set-up.

generation [62–65]. It was determined that the crucial factors determining the film properties, as well as the growth rate, were the arc current and the acetylene loading.

The type of growth species that are created in the expanding plasma, is determined by the ratio between the fluxes of the acetylene and the Ar^+ ions:

$$F = \frac{\Phi_{C_2H_2}}{\Phi_{Ar^+}} \tag{1.2}$$

When the C_2H_2 flow is smaller than the argon ion and electron fluence emanating from the plasma source, i.e., $F < 1$, the C_2H_2 is fully decomposed by the plasma reactions, leading to the formation of C, CH, CH_2, C_2 and C_2H. C and C_2 radicals have the highest densities, and are presumed to be responsible for the growth of soft polymer-like a-C:H films formed under these conditions [63]. When the C_2H_2 flow is higher than the argon ion and electron fluence emanating from the plasma source, i.e., $F > 1$, the C_2H_2 is only partially decomposed into C, CH, CH_2, C_2 and C_2H. Under these conditions, the C_2 and C_2H radicals can react with the remaining C_2H_2 leading to the formation of C_4, C_4H and C_4H_2. The C and CH radicals on the other hand react with the C_2H_2, leading to the formation of mainly C_3 and C_3H. These species are unreactive in the gas phase. It was shown that the C_3 radical has the highest density in the region close to the substrate, and its density was correlated with the measured growth rate. Since its surface reactivity was previously already reported to be high [66], it was concluded that the C_3 radical is probably responsible for the fast growth of hard a-C:H films under ETP $F > 1$ conditions. However, it was also found that the stoichiometry of the film could not be explained by the carbon containing growth species alone. Hence, it was concluded that additional H has to be incorporated into the film during the growth.

Although most of the plasma chemistry was indeed elucidated, and the important (presumed) growth species have been identified, the actual growth process remains unclear. More specifically, questions remain regarding the actual growth mechanism, the surface reactions, and the role of the additional hydrogen during film growth.

Aim of this work

It is the aim of the present Ph.D. work to elucidate the above mentioned growth mechanisms and film growth by means of computer simulations.

1.5 Simulation techniques

Thin film deposition encompasses a variety of physical processes, which occur over a wide range of length and time scales. A major challenge in modeling and simulating thin film deposition is this disparity in scales. Therefore, several computational techniques are used to simulate the growth and structure of amorphous carbons. Clearly, the choice of which method to use depends on the desired outcome. There are three major simulation techniques suitable for the simulation of amorphous carbons: (a) quantum-based simulations, including *ab-initio* density functional theory (DFT) and tight-binding (TB) methodologies; (b) molecular dynamics (MD) simulations; and (c) Monte Carlo (MC) simulations. A comparison among the different simulation techniques in terms of time scale and length scale is shown in Fig. 1.5.

1.5.1 Quantum-based simulations

The most accurate simulations are the ab-initio methods. These calculations are based on quantum-mechanical ideas and theoretical considerations instead of empirical fits as in classical MD. Probably the most famous general ab-initio package is the *Car-Parrinello Molecular Dynamics* (CPMD) package based on density functional theory (DFT). The advantage of ab-initio calculations is their accuracy, and the possibility to calculate electronic quantities, such as *e.g.* density of states. Their main disadvantage is the computational cost. The most efficient DFT codes can currently handle up to maybe 500 atoms. Computationally more efficient, but physically less accurate, are the so-called tight-binding (TB) simulations. Most TB simulations are of a semi-empirical nature, i.e., although based on quantum mechanical ideas, empirically fitted parameters are also used in TB potentials. Tight-binding simulations also allow the calculation of electronic properties as well as structural properties. Dynamics (*e.g.* growth) is possible, while the maximum number of atoms is in the order of about 10^3. DFT and TB have been used to study the structure and chemical bonding in amorphous carbons [67–73], as well as to study the actual growth of amorphous carbon [74–78]. These growth simulations focus mainly on the individual particle impacts, and the short-range order of the films. These simulations are, however, limited to the deposition of about 100 atoms. More often, amorphous carbon structures are generated starting from a melt, which is annealed and subsequently quenched, see *e.g.* [67, 70].

1.5.2 Molecular dynamics simulations

In a molecular dynamics simulation, atoms are treated classically, using empirical potential energy functions to determine the forces between the atoms (cfr. Chapter 2. Molecular dynamics simulations are less accurate compared to ab-initio simulations, but allow the simulation of thousands to even millions of atoms. This of course offers the possibility to simulate the actual growth of a-C films, as well as the analysis of their large-scale structure. Belov [79], Jäger [80] and Belov and Jäger [81–86] have investigated the structure, relaxation and properties of ta-C's using MD simulations employing both the Tersoff and Brenner potentials. They also investigated the growth of ta-C films using MD simulations, bombarding the substrate with medium energy C-atoms and C_2H_2 molecules (ca. 100 eV), using the same methodology as applied in our work. Similar growth simulations were performed by Kaukonen *et al.* [17, 18]. These simulations substantiate the validity of the subplantation mechanism for ta-C growth, showing how C-atoms with energies of 40 eV and above become subplanted and coincidingly cause densification of the layer. These simulations show subplantation occurring starting at a C-impact energy of about 40 eV, and increasing with increasing energy. On the other hand, recent simulations by Marks *et al.* [87–89] illustrate that the growth of ta-C films is possible well below the subplantation threshold (i.e., at an energy as low as 6 eV) using the Enviroment-Dependent Interaction Potential (EDIP) [90]. Growth of thin hydrocarbon films from adamantane beams with hyperthermal energies (>1 eV) was studied by Plaisted *et al.* [91]. Hyperthermal atom and cluster beam growth (1-100 eV) of thin a-C(:H) films was further simulated by Zoppi *et al.* [92], Plaisted *et al.* [93] and Halac *et al.* [94]. These simulations, however, are not immediately relevant for this work, since they focus mainly on atom and molecule impacts with energies above 1 eV and the formation of ta-C(:H) films.

Therefore, little work has been carried out in the field of thin a-C:H film deposition simulations using hydrocarbon radicals in the sub-eV energy range.

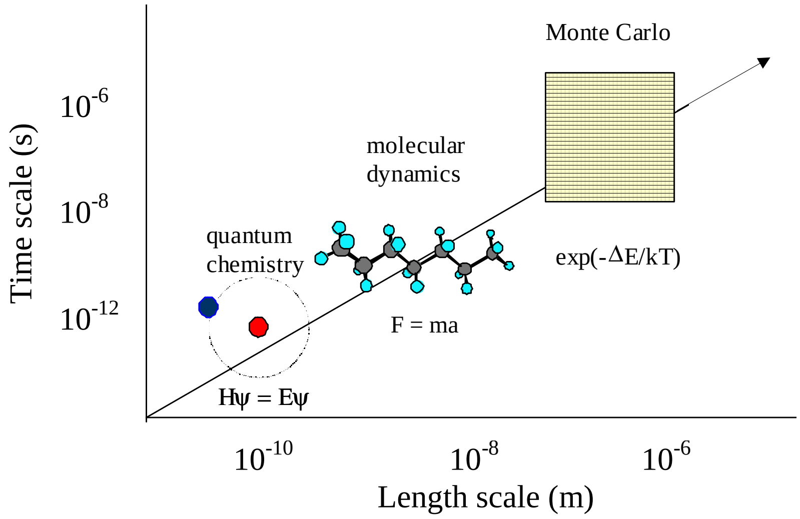

Figure 1.5: Comparison among the different simulation techniques used for thin film growth, in terms of time and length scales.

Molecular dynamics simulations are also used to perform structural analysis of amorphous carbons, *e.g.* Gao *et al.* [95] investigated the effects of the structure of a-C:H films on the mechanical and tribological properties using the Brenner potential; Lee *et al.* [96] studied the structural properties of a-C films as a function of the depositing atom beam energy, using the Tersoff potential. Sinnot *et al.* [97] employed MD simulations using the Brenner potential to study nanometer-scale indentation of amorphous carbons. Using the EDIP potential, Pearce *et al.* [98] investigated the thermal spike behaviour upon impact of medium high energy atoms. The friction behaviour of a-C:H thin films was investigated by Zhang *et al.* [99]. The evolution of sp^2 networks in a-C:H films with substrate temperature was studied by Gago *et al.* [100]. On a more fundamental level, reaction mechanisms have been studied by several authors. Garrison *et al.* [101] demonstrated dimer opening on diamond {001}(2x1) surfaces using the Brenner potential. Detailed reaction mechanisms of CH_3 radicals on diamond {111} surfaces have been investigated by Träskelin *et al.* [102] with both classical MD simulations using the Brenner potential and TB simulations. Finally, Perry and Raff [103, 104] studied the reaction mechanisms of several hydrocarbon radicals (i.e., C_2H_2, C_2H, CH_3, CH_2, C_2H_4, C_2H_3, C_3H and C_n (n=1-3)) on a diamond {111} surface, also using the Brenner potential.

1.5.3 Monte Carlo simulations

An important drawback of MD simulations are the limited time and length scales that are atainable. These limitations can be partially bridged using speed-up algorithms, such as hyperdynamics or temperature accelerated dynamics (TAD) [105–107]. Another important technique to simulate thin films and thin film growth on longer time and length scales, is kinetic Monte Carlo. Atoms are moved according to some probability over a lattice, according to the energy calculated from a specified interatomic potential. Usually, however, a list of all possible transitions (atomic moves) needs to be available in advance. The main advantage is the computational efficiency, allowing millions of atoms to be simulated over long time scales. The actual growth of thin amorphous carbon layers has not often been simulated using MC methods [108]. Film structure and morphology of a-C layers was studied using MC simulations by Patsalas et. al. [109]. MC simulations have also been applied to study thin diamond film growth, see *e.g.* [110–112].

The main application of Monte Carlo simulations in the realm of thin amorphous carbon films is, however, the simulation of diffusion. As mentioned above, the main problem is to construct a list of possible events, see *e.g.* [112–114]. Two notable exceptions are developed by Kaukonen [115], and Mousseau and Barkema [116–118], which do not require the creation of such lists.

Aim of this work

In this work, we have chosen to use molecular dynamics simulations. These simulations are performed to investigate the deposition of thin a-C:H films for ETP-relevant conditions in particular, and from low-energy hydrocarbon radicals in general.

Chapter 2

Molecular dynamics simulation techniques for thin film deposition

2.1 Introduction

In the past, physical sciences were characterized by an interplay between theory and experiment. In an experiment, the scientist subjects the system to a series of measurements, and results in numeric form are obtained. In theory, a model of the system is constructed as a set of mathematical equations. This theoretical model is then validated by comparing the model results with the experimental results. Usually, however, this can be done only in a few selected cases, simple enough to allow a solution for the model to be computed. Often, this implies that many "real world" complexities, invariably associated with real world problems, need to be eliminated in order to make the model solvable [119].

In experiments, on the other hand, one is confronted with the opposite problem: all complexities associated with the problem are necessarily included. It is virtually impossible in an experiment to vary only one parameter, leaving all other parameters constant. This obviously leads to the problem of how to interpret the results obtained. Second, some quantities are simply impossible to measure. For example, there exists no experimental technique to obtain the 3-D configuration of an arbitrary substance on the atomic level. Also, experiments inherently do not allow thought experiments to be realized.

Since the 1950t́s, however, this division between experimental and theoretical science was altered with the advent of high speed computers. In a *computer experiment*, one still uses some theoretical model, but the calculations are carried out by a machine, following a given recipe. Since computers are capable of performing calculations much faster than humans, additional complexity can be introduced compared to *"pen-and-paper"* models. On the theoretical level, one is no longer confined to studying special cases, and situations involving many degrees of freedom can be studied. On the experimental level, computer experiments, *a.k.a.* computer simulations, or simply *simulations*, do allow thought experiments, or the investigation of regions which are not accessible experimentally. Furthermore, simulations can help us to understand and interpret the outcome of experiments. In a way, computer simulations bridge the distance between theory and experiment.

Needless to say, simulations also have their drawbacks: the more complexity is introduced in the model, the slower the simulation will become. For example, it seems quite impossible for the next 10 years, that quantum mechanical calculations can be performed on a system of macroscale size and time scales. Also, a theoretical model on which the simulation is based, is still required – a model which we often do not yet have. For example, in the realm of so-called *molecular dynamics simulations*, some interatomic potential is needed to calculate the interactions between the atoms in the system. For many materials, such interatomic potentials have not yet been developed.

Finally, it should be realized that theory, computer simulations, and experiments are first and foremost *complementary.* Experiments will probably always remain necessary, both for simple validation, but also for the virtually infinite complexity of real life – a complexity which no model will probably ever be able to describe.

2.2 Elements of Molecular Dynamics

2.2.1 Introduction

We call *Molecular Dynamics simulation* (MD) a computer simulation technique where the time evolution of a set of interacting atoms is followed by integrating their equations of motion [119]. As such, MD is a deterministic particle method, as opposed to *e.g.* Monte Carlo simulations. In order to perform MD simulations, we essentially need some interatomic potential function through which the atoms can interact with each other, and some integration scheme. A simulation that is supposed to yield physical results, however, also requires a couple of additional ingredients, such as a method to control the temperature and periodic boundaries. These elements of MD will be explained below.

2.2.2 Classical dynamics

The molecular dynamics simulations as performed in this work are classical MD studies. The computational atoms in these simulations are point masses. Their time evolution is monitored by integrating the Newton equations of motion:

$$\mathbf{F}_i = m_i \mathbf{a}_i \tag{2.1}$$

for each atom i in a system of N atoms. Here, m_i is the mass of atom i, $\mathbf{a}_i = d^2\mathbf{r}_i/dt^2$ its acceleration and $\mathbf{F}_i$ the force acting upon it, due to the interactions with other atoms. Therefore, MD is a deterministic simulation technique, i.e., once an initial set of positions and velocities is assigned to the atoms, their subsequent time evolution is in principle completely determined.

In reality, however, the atoms are of course quantum mechanical particles, such that this classical description is only an approximation. The Heisenberg uncertainty relation forbids knowing an atom's position and momentum simultaneously with arbitrary precision:

$$\Delta p \Delta r \geq h/2\pi \tag{2.2}$$

where Δp and Δr are the uncertainties in momentum and position of the atom, respectively, and h is the Planck constant, $6.626068 \cdot 10^{-34}$ m^2.kg/s. If we can accept an uncertainty of *e.g.* 0.1 Å in the position of a carbon atom, then the uncertainty in this atom's momentum would be about $5.3 \cdot 10^{-24}$ kg.m/s, or 32 amu.Å/ps, corresponding to an uncertainty in energy of about 0.004 eV. This value is much smaller than any bond strength considered in this work, and 0.1 Å is much smaller than any bond length considered. It therefore seems reasonable to describe the motion of the atoms classically in these simulations. Alternatively, other equivalent arguments to justify the use of classical dynamics have been made, based on the de Broglie wavelength of particles (see *e.g.* [119, 120]).

Besides these mathematical justifications, a philosophically different argument has been pointed out by Rapaport [121]: historically, classical MD simulations have yielded results that agree surprisingly well with experiments. The rigor of quantum mechanics notwithstanding, this is perhaps the most compelling reason to deal with atomic motion using classical dynamics.

2.2.3 Statistical mechanics

A molecular dynamics simulation is essentially a statistical mechanics method. The computer calculates the trajectories of N atoms in a $6N$ dimensional phase space ($3N$ positions and $3N$ momenta). Most of the time, however, we are not particulary interested in the exact trajectory of every atom, but rather in the resulting configuration of the atoms. Each time step, the configuration of the system changes, and averaged over these different configurations, a set of configurations distributed according to some statistical distribution function, or statistical ensemble, is obtained. For example, consider the microcanonical ensemble. This ensemble corresponds to a probability density in phase space where the total energy is constant. Measuring a physical quantity by simulation is then obtained as an arithmetic average of the various instantaneous values assumed by that quantity during the MD run in which the total energy was conserved:

$$A_{obs} = \langle A \rangle_t = \langle A(\Gamma(t)) \rangle_t = \lim_{t_{obs} \to \infty} \frac{1}{t_{obs}} \int_0^{t_{obs}} A(\Gamma(t)) \mathrm{d}t \tag{2.3}$$

Here, Γ denotes one point $\{\mathbf{r}_i, \mathbf{p}_i\}$ in phase space. Practically, all simulations run over discrete time steps, so the integral is rewritten:

$$A_{obs} = \langle A \rangle_t = \frac{1}{t_{obs}} \sum_{\tau=1}^{\tau_{obs}} A(\Gamma(\tau)) \tag{2.4}$$

In principle, all possible states of the system should be visited in order to obtain the correct value for the observable A_{obs}. This is called the ergodicity principle. Of course, this implicitly means that the system must be in thermodynamic equilibrium, i.e., the probability density in phase space of the measured quantity is independent of time. If both conditions are fulfilled, the time average as computed in an MD simulation corresponds to the importance sampling as obtained by Monte Carlo simulations. Ergodicity in MD is, however, practically never accomplished, because the system itself might not be ergodic (i.e., no matter how long the simulation would take, not all phase space points would be visited), or certain regions might be very difficult to reach in a finite simulation time, e.g. because they are surrounded by a high potential energy barrier. Since MD runs are always of finite length, one should exert caution to estimate when the sampling may be good ("system at equilibrium") or not.

2.2.4 Interatomic potentials

Within the framework of classical dynamics, the forces acting on the atoms are derived from an interatomic potential that describes the material under consideration. Consider an isolated system, in which both the total energy, the volume and the number of particles in the system are conserved. This corresponds to the microcanonical ensemble in statistical mechanics. The total energy of the system is the sum of the total kinetic energy and the total potential energy. The kinetic energy is a function only of atomic momenta ($K = \frac{1}{2}\sum_i \mathbf{p}_i^2/m_i$), and the potential energy U is a function only of the atomic positions ($U = U(\mathbf{r}_1, \mathbf{r}_2, \mathbf{r}_3, \cdots)$). Then the force acting on atom i can be computed as:

$$\mathbf{F}_i = m_i\ddot{\mathbf{r}}_i = -\nabla_{\mathbf{r}_i}U \tag{2.5}$$

Hence, there are N differential equations describing the motion of the N atoms in the system. Clearly, this system of differential equations is highly coupled, since the interatomic potential U, which is in general a nonlinear function of all atomic coordinates, appears in all of them.

Interatomic potentials as used in classical MD simulations find their origin in quantum mechanics. As pointed out above, the relatively massive atomic nuclei are reasonably well described by classical dynamics. The much ligher electrons, on the other hand, are not. One of the fundamental approximations in quantum mechanics, the Born-Oppenheimer approximation, states that the motion of the nuclei and the electrons are effectively uncoupled. Due to their much smaller mass, the electrons move at much greater speads than the nuclei do. Hence, the electrons form a potential field around the nuclei which adjusts instantaneously over time scales associated with the nuclear motion. In other words: the nuclei “see” an average potential field around them – a potential field that varies according to the nuclear motion. This allows the potential energy surface U of a system of atoms to be described as a function only of the nuclear coordinates: it does not depend on the time derivative of the nuclear coordinates, nor on the coordinates of the individual electrons.

The most general form of an empirical interatomic potential is the following sum:

$$U = U_0 + \sum_i U_1(\mathbf{r}_i) + \sum_{i<j} U_2(\mathbf{r}_i, \mathbf{r}_j) + \sum_{i<j<k} U_3(\mathbf{r}_i, \mathbf{r}_j, \mathbf{r}_k) + \cdots + \sum_N U_N(\mathbf{r}_i, \mathbf{r}_j, \cdot, \mathbf{r}_N) \quad (2.6)$$

where U_n is a function of the positions of n atoms. U_0 defines a reference potential, and U_1 is used to describe the interactions of single atoms with external fields. Usually, the potential is constructed from the relative positions of the atoms with respect to each other, rather than from the absolute positions [119, 122]. Hence, the U_0 term is cancelled. Since external fields are not considered in any of the simulations performed in this work, also the U_1 term cancels. The decomposition of U represents the interatomic potential as a sum of n-body energies, where two-body energies describe bonding to first order, three-body energies describes the bond directionality, four-body energies allow for the description of conjugate bonding, etc. The more terms are included, the more accurate the resulting potential will be, but also the more computationally intensive it becomes. How complex the potential needs to be, depends first and foremost on the material under consideration. For example, it is possible to describe liquid argon fairly accurately using a simple two-body Lennard-Jones potential [123], but a much more complex material such as carbon with its different hybridisations and bond directionality requires a potential far more complex.

Different materials require different potentials. While several standard potentials have been developed for certain materials (*e.g.* the embedded-atom method for close-packed metals [124]), there is at present no general functional form available that correctly describes all types of multi-atom bonding. Therefore, a given potential is always limited to a range of materials it can model. Even within a certain class of materials, the transferability of the potential remains an important issue. For example, the Brenner potential [3] is adequate for simulating CVD growth of diamond, but it is not suited for simulating *e.g.* graphite [125] or carbon nanotubes [126, 127].

2.2.5 Numerical integration

In any MD simulation, the goal is to obtain the positions and velocities of the atoms in the system as a function of time. Hence, we need to integrate the equations of motion. In order to do so, one needs an algorithm which is stable, accurate, time reversible, causes no energy drift, preferentially needs only one force evaluation per time step, allows relatively long time steps, and is preferentially simple. One such scheme fulfilling these conditions is the so-called velocity-Verlet algorithm [128], and it is used throughout this thesis. In the velocity-Verlet scheme, the positions $\mathbf{r}_i$ and velocities $\mathbf{v}_i$ are updated using both the current and new values of the acceleration $\mathbf{a}_i$:

$$\begin{aligned}
\mathbf{r}_i(t+\delta t) &= \mathbf{r}_i(t) + \mathbf{v}_i(t)\delta t + \frac{1}{2}\mathbf{a}_i(t)\delta t^2 && (2.7)\\
\mathbf{v}_i(t+\frac{1}{2}\delta t) &= \mathbf{v}_i(t) + \frac{1}{2}\mathbf{a}_i(t)\delta t && (2.8)\\
\textit{Compute} \quad & \mathbf{F}_i(t+\delta t) && \\
\mathbf{a}_i(t+\delta t) &= \mathbf{F}_i(t+\delta t)/m_i && (2.9)\\
\mathbf{v}_i(t+\delta t) &= \mathbf{v}_i(t+\frac{1}{2}\delta t) + \frac{1}{2}\mathbf{a}_i(t+\delta t)\delta t && (2.10)
\end{aligned}$$

As can be seen in the equations above, the velocity is actually calculated in two steps: first, the new positions are calculated from the old positions, velocities and accelerations. Then, the velocities at *half* time step are calculated from the old velocities and accelerations. The new forces are computed, and accordingly the new accelerations. These are then used to complete the velocity calculation. It has been shown [129] that this "leap-frogging" is numerically more stable than the version in which the velocities are calculated in one step (Verlet algorithm). Furthermore, the numerical instabilities associated with the simple Verlet algorithm are resolved in the velocity-version. The accuracy in the velocities is of order $O(\delta t^4)$ instead of order $O(\delta t^2)$ as in the normal Verlet scheme.

Essential for conservation of energy (and physics, for that matter) is the proper choice of the timestep δt. The longer the time step one can choose, the longer the physical time will be that one can simulate. This depends both on the algorithm used and the simulated system. Usually, a time step in the order of one or a few fs are considered adequate [130]. A specific choice for the time step is considered to be adequate if the resulting energy drift is about 0.01% or less, given that the system is sufficiently large and the temperature is not outrageously high. However, very light elements such as hydrogen require a shorter time step. Throughout this thesis, a time step of 0.2 fs is therefore used. The justification of this choice is presented in section 2.4.

2.2.6 Temperature control

In the microcanonical ensemble, the number of particles, the volume and the energy is conserved. At equilibrium, the instantaneous kinetic and potential energy of the system, however, will fluctuate around an average value. The instantaneous temperature is given by statistical mechanics as:

$$\frac{3}{2}NkT = \sum_{i}^{N} \frac{1}{2} m_i \mathbf{v}_i^2 \tag{2.11}$$

However, we are not so much interested in the instantaneous temperature, but rather in the average value. For a system in equilibrium, the average can be obtained as the average over time.

In the process of film growth, particles are bombarding the growing film. Each of these impact events is highly non-equilibrium in nature, and the temperature will (locally) rise dramatically due to the particle impact, dependent on the energy of the incoming particle. Furthermore, as will be described in the next section, the energy brought into the simulation box is unable to "escape", i.e., due to the so-called *periodic boundaries*, the energy is effectively contained within the simulation box. Therefore, to simulate the heat conduction out of the simulation box, and to bring the structure back to the desired temperature, one is required to control somehow the temperature of the film.

This can be accomplished by changing the atomic velocities according to eq. 2.11. The temperature can then be controlled by modifying the equations of motion to effectively change the temperature, as well as suppressing the fluctuations in the atomic velocities. The most famous scheme using this approach is the Berendsen heat bath [131]. The heat bath is implemented by scaling the atomic velocities at each time step or interval of time steps by a factor λ:

$$\lambda = \left[1 + \frac{\delta t}{\tau_T}\Big(\frac{T_{set}}{T} - 1\Big)\right]^{\frac{1}{2}} \tag{2.12}$$

Here, δt is the time step, τ_T is a parameter determining the strength of the heat bath, T_{set} is the desired temperature and T is the instantaneous temperature. A small value for τ_T corresponds to a strong heat bath compared to one with a large τ_T. Typically, values for τ_T are between 1.0 and 0.001.

Clearly, changing the atomic velocities does not retain conservation of energy. Also, the ensemble is not longer the microcanonical ensemble. In [132, 133], it was reported that fluctuations in thermodynamic properties correspond with neither those from the canonical nor microcanonical ensembles. In [134], it was shown that the value of τ_T is the determining factor: in the limit of a very large τ_T, the microcanonical ensemble is reproduced, while a τ_T value equal to the time step results in the canonical ensemble. Beside these limiting cases, the obtained ensemble corresponding to this heat bath is unknown so far.

2.2.7 Periodic boundaries

Any MD simulation contains only a limited number of atoms. A relatively large fraction of these atoms will be positioned at or near the walls of the simulation box. Therefore, the walls of the container cannot be regarded as rigid boundaries, since the simulation would then be unable to simulate the interior of the material. Therefore, a system must be constructed in which the atoms are effectively contained, but nevertheless free of physical walls. This can be accomplished by periodic boundaries, as shown schematically in Fig. 2.1.

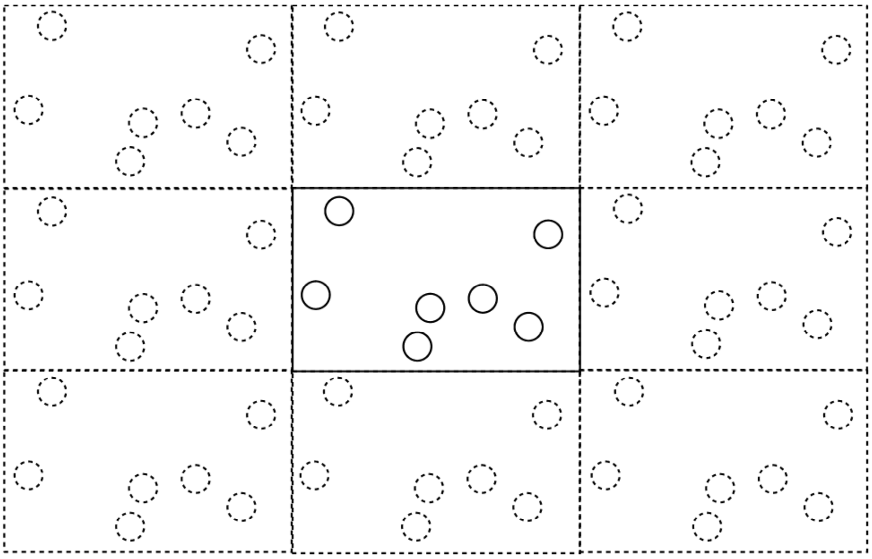

Figure 2.1: Periodic boundary conditions for the two-dimensional case.

The introduction of periodic boundaries is equivalent to the implementation of an infinite array of identical copies of the simulation box in the desired dimensions. Hence, bulk material can be simulated by applying periodic boundaries in all three cartesian directions. A free surface, as in our case, can be simulated by applying periodic boundaries only in the $\pm x$ and $\pm y$ directions. The planes that bound the simulation cell in the desired directions are then the periodic boundaries. As a result, an atom that “moves out” of the simulation box through the $+x$ bounding plane, will reenter the cell through the $-x$ plane with the same velocity and $\{y, z\}$ coordinates, and vice-versa.

The atoms will also interact with each other through the periodic boundaries. That is, an atom near the $+x$ boundary, will interact with an atom within a distance smaller than the cut-off of the interatomic potential near the $-x$ boundary, through the $\pm x$ periodic boundary. The atom then interacts with the *nearest image* of its neighbor. This so-called *nearest image criterion* is depicted schematically in Fig. 2.2.

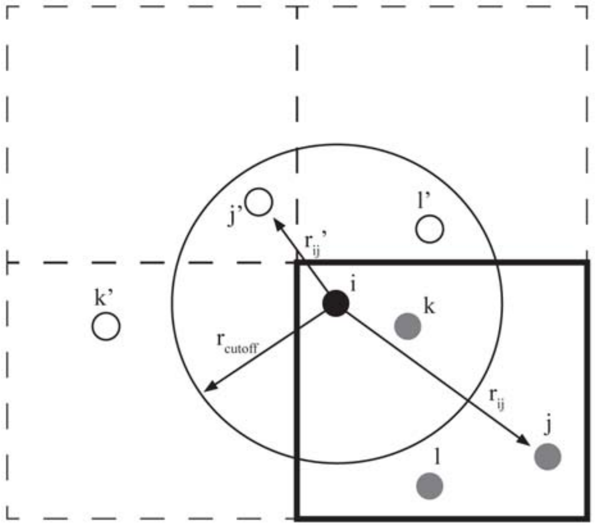

Figure 2.2: The minimum image criterion.

The figure shows the simulation box (in two dimensions), with atoms i, j, k and l. Since periodic boundaries are applied, all atoms have image atoms in the repeated cells. The image atoms are denoted as j', k' and l'. The minimum image criterion states that the distance between any pair of atoms is the shortest possible distance between them. Consider *e.g.* the pair of atoms $\{i, j\}$. From the figure it is clear that the distance r'_{ij} is smaller than r_{ij}. Hence, the distance between these atoms is determined to be equal to r'_{ij} corresponding to the pair of atoms $\{i, j'\}$, and not r_{ij}, corresponding to the pair of atoms $\{i, j\}$.

2.3 The Brenner potential

2.3.1 Functional form of the Brenner potential

In this section, the bond-order potential as introduced by Brenner and used in our MD simulations will be discussed. The potential energy formalism on which the Brenner potential is based, was originally developped by Abell, in an effort to describe a universality relation in binding-energy curves [135]. Abell introduced a general expression in which the binding energy is given as the sum of nearest-neighbour pair interactions that are moderated by the local atomic environment [136]. Based on this formalism, Tersoff introduced an analytical potential-energy expression describing the bonding in silicon for a number of solid-state structures [137, 138]. Subsequently, Tersoff proposed a similar potential for carbon [139]. The Brenner potential [3,140], is essentially a modification of the Tersoff potential for carbon, allowing for a better description of various carbon materials, including hydrocarbons. The Tersoff and Brenner potentials are often referred to as "REBO" potentials: reactive empirical bond-order potential. The original implementation of the potential used in this thesis, was done by Abrams [141].

In the Brenner potential, the binding energy is written as a sum over bond energies:

$$U = \sum_{i} \sum_{j>i} \phi_{ij}, \tag{2.13}$$

where i and j denote the atoms. The bond energy ϕ_{ij} is determined by repulsive and attractive components:

$$\phi_{ij} = V_R(r_{ij}) - \bar{b}_{ij} V_A(r_{ij}) \tag{2.14}$$

The repulsive and attractive components are given as:

$$V_R(r_{ij}) = f_{ij}(r_{ij})A_{ij} \exp\left(-\lambda_{ij} r_{ij}\right) \tag{2.15}$$

and

$$V_A(r_{ij}) = f_{ij}(r_{ij})B_{ij} \exp\left(-\mu_{ij} r_{ij}\right) \tag{2.16}$$

where the scalar separation between i and j is denoted by r_{ij}. A_{ij}, B_{ij}, λ_{ij}, and μ_{ij} are parameters specific to the two elements participating in the bond. The $\bar{b}_{ij}$ function is the so-called "bond order" function, modeling the many-body chemistry as explained below.

The following subscript convention is used: when ij appears on a variable, such as r_{ij}, i and j refer to individual atom indices; when ij appears as a subscript on a function, such as f_{ij}, or a parameter, such as μ_{ij} then i and j refer to the *elements* of atoms i and j. In the original paper, Brenner introduced two parameter sets. Throughout this thesis, parameter set II has been used, since this parameter set describes the force constants more accurately than the parameter set I does [3]. Values for these parameters are given in Table 2.1.

In order to limit the potential range to first neighbors only, a cutoff function is introduced. Therefore, only short range interactions are included in the potential. Instead of using the Brenner cutoff function, the Murty-Atwater cutoff function has been implemented [142]:

$$f_{ij}(r_{ij}) = \begin{cases} 1 & r_{ij} < R_{ij}^{(1)} \\ \frac{1}{2} - \frac{9}{16}\sin\left(\pi \frac{r_{ij} - \left(R_{ij}^{(2)} + R_{ij}^{(1)}\right)/2}{R_{ij}^{(2)} - R_{ij}^{(1)}}\right) - \frac{1}{16}\sin\left(3\pi \frac{r_{ij} - \left(R_{ij}^{(2)} + R_{ij}^{(1)}\right)/2}{R_{ij}^{(2)} - R_{ij}^{(1)}}\right) & R_{ij}^{(1)} \leq r_{ij} \leq R_{ij}^{(2)} \\ 0 & r_{ij} > R_{ij}^{(2)} \end{cases} \tag{2.17}$$

$R_{ij}^{(1)}$ and $R_{ij}^{(2)}$ are termed the inner and outer cutoff radii, respectively. The f_{ij} function decays smoothly from 1 to 0 between the cutoff radii. Values for the cutoff radii $R_{ij}^{(1)}$ and $R_{ij}^{(2)}$ are also given in Table 2.1. This cutoff function is used because it is smoother than the original Brenner cutoff function, resulting in a better energy and momentum conservation at minimal computational expense. In Fig. 2.3, both the original Brenner cutoff function (dashed line) and the Murty-Atwater cutoff function (full line) are shown for the C-C interaction.

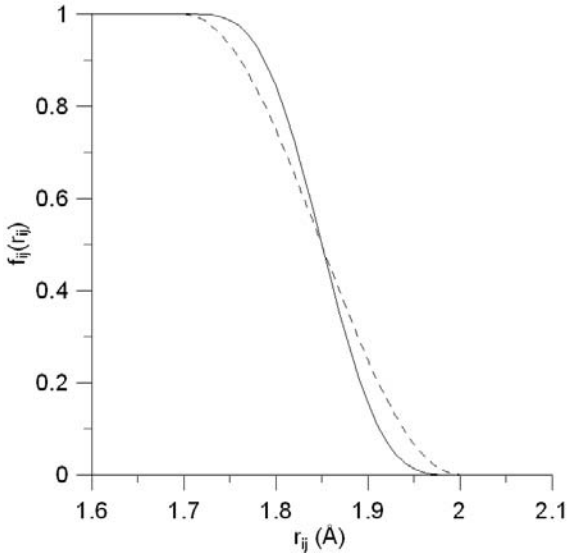

Figure 2.3: Cutoff functions for the C-C interaction of Brenner (dashed line) and Murty-Atwater(full line).

While the Abell-Tersoff expression realistically describes carbon-carbon single, double and triple bond lengths and energies, the assumption of nearest-neighbour interactions combined with the sum over atomic sites results in non-physical behaviour in intermediate bonding situations, i.e., the overbinding of radicals, and the fact that conjugation effects are not included. Both effects are taken into account in the Brenner potential, introducing correction functions as described below. Consider for example a carbon atom with three nearest neighbors bound to a carbon atom with four nearest neighbors. Then without any correction functions added to the $\bar{b}_{ij}$ bond order function, eq. 2.14 would interpolate the bond so that it is intermediate between a single and a double bond. However, the formation of a double bond results from the overlap of unbound $2p$ orbitals. Since the fourfold coordinated carbon atom does not have such a free orbital, π overlap cannot occur, and the bond is better described as a single bond plus a radical orbital. Conjugation effects will be described below.

In the Brenner potential, all the many-body chemistry is modeled through the $\bar{b}_{ij}$ bond order function:

$$\bar{b}_{ij} = \frac{1}{2}\left[b_{ij} + b_{ji} + F_{CC}\left(N_{ij}^{(t)}, N_{ji}^{(t)}, N_{ij}^{(conj)}\right)\right] \tag{2.18}$$

Here, b_{ij} is the contribution of the neighbours of atom i to the bond order of the ij bond. Similarily, b_{ji} is the contribution of the neighbours of atom j to the bond order of the ij bond. b_{ij} is given by:

$$b_{ij} = \left\{1 + \left[\zeta_{ij} + H_{ij}\left(N_{ij}^{(H)}, N_{ij}^{(C)}\right)\right]^{\eta_i}\right\}^{-\delta_i} \tag{2.19}$$

The parameters η_i and δ_i are set to 1 and 0.5, respectively. The F_{CC} function is the Brenner-correction for C-C bonding, handling the intermediate bonding situations described above. The H_{ij} function is also a Brenner-correction that accounts for the different chemistry of H and C. The N symbols will be explained below. ζ_{ij} is given by:

$$\zeta_{ij} = \sum_{k \neq j} f_{ik}(r_{ik}) g_i(\theta_{ijk}) \exp\left\{\alpha_i\left[\left(r_{ij} - R_{ij}^{(e)}\right) - \left(r_{ik} - R_{ik}^{(e)}\right)\right]\right\} \tag{2.20}$$

The parameter $\alpha_{CCC} = 0.0$ and $\alpha_{CCH} = \alpha_{CHH} = \alpha_{HHH} = 4.0$. $R_{ij}^{(e)}$ are the equilibrium dimer bond lengths of elements i and j, and are given in Table 2.1. The angle between the ij and ik bonds, subtended at atom i, is given by θ_{ijk}. The $g_i(\theta)$ function models a potential energy reduction for bond angles deviating from the appropriate equilibrium values, and favors 180^o bond angles and hence open structures. This is physically motivated by valence shell electron pair repulsion theory (VSEPR), which assumes that repulsions between pairs of valence electrons tend to maximize bond angles [143, 144]. This function is given by:

$$g_C(\theta) = a\left(1 + \frac{c^2}{d^2} - \frac{c^2}{d^2 + (1 + \cos\theta)^2}\right) \tag{2.21}$$

In equation 2.21, a, c and d are dimensionless parameters having values of $2.0813{\cdot}10^{-4}$, 330.0 and 3.5, respectively.

To make the potential continuous, the cutoff functions $f_{ij}(r)$ (see eq. 2.17) are used to define the bonding connectivity between the atoms, i.e., to define the total number of hydrogens and carbons ($N_{ij}^{(t)}$) bound to every atom:

$$N_{ij}^{(t)} = \sum_{k \neq j} f_{ik}(r_{ik}) \tag{2.22}$$

The index k runs over the hydrogens only when calculating $N_{ij}^{(H)}$ and over carbons only when calculating $N_{ij}^{(C)}$, to be used in Eq. 2.19. To determine whether carbon atoms i and j in the $\{ij\}$ bond are part of a conjugated system, the quantity $N_{ij}^{(conj)}$ is defined:

$$N_{ij}^{(conj)} = 1 + \sum_{k \neq j} f_{ik}(r_{ik}) F(N_{ki}) + \sum_{l \neq i} f_{jl}(r_{jl}) F(N_{lj}) \tag{2.23}$$

where atoms k and l are carbon atoms. $F(x)$ is defined as:

$$F(x) = \begin{cases} 1 & x \leq 2 \\ \left\{1 + \cos\left[\pi(x-2)\right]\right\}/2 & 2 < x < 3 \\ 0 & x \geq 3 \end{cases} \tag{2.24}$$

The function $F(x)$ in eq. 2.24 should not be confused with the F_{CC} function from eq. 2.18. $F(x)$ is used to determine whether the carbon atoms i and j are part of a conjugated system. As such, it determines the value of N_{ij}^{conj}. This value is then used in the correction function F_{CC}. The function F_{CC} is symmmetric with respect to the first two arguments, i.e.,

$$F(x, y, z) = F(y, x, z) \tag{2.25}$$

Hence, the average bond order $\bar{b}_{ij}$ is symmetric with respect to inversion of atoms i and j. The F_{CC} function is used to determine whether the ij bond is part of a

Table 2.1: Two-body parameters in Brenner's hydrocarbon potential.

Parameter	C-C	C-H	H-H
$A(eV)$	2605.8416	297.5018	80.0703
$B(eV)$	1397.0730	96.8299	31.3793
$\lambda(\text{Å}^{-1})$	3.2803	3.6011	4.2075
$\mu(\text{Å}^{-1})$	2.6888	2.1299	1.7956
$R^{(e)}(\text{Å})$	1.315	1.1199	0.7414
$R^{(1)}(\text{Å})$	1.7	1.3	1.1
$R^{(2)}(\text{Å})$	2.0	1.8	1.7

conjugated system; therefore, this function is only considered if both atoms i and j are carbon atoms - hence the notation F_{CC}. The ij bond is then considered to be part of a conjugated system if any carbon neighbours k and l of atoms i and j, respectively, have a coordination of less than 4. Equation 2.24 yields a continuous value of N^{conj} in Eq. 2.23 as bonds break and form and as second-neighbour coordinations change. For $N_{ij}^{conj} = 1$, a bond is not part of a conjugated system, and the F_{CC} function (and hence the bond-order function $\bar{b}_{ij}$) yields appropriate values. If $N_{ij}^{conj} \geq 2$, the bond is considered to be part of a conjugated system, and function values $F(x, y, z)$ fit to conjugated bonds are used. Values for F_{CC} at integer points are given in Table 2.2. Finally, to ensure that the potential is continuous, a tricubic spline is used for F_{CC}, to interpolate between values at discrete numbers of neighbors.

The second correction function (see above) is $H_{ij}(N_{ij}^{(H)}, N_{ij}^{(C)})$. This function is to be applied only when atom i is a carbon, i.e., only C-C and C-H bonds are

Table 2.2: Values of F_{CC} at integer points. The integer points (x, y, z) denote N_{ij}^t, N_{ji}^t and N_{ij}^{conj} from eq. 2.18, respectively. $F_{CC}(x, y, z) = F_{CC}(y, x, z)$ and $F_{CC}(x, y, z > 2) = F_{CC}(x, y, z = 2)$. All values not given are 0. Derivatives (required for tricubic interpolation) are found by 2^{nd} order finite differences.

x	y	z	$F_{CC}(x, y, z)$
0	1	1	0.0996
0	2	1	0.0427
0	2	2	-0.0269
0	3	1,2	-0.0904
1	1	1	0.1264
1	1	2	-0.0108
1	2	2	-0.0243
1	2	1	0.0120
1	3	1,2	-0.0903
2	2	1	0.0605
2	3	1,2	-0.0363

considered. The values of $N_{ij}^{(H)}$ and $N_{ij}^{(C)}$ are again given by Eq. 2.22, i.e.,:

$$\begin{aligned} N_{ij}^{(H)} &= \sum_{k \neq j,\, k \in H} f_{ik}(r_{ik}) \\ N_{ij}^{(C)} &= \sum_{k \neq j,\, k \in C} f_{ik}(r_{ik}) \end{aligned} \tag{2.26}$$

The H_{CC} and H_{CH} correction functions quantify how all possible combinations of H and C bound to a carbon atom i collectively affect the bond ij. H_{CC} and H_{CH} are precomputed at integer values of their arguments so that the potential correctly predicts known thermodynamical properties of a selected set of hydrocarbon molecules. These values are given in Table 2.3. Again, to ensure that the potential is continuous, bicubic interpolation is used to evaluate H_{CC} and H_{CH} at non-integer neighbor numbers.

Table 2.3: Values of H_{CC} and H_{CH} at integer points. The integer points (x, y) denote N_{ij}^{H} and N_{ji}^{C} from eq. 2.19, respectively. All values not given are 0. Derivatives (required for bicubic interpolation) are found by 2^{nd} order finite differences.

x	y	$H_{CC}(x, y)$	$H_{CH}(x, y)$
0	1	–	-0.2479
0	2	0.0149	-0.3221
0	3	–	-0.4460
1	0	–	-0.0984
1	1	-0.0226	-0.3344
1	2	–	-0.4449
2	0	-0.0061	-0.2878
2	1	0.0160	-0.4438
0	0	0.0173	0.4507

To ensure a sufficiently strong repulsion at short interaction distances, the Morse-type repulsion component of the Brenner potential (eq. 2.15) is spliced to a Molière potential at very short separations. This is implemented following Beardmore and Smith [145]. The Molière potential for two point charges separated by a distance r is given by [146]:

$$V_M = \frac{Z_1 Z_2 e^2}{4\pi\epsilon_0 r} \sum_{i=1}^{3} c_i \exp\left(-\frac{d_i r}{a}\right) \tag{2.27}$$

Here, Z_i is the nuclear charge of atom i, e is the elementary charge, ϵ_0 is the permittivity of free space, and a is the screening length, determining the effective interaction range of the potential. The values of c_i are $\{0.35; 0.55; 0.1\}$. The values of d_i are $\{0.3; 1.2; 6.0\}$ for $i = \{1; 2; 3\}$.

The Molière potential is only used at interatomic spacings r less than some value r_a, while the Brenner repulsive component is used when the interatomic separation

$r > r_b$. The spline is used between these limits. This spline function also assures that both the potential and its first derivative are continuous at the spline limits. The spline used is an exponential:

$$V_R^{spline}(r) = c + \exp(ar + b) \tag{2.28}$$

The total repulsive component of the two body potential is now expressed as:

$$V_R(r) = \begin{cases} V_R^{Molière}(r) + s & r < r_a \\ V_R^{spline}(r) & r_a < r < r_b \\ V_R^{Brenner}(r) & r > r_b \end{cases} \tag{2.29}$$

The values of r_a, r_b, and the spline parameters a, b, c, and s are given in Table 2.4. The Molière potential was also used for the interaction of Ar-C, Ar-H and Ar-Ar, using a cutoff of 5.0 Å.

Table 2.4: Parameters for the repulsive spline function.

Parameter	value
r_a, Å	0.286968
r_b, Å	0.652200
a, Å	-2.862885
b	7.729378
c, eV	44.727802
s, eV	544.237667

Summarized, the Brenner potential is a highly parametrized, extended version of Tersoff's orgininal empirical bond-order potential, requiring over 40 parameters for the C-C, C-H and H-H interactions to be described. It allows for the description of carbon structures, as well as hydrocarbons, and includes terms that correct for overbinding of radicals and conjugation effects.

2.3.2 Disadvantages of the Brenner potential

Although the Brenner interatomic potential allows to simulate carbon-hydrogen materials fairly accurately, the potential also has several disadvantages. These disadvantages are described shortly in the following list.

1. The concept of a classical description of essentially quantum mechanical particles could in itself be regarded as the most important disadvantage of any empirical potential. Although the parameters in the potential have been fitted as to describe realistic materials as accurately as possible, the formalism itself remains empirical.

2. The cutoff of the potential for C-C interactions was set to 2.0 Å. This value was chosen on a rather arbitrary basis by Brenner. The idea was to limit the interaction range of the potential to the first neighbors only. The effect of the cutoff distance taken too short is a considerable underestimation of the sp^3 fraction in a-C's [78, 80, 90, 147]. Several authors have used longer cutoffs [79–81, 83, 84, 148]. This indeed increases the sp^3 content of a given structure for a given density at the expense, however, of a great number of unphysical metastable distances intermediate between the first and second neighbors [90].

3. The Brenner potential in its original form does not include a torsional potential for hindered rotation around C-C bonds. Brenner developed an updated version of the original potential [149] including a term for hindered rotation around C-C double bonds. However, it has been reported that the dihedral terms (torsional potential) are not conservative due to a cutoff when three atoms are almost along a line. This updated potential has also been implemented in the course of this thesis. However, it was found that in about 1% of the particle impacts, the energy could not be conserved to within acceptable limits, notwithstanding the fact that all tests as described by

Brenner [149] could be reproduced. Since energy conservation is essential, this implementation was not used for any of the results presented in this thesis.

4. The Brenner potential also does not include non-bound interactions. Therefore, structures in which these terms are important, cannot be accurately simulated. The most simple solution is of course to increase the cutoff of the potential, although it is well known that this leads to unphysical results [90].

Due to great interest in carbon materials, and in order to find solutions for the disadvantages of the Brenner potential as described above, several other empirical hydrocarbon potentials have been developed. Prior to Brenner, Tersoff introduced an interatomic potential for silicon [137], which was later reparametrized for carbon [139]. These potentials are the basis on which practically all other empirical carbon and hydrocarbon potentials are based. Brenner introduced his potential in 1990 [3], followed by an erratum in 1992 [140].

As mentioned above, several groups have varied the cutoff values of the Tersoff and Brenner potentials to obtain more realistic sp^3 values. Various attempts have also been made to combine non-bound interactions with the Tersoff and Brenner potentials, while retaining the reactive capabilities of these potentials [150–152], although these attempts have not been overly successful. In 2000, Stuart *et al.* introduced the so-called “AIREBO” potential (Adaptive Intermolecular Reactive Empirical Bond-Order potential). It is based on the updated Brenner potential [149] (which was not yet published at that time), taking into account both the rotational barriers for C-C bonds, and intermolecular interactions. At the same time, Marks [90] introduced his so-called “EDIP” potential for carbon (Environment-Dependent Interaction Potential), similar to the Stillinger-Weber potential for silicon [153]. However, this potential was reported to be unable to reproduce distances associated with double and triple C-C bonds [90]. Very recently, a new empirical potential for carbon has been developed by Lee *et al.* based on the modified embedded atom method (MEAM) [154]. The authors state that their potential is as good as the original Tersoff potential for carbon, and furthermore that it can be easily combined with existing metal MEAM potentials. However, it does not include hydrogen at present.

Notwithstanding the disadvantages of the original Brenner potential, it does remain the most popular carbon potential to date. In Fig. 2.4, the number of citations to the most popular carbon potentials is plotted: “Brenner 1990” [3]; “Tersoff 1988” [139]; “Brenner 2002” [149]; “Stuart 2000” [125] and “Marks 2000” [90]. From the figure, it can be clearly seen how much attention the original Brenner potential has received, even compared to its predecessor, the Tersoff potential.

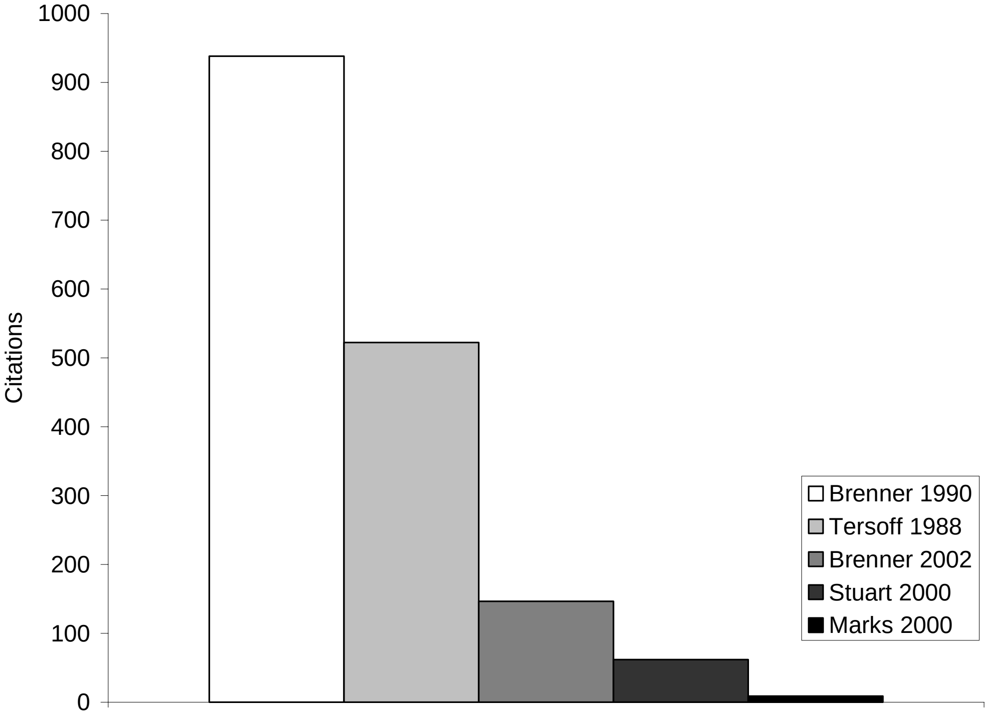

Figure 2.4: Number of citations to the most popular carbon potentials since their publication.

2.4 Validation of the interatomic potential implementation in the model

2.4.1 Atomization energies

The Brenner potential was originally developed as a first step to study chemical vapor deposition of diamond films using molecular dynamics simulations. As a first test of the transferability of the potential to other carbon based materials, Brenner examined the atomization energies of a variety of small hydrocarbon molecules and compared them with experimental values. It was found that the energies calculated with this potential reproduced the experimental values to within 1% or better for 81% of the molecules tested [3].

To test the current implementation of the potential, used in this work, these atomization energies have been recomputed. The atomization energy of a molecule is the total energy needed to reduce a molecule to its individual neutral atoms that constitute the molecule, and can therefore be calculated by minimizing the energy of the molecule. Minimizing the energy of the molecules, and thereby optimizing the geometry of the molecules, was accomplished using the conjugate gradient method [155]. The results are given in Table 2.5.

With the exception of ethynylbenzene, all reported values could be reproduced. Ethynylbenzene minimized to a slightly lower atomization energy, possibly indicating a local minimum in the potential energy surface of which Brenner was not aware. Other authors have also reported the same value as was determined in our work [152, 156].

Table 2.5: Calculated atomization energies for various hydrocarbon molecules (in eV), and the values reported by Brenner [3]. Also given are the experimental values.

Molecule	**Current work**	**Brenner**	**Expt.**
Alkanes			
methane	17.6	17.6	17.6
ethane	29.7	29.7	29.7
propane	42.0	42.0	42.0
n-butane	54.3	54.3	54.3
i-butane	54.3	54.3	54.4
n-pentane	66.5	66.5	66.6
isopentane	66.5	66.5	66.6
neopentane	66.8	66.8	66.7
cyclopropane	35.0	35.0	35.8
cyclobutane	48.5	48.5	48.2
cyclopentane	61.3	61.3	61.4
cyclohexane	73.6	73.6	73.6
Alkenes			
ethylene	23.6	23.6	23.6
propene	36.2	36.2	36.0
1-butene	48.5	48.5	48.5
cyclopropene	27.3	27.3	28.8
cyclobutene	42.0	42.0	42.4
cyclopentene	55.7	55.7	55.6
1,4-pentadiene	55.0	55.0	54.8
Alkynes			
acetylene	17.1	17.1	17.1
propyne	29.4	29.4	29.7
1-butyne	41.7	41.7	42.0
Aromatics			
benzene	57.5	57.5	57.5
toluene	69.6	69.6	70.1
1,4-dimethylbenzene	81.8	81.8	82.6
ethylbenzene	81.9	81.9	82.5
ethenylbenzene	76.2	76.2	76.5
ethynylbenzene	68.4	69.8	69.9
naphthalene	91.4	91.4	91.2
Radicals			
methylene	7.8	7.8	7.8
methyl	12.7	12.7	12.7
ethyl	25.7	25.7	25.5
ethenyl	18.9	18.9	18.9
ethynyl	12.2	12.2	12.2
n-propyl	38.0	38.0	37.8
i-propyl	38.3	38.3	38.0
t-butyl	50.5	50.5	50.5
phenyl	52.7	52.7	52.7

2.4.2 Conservation of energy

The idea behind a molecular dynamics (MD) simulation is to numerically solve the Newton equations of motion of an atomistic or similar system. The atoms then move under the influence of interatomic forces. As long as the force is conservative, this force can be re-obtained by taking the vector gradient of the associated potential field. So, the force $\mathbf{F}$ acting on atom i is given by:

$$\mathbf{F}_i = -\nabla_{\mathbf{r}_i} U \tag{2.30}$$

Once the force is obtained, Newton's second law permits us to calculate the acceleration of atom i: $\mathbf{F}_i = m_i \mathbf{a}_i$. Because acceleration is the first time-derivative of velocity and the second time-derivative of position, we can use a numerical integration scheme to predict the new positions and velocities at an arbitrarily small amount of time in the future. This small amount is the time step, which is the fundamental unit of time in the MD simulation.

The computation of the forces on each atom is usually the most computationally intensive portion of an MD code, and requires careful debugging and analysis to ensure that it performs accurately. A first test to check the accuracy of the potential concerns the conservation of energy. Simulations in which the number of particles, volume and energy remain constant, are termed “NVE” integrations. These generated microscopic states form an ensemble known as the microcanonical ensemble. The conditions of conservation of number of particles and volume are always fulfilled as long as no new particles are introduced or deleted from the simulation domain defining its volume. The energy, however, is computed as:

$$E_{kin} + E_{pot} = Const. \pm \delta \tag{2.31}$$

Thus, for all time steps in a trajectory in which no particles enter or leave the simulation volume, the sum of kinetic and potential energy is constant to within some numerical criterion δ. In Eq. 2.31, δ is desired to be less than about a few thousands of a percent of the total energy ($< 10^{-3}\%$). This is one of the most common ways to test the validity of the subroutine of the model that calculates the forces.

Below, conservation of energy is demonstrated for five systems:

1. A naphtalene molecule;
2. a bulk-terminated 12-monolayer diamond {111} surface, consisting of 768 carbon atoms;
3. a 12-monolayer diamond {111} surface, passivated with 1 monolayer of H, and consisting of in total 832 atoms;
4. an a-C:H layer, consisting of 1910 atoms and containing about 10% of H;
5. a 10 eV CH_3 impact onto an a-C:H surface.

In all figures shown, the total energy, the potential energy and the temperature of the structure are shown. It can be seen that the total energy remains constant in all simulations. The temperature (or, equivalently, the kinetic energy), on the other hand, can fluctuate. These fluctuations in temperature, however, match the fluctuations in potential energy, such that Eq. 2.31 is fulfilled, i.e., the total energy is conserved.

Naphtalene

Fig. 2.5 shows the time evolution of the calculated total energy, potential energy and temperature for an NVE integration of a single naphtalene molecule. The time step was 0.2 fs, and the total integration time was 2 ps, or 10000 time steps. Note the absence of any drift in the total energy. The calculated total energy was conserved to within $9.74301 \times 10^{-5} \pm 7.41046 \times 10^{-5}\%$.

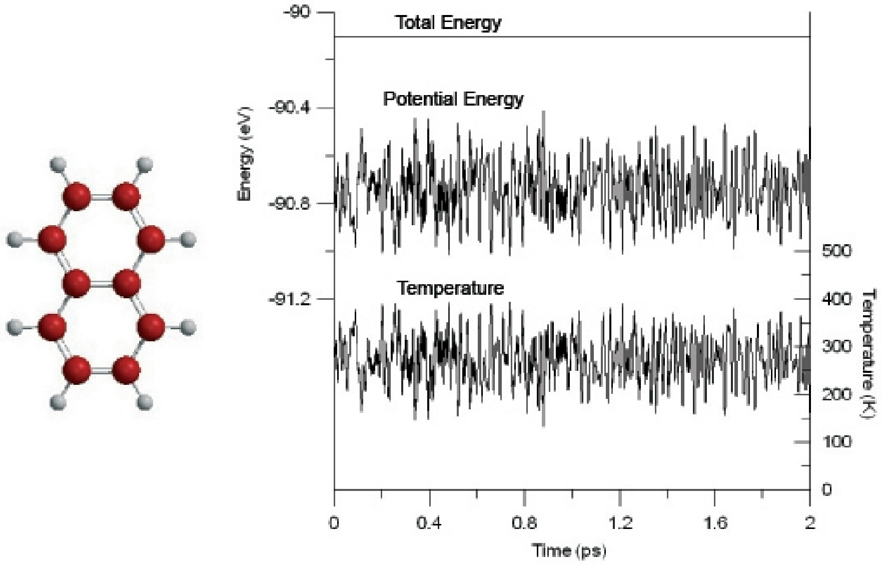

Figure 2.5: Napthalene, and the time evolution of its total energy, potential energy and temperature.

Crystalline diamond

Fig. 2.6 shows the time evolution of the total energy, potential energy and temperature for an NVE integration of a crystalline diamond bulk-terminated {111} surface. The time step was 0.2 fs, and the total integration time was 2 ps, or 10000 time steps. Again, note the absence of any drift in the calculated total energy. The total energy was conserved to within $6.59114 \times 10^{-6} \pm 3.85026 \times 10^{-6}\%$.

Passivated crystalline diamond

Fig. 2.7 shows the time evolution of the total energy, potential energy, and temperature for an NVE integration of a crystalline diamond {111} surface, passivated by one monolayer of H. The time step was 0.2 fs, and the total integration time was again 2 ps, or 10000 time steps. In this run, the total energy was conserved to within $1.47598 \times 10^{-5} \pm 9.86834 \times 10^{-6}\%$.

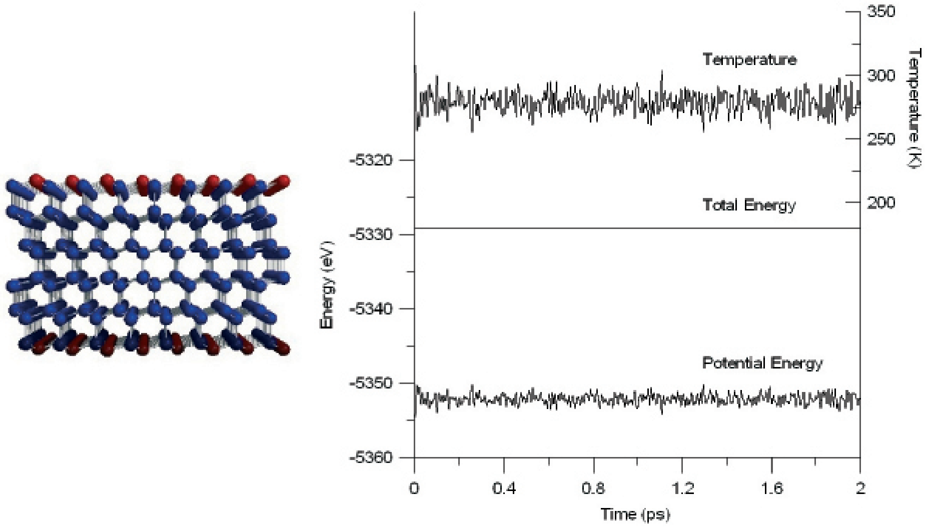

Figure 2.6: Diamond {111} surface, and the time evolution of its total energy, potential energy and temperature.

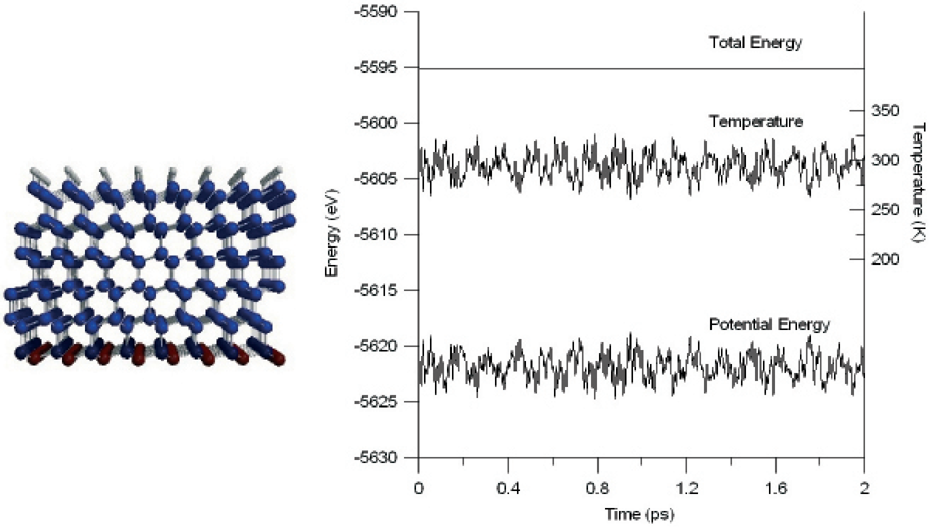

Figure 2.7: Diamond {111} surface passivated with H, and the time evolution of its total energy, potential energy and temperature.

Amorphous hydrogenated carbon

Fig. 2.8 shows the time evolution of the total energy, potential energy, and temperature for an NVE integration of a thin a-C:H layer, with a H-content of about 10%. This a-C:H layer was deposited following the methodology as described in 2.5. The time step was 0.2 fs, and the total integration time was again 2 ps, or 10000 time steps. The total energy was conserved to within $7.21440 \times 10^{-6} \pm 5.21463 \times 10^{-6}\%$.

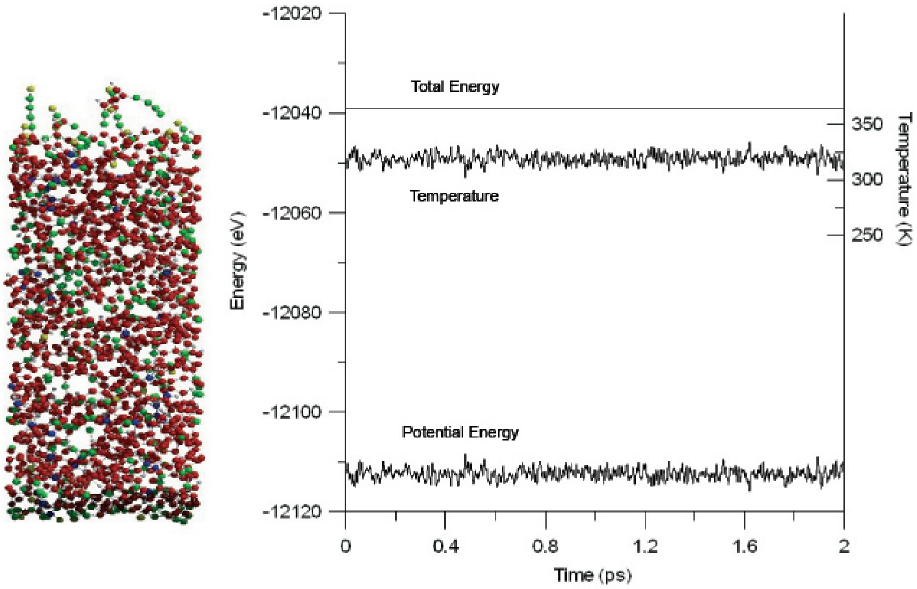

Figure 2.8: a-C:H surface, and the time evolution of its total energy, potential energy and temperature.

CH_3 impact on a a-C:H layer

Fig. 2.9 shows the time evolution of the total energy, potential energy, and temperature for an NVE integration of an impact of a 10 eV CH_3 radical on a a-C:H layer. This a-C:H layer was deposited following the methodology as described in 2.5. The time step was 0.2 fs, and the total integration time was 5 ps, or 25000 time steps. Note the rise in temperature during the first 3 ps of the integration. This is the heating of the surface due to the impact. The total energy was conserved to within $3.01971 \times 10^{-5} \pm 1.68975 \times 10^{-5}\%$.

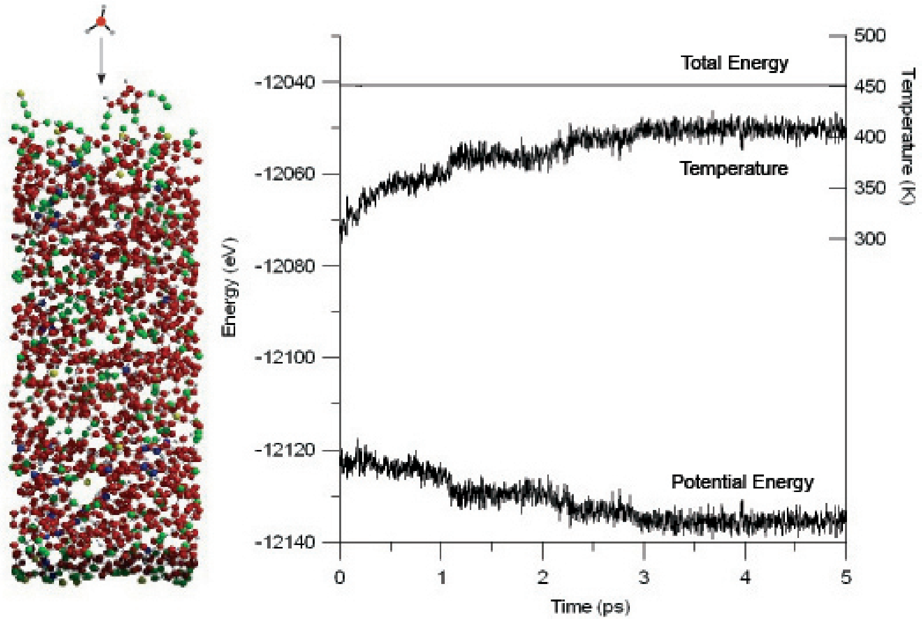

Figure 2.9: Impact of a 10eV CH_3 radical on an a-C:H surface, and the time evolution of its total energy, potential energy and temperature.

2.4.3 Chemisorption energies of several species on a diamond {111} surface

Because the original purpose of the potential was to simulate growth of diamond films, Brenner also calculated chemisorption energies for several radicals on a diamond surface. These energy calculations have been repeated in our work.

In Table 2.6, the chemisorption energies of a H-atom, a methyl radical, an ethynyl radical, a H_2 molecule, an acetylene molecule and an ethene molecule on a H-terminated diamond {111} surface are given. It can be seen from the Table, that the values for H_2 and C_2H_2 correspond to the values reported by Brenner, while the other values slightly differ. It should be noted, however, that the dimensions of the diamond structures are not explicitely stated in Brenners original publication. Also, it is unclear which energy minimalization technique Brenner used for his calculated values, and what energy tolerance was used (i.e., the criterion determining

Table 2.6: Chemisorption energy values (in eV) on a diamond {111} surface for several species.

Species	Current work	Brenner
H	-4.1	-4.2
CH_3	-3.9	-4.0
C_2H	-4.2	-4.1
H_2	-3.6	-3.6
C_2H_2	-4.9	-4.9
C_2H_4	-4.2	-4.3

when a structure is considered to be minimized).

2.4.4 Bond energies and bond lengths

Notwithstanding the fact that some of the calculated chemisorption energies differ slightly from the values reported by Brenner, the inferred bond lengths and bond energies do match. The calculated C-C bond lengths for the chemisorbed ethynyl radical (mistakenly termed "acetyl radical" by Brenner), and the acetylene and ethene molecule are given in Table 2.7.

Table 2.7: Calculated C-C bond lengths (in Å) of the chemisorbed species from Table 2.6.

Species	Current work	Brenner
C_2H	1.29	1.29
C_2H_2	1.39	1.39
C_2H_4	1.57	1.57

In Table 2.8, the calculated values for the C-H and C-C bond energies in several hydrocarbons are given, along with the values reported by Brenner. Again, it can be seen that all values correspond fairly well, with deviations of 0.001 eV or less. Also given are the bond lengths, as well as the vacancy formation energy for diamond. All calculated values correspond to the values reported by Brenner. Hence, we may conclude that the Brenner potential is correctly implemented in our code, resulting in reliable calculations.

2.5 Methodology for simulating thin film growth

In this section, the general methodology followed in this thesis for particle impacts on a surface and thin film growth will be described. Specifications for the different simulations carried out in this work will be given in the appropriate chapters. To begin a simulation, a substrate first needs to be defined. This initial surface can either be a freshly generated crystal structure, or (part of) a structure previously created. This initial substrate is equilibrated at the desired temperature using the Berendsen heat bath. The lower atomic layers (typically a few hunderd atoms) are kept fixed, preventing the simulation cell to translate due to momentum transfer from the impacting particles. In using this static layer, we assume that all of the interesting physics and chemistry is occurring in the top layers of the film. In Fig. 2.10, an example of a diamond {111} substrate containing 728 atoms (lefthand side), and an example of a thin a-C:H layer, containing 1000 atoms (righthand side), is shown. All structures depicted in this thesis are rendered using the freeware rendering program *Raster3D* [157]. The package can be downloaded from

`http://www.bmsc.washington.edu/raster3d/raster3d.html`

Table 2.8: Calculated bond energies (*BE*) and bond lengths (*BL*) for basic hydrocarbons and for diamond, and the corresponding values as reported by Brenner [3]. Bond energies are expressed in eV, and bond lengths in Å.

Property	Current work	Brenner
Bond Energies		
C-H BE CH_4	-4.393	-4.393
C-H BE C_2H_6	-4.362	-4.362
C-H BE C_2H_4	-4.363	-4.362
C-H BE C_2H_2	-4.362	-4.362
C-C BE C_2H_6	-3.546	-3.547
C-C BE C_2H_4	-6.174	-6.175
C-C BE C_2H_2	-8.424	-8.424
BE diamond	-7.323	-7.323
Bond Lengths		
C-H BL C_2H_6	1.07	1.07
C-H BL C_2H_4	1.07	1.07
C-H BL C_2H_2	1.07	1.07
C-C BL C_2H_6	1.55	1.55
C-C BL C_2H_4	1.38	1.38
C-C BL C_2H_2	1.29	1.29
BL diamond	1.54	1.54
Vacancy formation energy	.	.
VFE diamond (eV)	-7.2	-7.2

The code for translating the configuration files of the MD program into the Raster3D format was written by C. Abrams, and was extended in this work to allow bond energy dependent ball-and-stick representation of structures and new coloring modes.

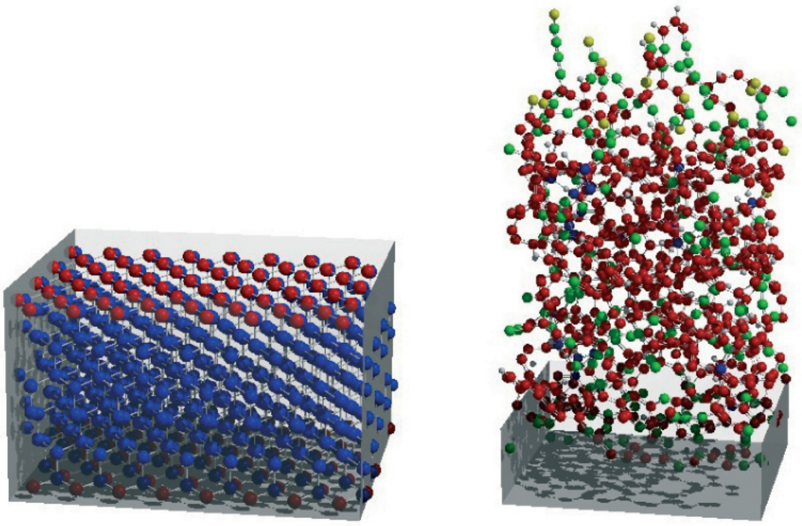

Figure 2.10: Diamond {111} substrate, containing 728 atoms (lefthand side), and a thin a-C:H layer, containing 1000 atoms (righthand side). The grey {x,y}-planes are the periodic boundaries. Blue balls are 4-coordinated C-atoms, red balls, green balls and yellow balls are 3-, 2- and 1-coordinated C-atoms, respectively, and the small grey balls are H-atoms.

The impacting species can be chosen either manually, or from a pool of species using a random number. In the latter case, each species is assigned a "relative flux". The relative flux of each species is defined as the fraction of particle impacts by this species. For example, if the relative flux of *e.g.* a C-atom is 0.2, then there will be about one C-impact out of every five impacts, on average. The sum of all relative fluxes equals 1. For each specific impact number, a random number in the interval [0,1] determines which species is selected. The particle, belonging to the selected species, is then positioned above the substrate beyond the cutoff of the potential. The $\{x,y\}$ position of the particle can be user-defined, or determined randomly using two random numbers. In the case of a polyatomic species, the rotational angles are also randomized. The particle is also given a translational energy, and an impact direction, requiring both the azimuthal angle and the polar angle. The particles are also allowed to vibrate and rotate: the atoms of the molecule are randomly displaced from their equilibrium positions, such that the difference in energy between the resulting molecule structure and the equilibrium molecule structure equals the desired value. Then the particle is allowed to move towards the substrate where it interacts with the surface atoms. During the impact, the heat bath is switched off.

Each particle impact was followed for 2 ps, using a time step of 0.2 fs. Although the impact time is rather short, it is sufficient for the cases studied in this thesis: the particles were usually given a thermal energy in the order of 0.1 eV. Clearly, this will not induce any temperature spike, and the moderation of the particles' kinetic energy to the substrate's temperature occurs within a few hunderd timesteps. Nevertheless, a small temperature increase of the substrate does occur. Hence, after 1.6 ps, the heat bath is switched back on. However, to limit the influence of the heat bath and to remain close to the microcanonical ensemble, only a few atomic layers, above the fixed atoms, are included in the heat bath. After the impact, any unbonded atoms are removed, as well as clusters not bound to the substrate (i.e., clusters moving away from the substrate). A flow-chart of an MD program execution is shown in figure 2.11.

For the simulation of thin film growth, the resulting surface after impact i is the input surface for impact $i + 1$. After growth, the structure is allowed to relax during 5 ps using the heat bath, followed by another 5 ps without the heat bath. Quantities of interest are obtained as time-averages during the relaxation stage without the heat bath. Information regarding sticking coefficients or reaction mechanisms are also obtained after the growth simulation has been completed. Each individual impact is analysed separately, and sticking coefficients are obtained as averages over the entire growth simulation. Hence, the obtained values are relevant for an "average" surface.

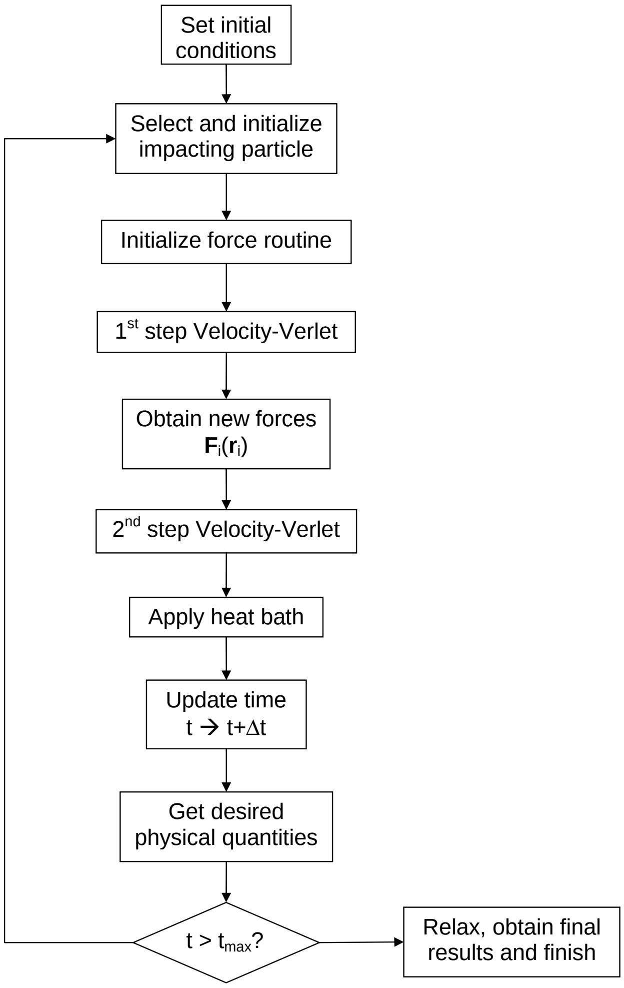
Set initial conditions
Select and initialize impacting particle
Initialize force routine
1st step Velocity-Verlet
Obtain new forces Fi(ri)
2nd step Velocity-Verlet
Apply heat bath
Update time t → t+Δt
Get desired physical quantities
t > tmax?
Relax, obtain final results and finish

Figure 2.11: Flow-chart representing the basis execution of an MD program.

Alternatively, sticking coefficients can also be obtained on specific surfaces (cfr. chapter 5). Here, the same surface was used as input substrate for the particle impacts. Quantities of interest are then obtained by simple averages over all post-impact configurations. The set of all post-impact configurations forms an ensemble of microscopic states corresponding to a macroscopic state of a surface under bombardment by species of a certain energy, direction and type.

2.6 Speeding up the code

The original code of the MD program used in this thesis was written by Cameron Abrams [158]. In order to extend the capabilities of the code, some changes have been made to this code. Most of the changes were focussed on improving the code's performance.

As a first step to improve the code's performance, the compiler assisted profiling tool *gprof* was used. *Gprof* yields a profile of the code, indicating how much time was spent in each function. Analysis and subsequent tuning of the code on the basis of these profiles resulted in a increase in speed of about 30%.

In order to further speed up the calculation, the so-called *cell-method* was implemented, following Rapaport [121]. The idea of this cell-method technique is to limit the number of possible atomic interactions by placing the atoms in virtual cells with dimension greater than or equal to the cutoff of the interatomic potential. Only those atoms that are located in either the same cell or in neighboring cells can interact with each other.

Specifically for growth of thin films, a non-conventional method was used to further increase the calculation speed. First, growth was initiated on a substrate as described above. After a sufficient number of impacts, depending on the growth conditions, growth was stopped, and part of the substrate was removed. For example, growth of a film was initiated on a substrate containing maybe 500 atoms, and continued until 1500 atoms were deposited. Then, the lower half of the film was removed, of which the lower atomic layers were fixed again. The new, smaller substrate was equilibrated again and growth was continued on this smaller substrate. This process was continued, until the desired number of atoms in total were deposited. The different pieces were then glued together again, to obtain the final structure. This structure was then equilibrated and relaxed as described above.

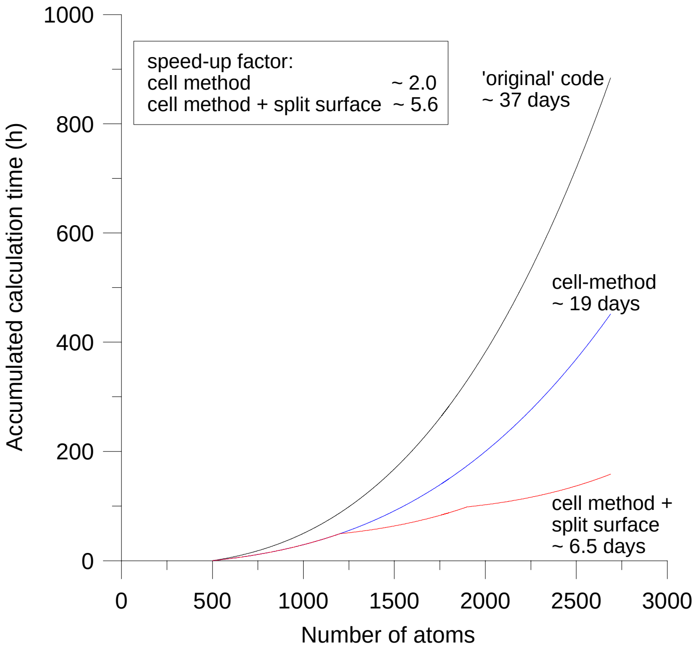

Figure 2.12: Effect of speeding up the code, using the cell-method and the split-method (see text). The calculation time (in hours) reflects the time needed to simulate the deposition of 2188 atoms initiated on a 500 atom substrate on a single AMD Athlon MP 2600+ processor.

This procedure assumes that removing the lower half of the film (or about half of the film), does not influence the deposition process. This condition is not violated in the simulations as carried out in this work, due to the very low energy of the particles: the impacts do not result in an important momentum transfer to the substrate, nor in a temperature spike. The advantage of this method is that the number of interatomic interactions that need to be calculated decreases substantially, and hence also the calculation time. In Fig. 2.12, the effect of using this "*split-method*" on the calculation time is shown. Also shown is the calculation time using the original code of C. Abrams, and the introduction of the cell-method in the code. Note that the speed-up factors and the total calculation time of all three simulations were obtained after the initial *gprof* analysis and tuning.

2.7 Aim of this work and structure of the thesis

The aim of this work is twofold. First, a better understanding of the specific expanding thermal plasma (ETP) deposition process of thin a-C:H films under different conditions was desired (see p. 13). More specifically, most of the ETP plasma chemistry was already investigated, and this information is now complemented by a more detailed understanding of the actual deposition process. Second, information is obtained which is relevant for *any* deposition system in which film growth proceeds by low-kinetic energy hydrocarbon radical surface chemistry.

A first step to reach these goals was to simulate the growth and the structure of a-C:H films deposited by the ETP deposition system. These early simulations were based on the information which was experimentally available at that time. The results of these simulations are shown in chapter 4.

Later experiments, however, revealed several adjustments to these input data, especially regarding the growth species. It was realized that a more fundamental understanding of the film growth was necessary. Therefore, simulations have been carried out to investigate how different hydrocarbon radicals react with predefined sites, characteristic for thin a-C:H films. The results of these simulations are given in chapter 3.

Because the goal of this work was not only to understand ETP-based growth of thin a-C:H films, but to obtain a more general understanding of a-C:H film growth, simulations were also performed to study the influence of the impact angle and the vibrational and rotational energy of the species. Indeed, these data are usually not known, and hence, we wanted to investigate their effect on the impact behaviour of the various species. However, these simulations were not specifically based on the ETP set-up and are, therefore, more generally valid as well. The results are given in chapter 5.

The simulations providing more basic and general information regarding the reaction behaviour of several hydrocarbon radicals, as well as the preliminary growth simulations, enabled us to start investigating the growth of a-C:H films specifically designed for ETP conditions. In a first attempt, $F > 1$ conditions were chosen (i.e., acetylene flow is higher than the Ar ion flow, and the main growth species are C_3 and C_3H; see section 1.4.5). Simulations of actual film growth were performed, also providing more basic information regarding the sticking behaviour of the different isomers of the growth species. The results are presented in chapter 6.

However, it was realized that the simulations did not yet match the experiment very well. Therefore, simulations were started to investigate thin film growth under both $F < 1$ and $F > 1$ conditions, including the effect of the additional H-flux. Indeed, the actual H-flux is not known, and the observed H-content in the film cannot be explained from the C-containing growth species alone. Therefore, an additional H-flux towards the substrate must be present. For $F < 1$ conditions (i.e., acetylene flow is lower than Ar flow, and the main growth species are C, CH, C_2 and C_2H), good agreement with experiment was obtained. These results are shown in chapter 7.

The results for the $F > 1$ conditions, however, still did not correspond very well to the experiments. Therefore, the influence of an additional C-flux was also investigated, corresponding more to $F \sim 1$ conditions. On the basis of the results of the $F < 1$ conditions and the reaction behaviour of the C-atoms, it was expected that an additional C-flux could possibly yield a better agreement with experiment, corresponding to $F \gtrsim 1$ conditions. The results of these simulations are given in chapter 8.

Combining the data obtained in these simulations provides a better understanding of the actual chemistry at the surface of a-C:H films. A better understanding of the ETP-based deposition process is indeed obtained. Second, more general conclusions can also be drawn from the results obtained.

These conclusions, and a general overview of the chemistry of the a-C:H deposition process, are summarized in chapter 9.

Chapter 3

Initial simulation of the growth of a-C:H films from hydrocarbon radicals

Abstract

In this chapter, simulations have been performed to study the formation of a-C:H films grown from low energy hydrocarbon radicals ($<$ 2 eV). With these simulations, insight is gained in the processes occurring in this type of deposition. The initial surface is a previously deposited DLC surface; impinging particles include Ar^+ ions with an energy of 2 eV as well as several hydrocarbon radicals and molecules, and hydrogen atoms, with an energy of 1 eV. Two different radical flux compositions were examined: in the first condition, only C, C_2 and CH were used as growth species, as well as a large flux of H atoms. In the second condition, the same carbon radicals were considered, as well as the C_2H radical and C_2H_2, C_4H_2 and C_6H_2 molecules, but without the H-atom flux. These fluxes are similar to typical experimental conditions in an expanding thermal Ar/C_2H_2 plasma (ETP), using different in-fluxes of acetylene, as was revealed by early experiments [159].

However, later experiments indicated that other species, more specifically C_3 and C_3H, are also important growth precursors. These species should therefore also be included in the model as will be demonstrated in later chapters. Several properties of the resulting films will be presented, focussing mainly on the carbon coordination and on the bonding network. The simulations suggest that lowering the acetylene in-flux results in films having a more extensive bonding network, but with more H incorporated. This leads to more polymeric films, having a less diamond-like character, as is evidenced also from experiments. The aim of this work is twofold. The first objective is to compare the structural composition of the simulated films to the structure of the experimentally deposited films, applying similar conditions. Second, the simulations can give us valuable information about the key mechanisms in the deposition process. The material presented in this chapter is published in Diamond and Related Materials.

3.1 Introduction

As a first step towards a better understanding of hydrocarbon radical based deposition of thin a-C:H films, MD simulations of thin film growth are carried out on the basis of experimental data. The species bombarding the substrate, as well as their energies and fluxes, are adopted from a specific experimental deposition of DLC films from an expanding thermal C_2H_2/Ar plasma by Benedikt *et al.* [65], and are given in Table 3.1. Note that later experiments revealed that (a) C_3 and C_3H are also important growth precursors, which need to be included in the model; and (b) the C_4H_2 and C_6H_2 species are in fact background species, not contributing to the film growth. The results related to these later experiments will be presented in following chapters.

All impacts are normal to the surface, with a predefined energy of 1 eV/molecule for hydrocarbons, and 2 eV for the Ar^+ ions. The incident particle was initially placed at a distance above the substrate beyond the cutoff of the potential. The position in x and y direction was chosen randomly. Each trajectory is run for 1500 timesteps, equal to 0.75 ps/impact. Films of about 2.5 nm were simulated. After deposition, the film is allowed to relax for 20 ps at a constant temperature of 523K. Output data are gathered averaging over the last 10 atomic configurations determined at intervals of 50 fs, thus corresponding to the last 0.5 picosecond of relaxation.

Table 3.1: Species, fluxes and energies of particles arriving at the substrate for both conditions, adopted from the experiments.

Condition	Species	Flux (x 10^{21} $s^{-1}m^{-2}$)	Energy (eV)
1	C_2H_2	0.0*	/
	Ar^+	2.300	2
	H	5.302	1
	C_2	1.330	
	CH	0.796	
	C	0.796	
2	C_2H_2	2.650	1
	C_2H	2.210	
	C_4H_2	1.330	
	C_6H_2	0.442	
	C_2	0.221	
	CH	0.133	
	C	0.133	

* consumed entirely in the plasma chemistry

Simulations have been carried out for 2 different conditions. Experimentally, these conditions are similar to a different flux of C_2H_2 through the injection ring in the expanding thermal plasma. For condition 1, a low acetylene in-flux was assumed; for condition 2, the in-flux was assumed to be high. In both conditions, argon is present in the discharge, but only in condition 1, Ar^+ ions were detected at the substrate. As mentioned above, these simulations are relevant for deposition sources such as the ETP source. This is a remote plasma, where the argon thermal plasma at subatmospheric pressure is first created in a cascaded arc with an argon flow. At a constant arc current, a constant flow of Ar^+ ions and electrons into the reactor is maintained. The argon thermal plasma expands into the low-pressure vessel. In this type of plasma, the electron temperature is below 0.3 eV, resulting in a low substrate selfbias (< 2eV) and hence negligible ion bombardment on the sample during the deposition. Further details on the operation of the expanding thermal plasma can be found in references [18-19] and references therein.

Electron energy loss spectroscopy (EELS) was used to investigate the bonding of the experimentally deposited films [20]. The species included here were chosen on the basis of Cavity Ring Down Spectroscopy (CRDS) measurements [18]. The flux-values for the H-atoms, however, were estimated to correspond to the experimental H-concentration in the film, since no experimental data on the H-flux were available. The H-flux for the second condition was assumed to be zero, implying that all the H incorporated in the second film is due to the bombarding hydrocarbons only.

The species included in the model, along with their fluxes to the substrate, are given in Table 3.1 for both conditions. The absence of acetylene in condition 1 is due to the complete consumption of the acetylene in the plasma chemistry. It should be noted that the fluxes have no real meaning here, since every trajectory for every particle was calculated for 1 ps. Therefore, only the relative fluxes are important, indicating the ratios of the impinging particles. Finally, it should also be mentioned that there is considerable uncertainty concerning the particle fluxes as determined experimentally.

For the first film, which was deposited under condition 1, 2304 atom and molecule impacts were performed on the surface, of which 510 Ar^+ ions, 1158 H and 188 C atoms, and 278 C_2 and 170 CH radicals. The net result is the addition of 1019 atoms to the film, of which 466 H-atoms, and 553 C-atoms. For the second film, deposited under condition 2, there were 1597 atom and molecule impacts on the surface, of which 583 C_2H_2, 312 C_4H_2 and 104 C_6H_2 molecules, 487 C_2H, 46 C_2, 33 C and 32 CH radicals. In total, 954 atoms were added to the surface, of which 283 H-atoms and 671 C-atoms.

3.2 Results and discussion

3.2.1 General microscopic structure of the deposited films

In Fig. 3.1, the simulated microscopic picture of both deposited films is shown. The film deposited under condition 1 (called here in brief “first film”), is 24 Å thick, and the second film is 28 Å thick. These pictures already show a few general characteristics of both films: the first film shows fewer voids and more 4-coordinated carbons than the second film. Also, the second film is somewhat thicker than the first film but has a lower density. It is also clear from the pictures that the H-concentration in the first film is higher than in the second film. Also the microcrystalline structures differ in both films. These characteristics will be explained in the following sections.

The occurrence of rings in both networks has also been determined, as shown in Table 3.2. No rings with more than 6 members were found, and only 1 aromatic ring was found: a 6-membered ring in film 2. All other rings consist of a mixture of 3-coordinated and 4-coordinated carbons. However, the simulated films are too small, and they contain not enough atoms, to draw definite conclusions from these data.

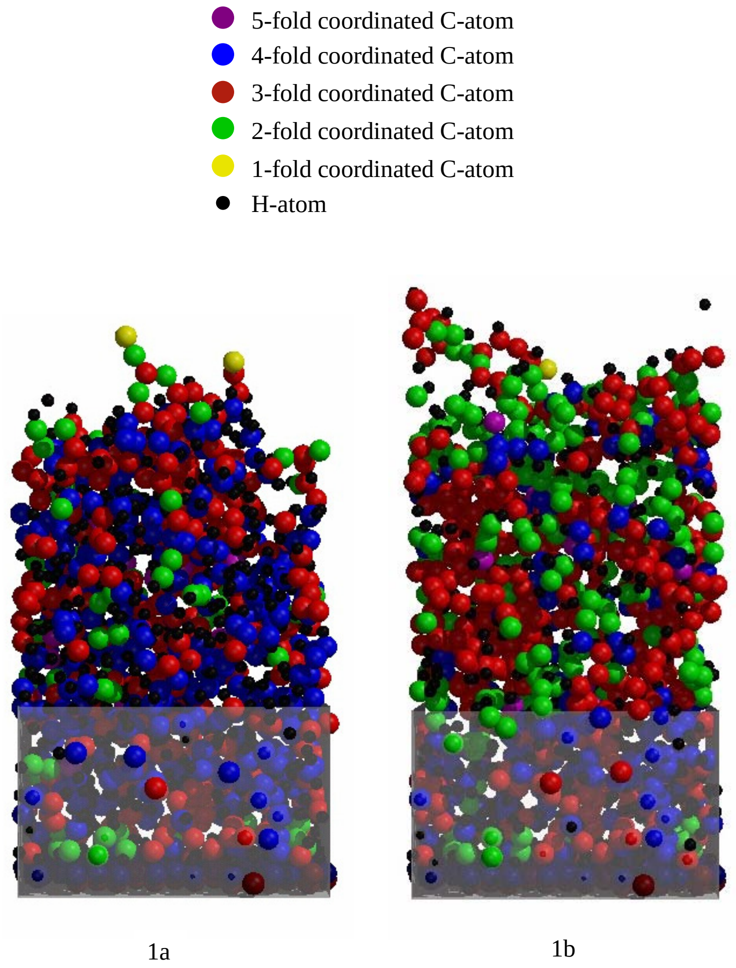
5-fold coordinated C-atom
4-fold coordinated C-atom
3-fold coordinated C-atom
2-fold coordinated C-atom
1-fold coordinated C-atom
H-atom
1a
1b

Figure 3.1: Side view of the simulated films for condition 1 (figure 1a) and condition 2 (figure 1b). It can be seen that the film of condition 1 shows fewer voids in its structure, and contains a much higher fraction of 4-fold coordinated carbon atoms, as compared to the film of condition 2.

3.2.2 Coordination in the films and mechanisms of film growth

In the bulk, the average coordination number for the first film is calculated to be 3.4; for the second film, it is 2.7. The model as it is used for this work does not allow to calculate the hybridisation of the atoms in the deposited films. Therefore, one of the most important characteristic properties of DLC on the microscopic level, i.e., the sp^3 fraction, cannot be calculated. Instead, the fraction of 4-fold

Table 3.2: Calculated occurrence of rings for both conditions.

	3-ring	4-ring	5-ring	6-ring	>6-ring
film 1	2	1	3	1	0
film 2	2	0	1	3	0

coordinated carbon atoms is calculated, which is supposed to be a realistic measure for the sp^3 fraction in the film. In Fig. 3.2, this fraction, for the two conditions, is shown as a function of depth in the film.

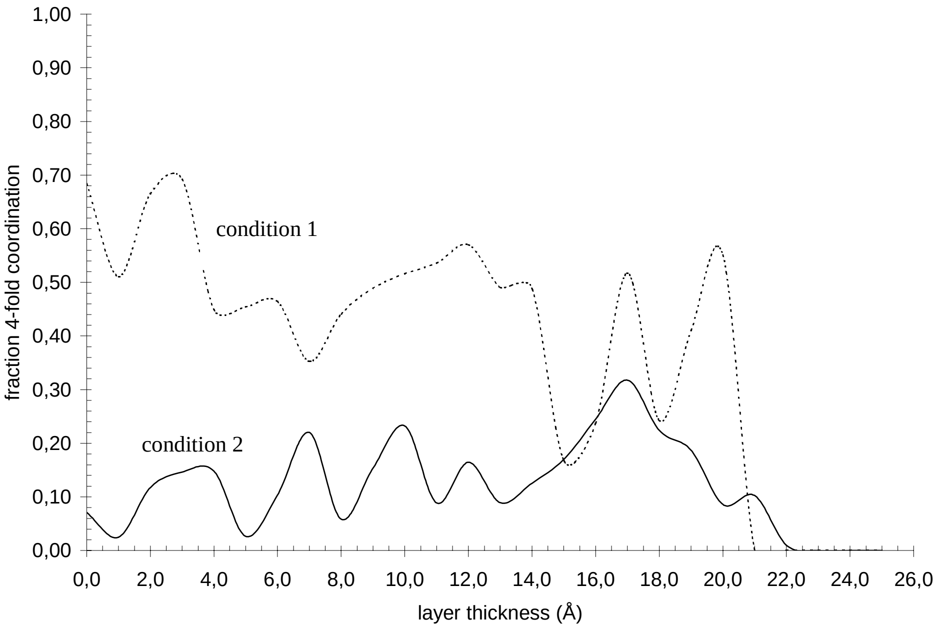

Figure 3.2: Calculated fraction of 4-fold coordinated carbon atoms for condition 1 (dashed line) and condition 2 (solid line) as a function of position in the film. The initial substrate on which the film was grown starts at 0.0 Å, and extends to the left (not shown).

It can be seen in the figure that the 4-fold coordination heavily fluctuates with depth in the film, and becomes zero near the surface (right hand side of the figure). In the first film, the top 3 Å contains no 4-fold coordinated atoms; in the second film, there are no 4-fold coordinated atoms in the top 5 Å.

The fact that no 4-fold coordination is present in the top few Å of both films is a consequence of the growth mechanism: since no high-energy particles are present, there can be no subplantation. Therefore, the films grow by chemisorption of incoming radicals on the surface. Hence, almost every incoming atom will initially be either 1-fold, 2-fold or 3-fold coordinated. Therefore, for an atom to become 4-fold coordinated, it must be covered by new incoming atoms, such that it becomes embedded in the bulk.

From Fig. 3.2, it is clear that the 4-fold coordination number in the bulk is higher in film 1 than in film 2. This can also be seen in Fig. 3.1. For the first film, the fraction of 4-coordinated carbons in the bulk is on average 0.50; for the second film, this fraction in the bulk is on average 0.16. It is worth to mention that in order to calculate the 4-fold coordination in the bulk, the upper atomic film included must be covered by at least one more complete monolayer. For condition 1, this upper monolayer is situated at 16.0 Å; for the second condition, it is located at 19.0 Å.

Since the hybridisation of the atoms cannot be determined in this model, direct comparison with experiments is not possible. However, when we identify the fraction of 4-fold coordinated carbon atoms with sp^3 hybridisation, an indirect comparison can be made. Experimentally, EELS measurements of the deposited films show an sp^3 fraction of 0.67 for the first film [160], which indicates a reasonable agreement with our simulated result of 0.50 for the 4-fold coordinated fraction. The EELS data show a value of 0.53 for the sp^3 fraction in the second film [160], which is not in good agreement with our result of 0.16.

Two factors should be considered when interpreting this result. First, the uncertainties concerning the particle fluxes should be taken into account when comparing the simulation results and the experimental measurements, as well as the uncertainty regarding the EELS measurements [160]. These uncertainties are the same for both layers. Second, comparing the calculated 4-fold coordinated fraction of the second film to the experimentally determined sp^3 fraction, it is clear that these values do not correspond. It should be noted that both the C_3 and C_3H radicals have not been included in the model. Indeed, later measurements revealed that these species are also formed in the plasma and play an important role in film growth under condition 2. Their effect on the resulting a-C:H film is investigated in chapter 6.

The higher average coordination number, and more specifically, the higher 4-fold coordination number predicted by our model for the first film compared to the second film, is a result of the different growth species in both conditions. In Fig. 3.3, the sticking and etch efficiency of the different species are shown for both conditions. Only the species with a high sticking efficiency are shown. For condition 1, it is clear from the figure that not the H-atoms, but the C_2 radical is the most efficient etching species. In only 2.7% of the H-impacts, material was etched from the surface, and the main etch product was H_2 (in 80.0% of the etch events); also C_2H_2 and C_2H were etched, but to a minor extent. The C_2 radical, however, etches material away in 28.1% of its impacts, and in most of these events, C_2H was the etch product, thus creating dangling bonds at the surface by removing hydrogen. The same conclusion regarding the etch efficiency of C_2 can be made for condition 2: in all etch events, the etch product was C_2H. Although under condition 2 the etch efficiency itself is also rather high for C_2 (30.4%), the effect is small due to the very low relative flux of C_2: only 2.9% of the impacts under condition 2 is a C_2 radical. In total, only 14 H-atoms were removed from the surface due to C_2 etching.

The contribution of the different species to the growth of the layer is shown in Fig. 3.4. For condition 1, the main growth species is found to be C_2, responsible for over 68% of the carbon atoms in the final film. This is a direct result of (i)

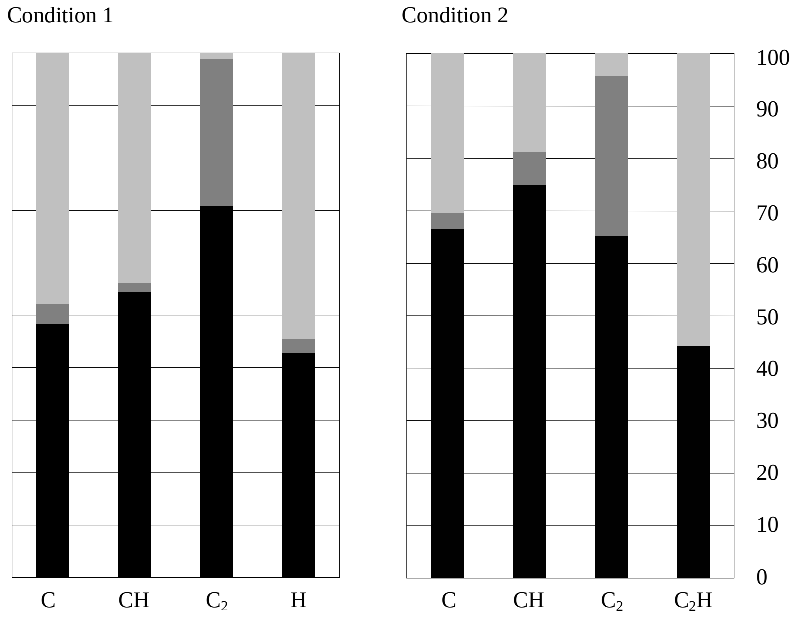

Figure 3.3: Calculated sticking and desorption efficiencies of the main growth species under condition 1 (left panel) and condition 2 (right panel). The black areas indicate the sticking efficiencies, the dark grey areas indicate the etching efficiencies, and the light grey areas indicate the fraction of events where neither sticking nor etching occurred. Only the species with a high sticking efficiency are shown.

its high relative flux (43.6% of all C-containing species under condition 1 is C_2), (ii) the fact that it brings 2 carbon atoms to the surface per impact (60.7% of all carbon atoms arriving at the surface), and (iii) its high sticking efficiency (70.9%). The role of the H-atoms is primarily to passivate dangling bonds: under these conditions, the H is not an efficient etching species (see above), but simply binds to the surface in 42.8% of its impacts. Due to its high relative flux, it is the main source of hydrogen in the film under condition 1 (84.5%).

The most important growth species under condition 2 is C_2H: 63.4% of the C-atoms and 70.5% of the H-atoms in film 2 is incorporated through C_2H impacts. Only 6.8% of the carbon atoms in this film comes from growth species that do

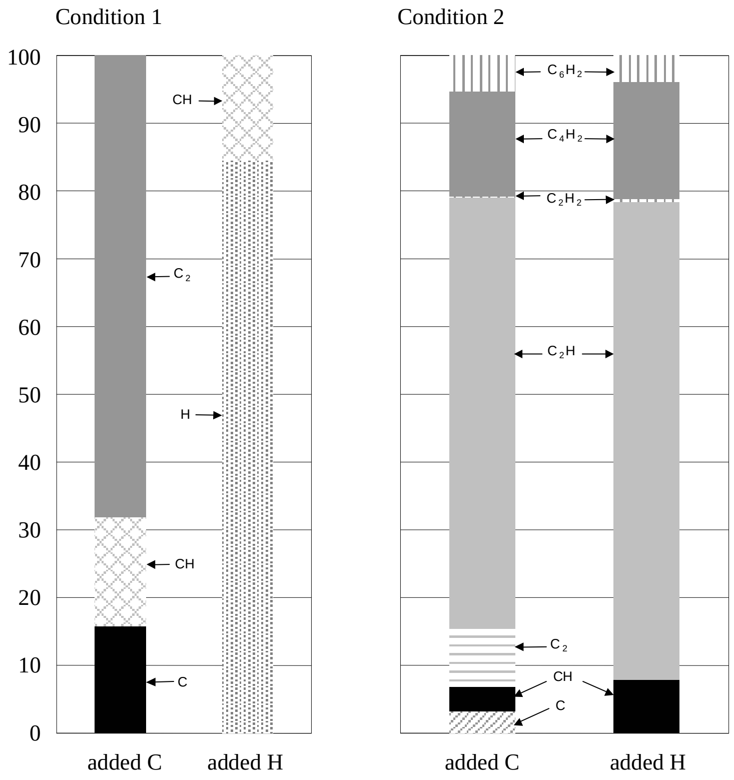

Figure 3.4: Calculated contribution of the different species to the growth of the film, in terms of the fraction of carbon atoms and hydrogen atoms added to the film by each species, under condition 1 (left panel) and condition 2 (right panel).

not have a double bond, i.e., C and CH. The most important growth species, i.e., C_2 under condition 1 and C_2H under condition 2, both contain a triple bond. However, an impinging particle will more easily become 4-fold coordinated when it has no double or triple bonds, since these species require that the double and triple bonds become saturated by incoming H-atoms or incoming radicals in order to become 4-fold coordinated. In condition 1, all growth species are very reactive, and more than 30% of the carbon added to the film comes from particles (C and CH) not having a double or triple bond. In condition 2 on the other hand, 4-fold coordination is more difficult to obtain, since in this case, the most important growth species is C_2H. This radical has two resonance structures, with a double and a triple bond respectively, resulting in a carbon-carbon bond order of 2.5. This carbon-carbon bond has to be saturated before 4-fold coordination can occur. The same is true for C_4H_2 and C_6H_2: both are stable molecules, containing triple bonds. Although both have a rather low sticking efficiency (8.3% for C_4H_2 and 5.8% for C_6H_2), they are responsible for 20.7% of the added carbon to the film. Also, there is no H-flux present for this condition to saturate this unsaturated bond and to passivate dangling bonds at the growing surface. Both factors contribute to the dramatic lowering of the 4-fold coordination compared to the first condition, as predicted with our model. The higher fraction of 4-fold coordination in the first film is also reflected in the radial distribution function (RDF), which we will discuss in the next section.

Finally, while the 2-fold coordination in the first film is relatively low (0.09), it is very high in the second film (0.29). This is also a consequence of the nature of the growth species, which are highly unsaturated, as well as the lack of an atomic H-flux.

3.2.3 The Radial Distribution Function

Equally important to determine the microstructure of the simulated films is to calculate the radial distribution function (RDF), and more specifically, the 4-4 RDF, indicative for the fraction of 4-fold coordinated C-atoms bound to other 4-fold coordinated C-atoms. This fraction is important, since it constitutes the bonding network, giving the structure its mechanical hardness and rigidity. The RDF measures the probability of finding an atom at a distance r from any other atom, relative to the same probability in an ideal gas at the same overall number density. Therefore, it constitutes a normalised distribution of interatomic distances. In a crystalline material, like diamond, the atoms are situated at well defined positions, and the RDF will therefore show well defined peaks and valleys over a long length scale, implying long range order. In an amorphous material, however, the atoms are not localised at well defined positions, and therefore, no peaks will appear in the RDF except at first neighbour distances.

In Fig. 3.5, the 4-4 RDF is shown for both DLC films, indicating the number of pairs of atoms both having 4 neighbours. It can be seen that there is no long range order, as there are no peaks beyond ~ 2.65 Å, as is expected for these DLC films. There is, however, a medium range order, as indicated by the second peak at about 2.65 Å. Since the peak at 1.55 Å for film 1 is much larger than it is for film 2, the 4-4 RDF shows that there is much more 4-4 coordination in the first film. This indicates a more rigid structure. Also the second-nearest-neighbours are more strongly coordinated in the first film than in the second film, shown by the larger peak at 2.65 Å for film 1.

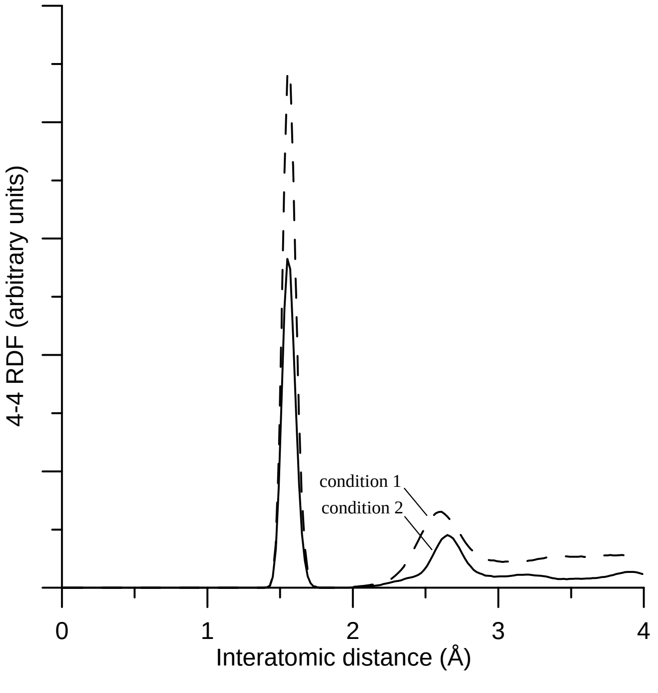

Figure 3.5: Calculated 4-4 RDF for film 1 (dashed line) and film 2 (solid line).

In Fig. 3.6, the total carbon-carbon RDF is shown for both films. The first peak, at about 1.3 Å, shows up due to 2-fold coordinated carbon atoms, bound to either other 2-fold coordinated carbon atoms, 3-fold or 4-fold coordinated carbon atoms. It can be seen that the second film contains a much larger fraction of 2-fold coordinated carbons.

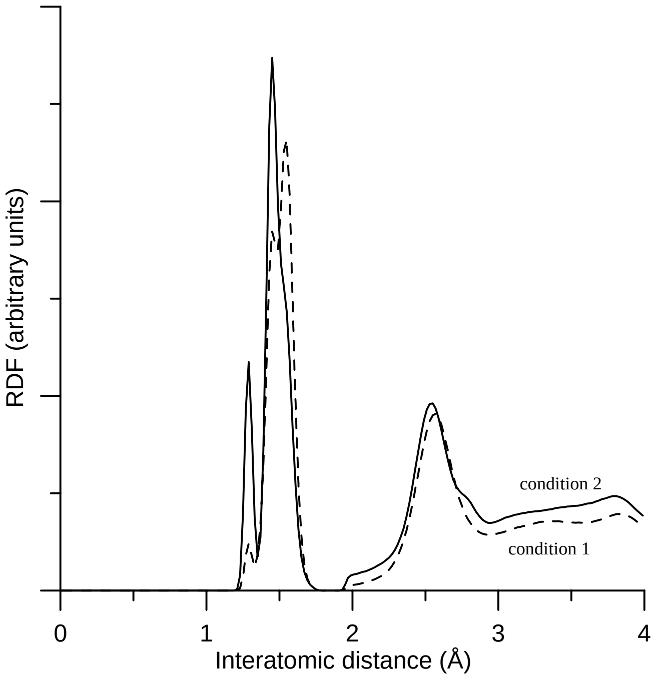

Figure 3.6: Calculated total carbon-carbon RDF for film 1 (dashed line) and film 2 (solid line). The H-atoms are not included in this RDF.

The second peak, at about 1.5 Å, is split in two in the first film. The left peak arises from 3-3 coordinated carbon atoms, while the right peak is a combination of 3-4 and 4-4 coordinated carbon atoms. The importance of this overlap of the 3-3 peak and the 4-4 peak is diminished in the second film to a barely visible shoulder at the right of the main peak at 1.5 Å. This indicates that the fraction of 3-4 and 4-4 coordinated carbon atoms is greatly reduced in the second film as compared to the first film, while the 3-3 fraction is increased. Again, this reflects the lower 4-fold coordination in the second film. The RDF therefore indicates that the first film has a more extensive bonding network than the second film. However, due to the much higher H-content in the first film (resulting in many CH_2 and CH_3 structure fragments, see below), this does not lead to a more diamond-like character of the film, but rather to a more polymeric structure.

3.2.4 Hydrogen content of the films

The average hydrogen content of the films is calculated to be 0.46 for the first film, and 0.30 for the second film. Experimentally, values of > 0.42 and 0.35 were obtained, respectively [160]. The H-fraction in both films, as a function of the film thickness, is shown in Fig. 3.7. It can be seen that the H-content remains fairly constant throughout the film, except at the surface. The fraction of the different CH_x fragments in the films is shown in Table 3.3. Again there is a significant difference between the two films. The reason for this difference is the absence of an atomic H-flux for the second condition, such that all the hydrogen present in the second film comes from the growth species. The H-fraction of 0.30 corresponds to C_2H and C_4H_2 as the main growth species. Since these growth species do not have carbon atoms with 2 or 3 hydrogen atoms, CH_2 and CH_3 fragments in the film can only be formed by breaking a C-H bond, followed by the migration of the H atom to a C atom that is already bound to a H atom. This explains the very low CH_2 and CH_3 fractions in the second film. In the first film, however, the incoming atomic H atoms can easily react with C atoms and CH radicals, which are not yet fully saturated.

3.2.5 Density of the films

In contrast to the large difference in coordination and hydrogen content, the density in both films is practically the same. The density in the bulk of the films is

Table 3.3: Calculated CH_x fractions in both films.

	Condition 1	Condition 2
CH_0	0.353	0.515
CH_1	0.428	0.464
CH_2	0.196	0.021
CH_3	0.023	0

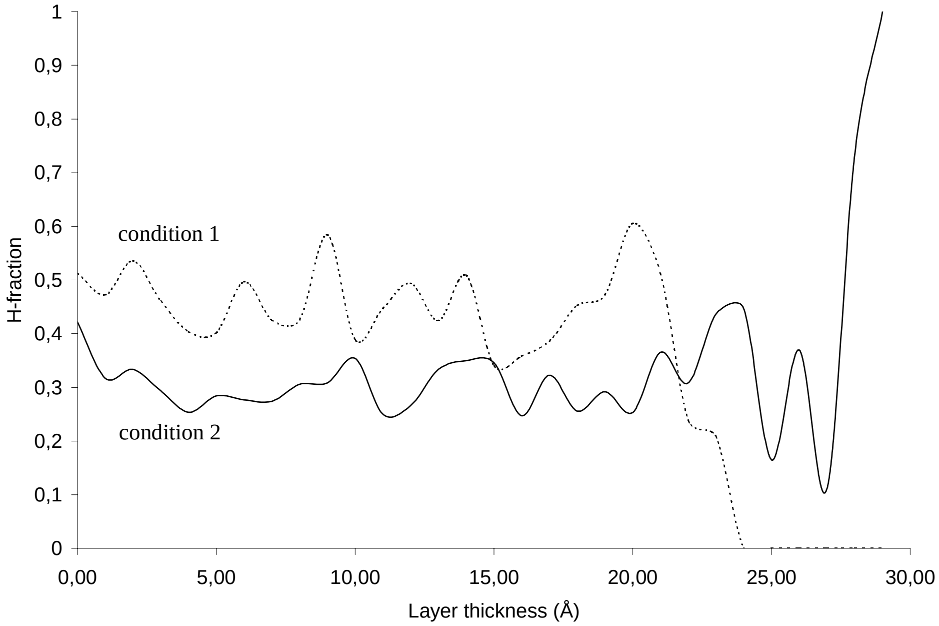

Figure 3.7: Calculated H-fractions for film 1 (dashed line) and film 2 (solid line), as a function of position in the film. The initial substrate starts at 0.0 Å, and extends to the left (not shown).

calculated to be 1.73 g.cm^{-3} for the first film, and 1.75 g.cm^{-3} for the second film. This is a result of the higher 4-fold coordination in the first film (increasing the density), combined with a higher hydrogen content (decreasing the density), relative to the second film.

The evolution of film density for both films as a function of film thickness is shown in Fig. 3.8. It can be seen that the density in both cases fluctuates, showing peaks every ~ 3 Å in film 1, and every ~ 2.5 Å in film 2. The peaks in the density evolution in both films appear at positions with a valley in the H-content evolution, showing the inverse relation between hydrogen content and density. This effect is then balanced by the coordination number to result in similar densities in both films.

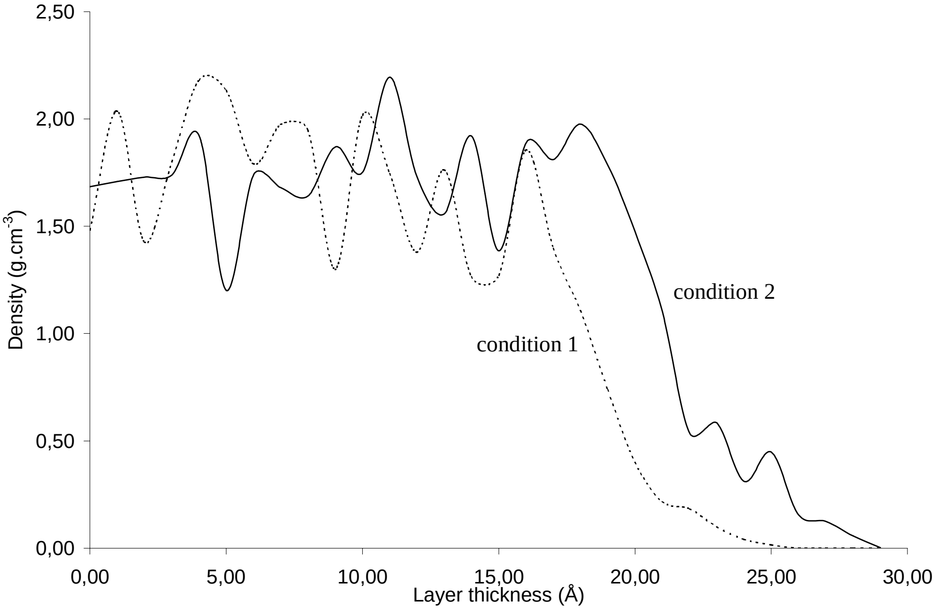

Figure 3.8: Calculated density for film 1 (dashed line) and film 2 (solid line), as a function of position in the film. The initial substrate starts at 0.0 Å, extending to the left (not shown).

3.3 Conclusion

The deposition of a-C:H films for two different conditions was investigated with MD simulations, using the Brenner potential. Growth was accomplished using low-kinetic energy hydrocarbons (1 eV), chemisorbing at the growing a-C:H surface. As an example, the fluxes used in the simulations were taken from expanding thermal plasma (ETP) experiments under two different operating conditions, i.e., different in-fluxes of acetylene through the injection ring of the expanding thermal plasma, resulting in different reactive species reaching the substrate. For the first condition, corresponding to a low in-flux of acetylene, a film was formed with a rather high fraction of 4-fold coordinated carbon atoms (0.50), high hydrogen concentration in the film (0.46) and a rather low density of 1.73 g.cm^{-3}, typical for this type of DLC. For the second condition, corresponding to a higher in-flux of acetylene, our simulations predict the formation of a film containing only a small fraction of 4-fold coordinated carbon atoms (0.16), a lower H-content (0.30) and a similar density (1.75 g.cm^{-3}). The results for the first film correspond fairly well to the experimental data; the results for the second film, however, do not agree so well with the experimental results. As later experiments indicated, the C_3 and C_3H radicals should be included in the model to simulate film growth under this condition. The results for the updated model will be presented in chapter 6.

The results of the present chapter still remain generally valid, and can be explained in terms of the growth mechanism, as well as the growth species and their fluxes towards the substrate. It is shown that under condition 1, the C_2 radical is both the most efficient and important growth and etch species, while the H-atoms are only passivating dangling bonds. More than 30% of the carbon added to the film comes from particles that have no double or triple bonds (C and CH). While the C_2 radical remains the most efficient etch species under condition 2, the C_2H radical becomes the most important growth species. Less than 7% of the carbon atoms in the film originates from C and CH. The radial distribution function indicates that both films have different microstructures: the first film has more extensive coordination than the second film. However, it also contains much more hydrogen, which results in a more polymer-like structure, in agreement with experiments. These simulations suggest that experimental conditions, changing only one parameter in the depositing plasma (i.e., the acetylene in-flux), can have a significant influence on the resulting film characteristics, due to the different species and particle fluxes to the substrate. These simulations also suggest that changing only the growth species, without changing the governing growth mechanism (chemisorption), leads to different films, irrespective of the source used to generate these growth species.

Chapter 4

Reaction mechanisms of a-C:H growth precursors on selected a-C:H sites

Abstract

In this chapter, reaction mechanisms of several hydrocarbon radicals are investigated on specific sites, relevant for a-C:H thin films. This study has been carried out in order to obtain a more basic understanding of the reaction behaviour of various hydrocarbon radicals. The species whose reaction mechanisms have been studied, include C_2, C_3, linear C_3H and cyclic C_3H. In total, 11 surface sites have been investigated. Several trends in the mechanisms have been established. It is shown that chemical resonance, steric hindrance and structural stability are the main factors affecting the reaction mechanisms. Also, the influence of site-specific factors is addressed. This information is important for a better understanding of the growth of thin a-C:H films from low-kinetic energy hydrocarbons.

4.1 Introduction

As indicated in the previous chapter, a clear understanding of the reaction behaviour of the a-C:H film growth species is important to understand the resulting film structure. Furthermore, it was pointed out by experiments [65] that C_3 and C_3H are important growth species, and should be included in the model. Therefore, this study was carried out to understand how characteristic hydrocarbon radicals, including C_3 and C_3H, react on specific a-C:H sites. It is clear that a good understanding of the reaction mechanisms of the hydrocarbon radicals at the surface is of paramount importance. The species whose reaction mechanisms have been studied, include C_2, C_3, linear C_3H and cyclic C_3H. In total, 11 surface sites have been investigated. A site is defined as a specific location on this surface: it can be a dangling bond, or one or several atoms bound to the diamond surface, corresponding to sites as they are grown during *e.g.* a deposition process. The different surface sites are shown in Fig. 4.1. Each impact of a specified hydrocarbon radical on a specific site location is repeated 100 times. Although this gives rather poor statistics on rarely occurring reactions, it is sufficient to determine the major reaction mechanisms, which is the goal of this study. Furthermore, as will be shown in the next chapter, the calculation of sticking coefficients on the basis of 100 impact converges to approximately ± 5% of the value obtained after 500 impacts.

Each impacting particle was given a translational energy of 0.13 eV at normal incidence, and an energy of 0.026 eV allowing for vibration and rotation. In Table 4.1, the different hydrocarbon radicals are shown with their major resonance contributors.

In Table 4.2, these species are shown with their gas-phase binding energies, as calculated using the Brenner potential. In total, 4400 impacts have been per-

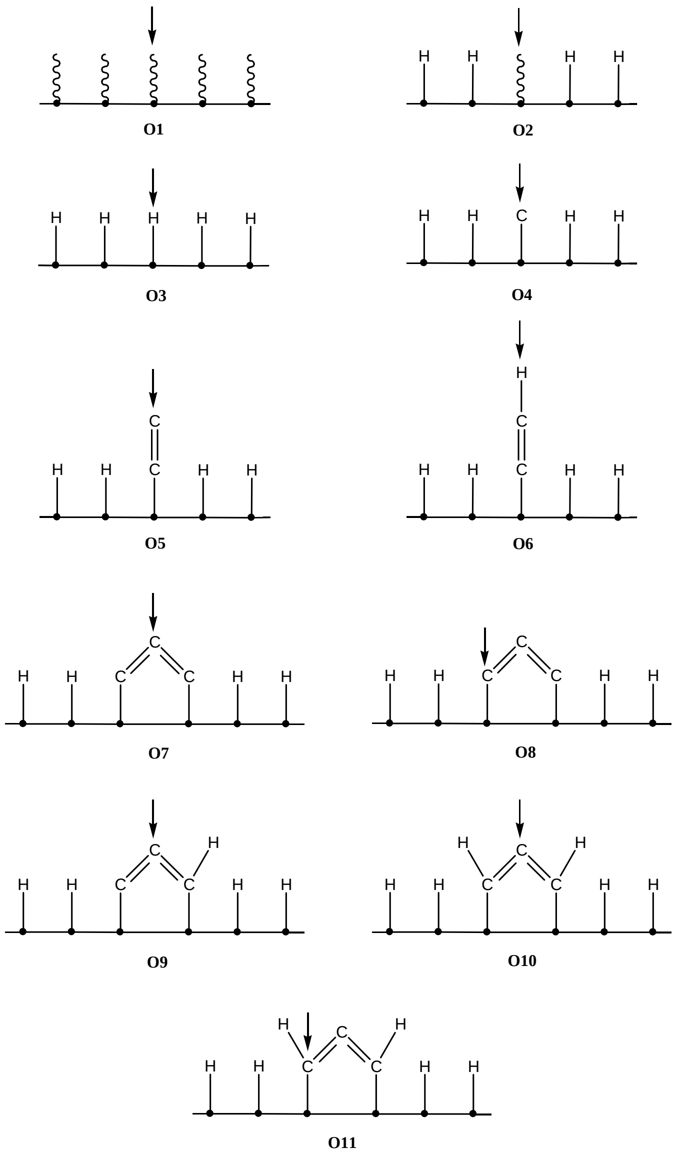

Figure 4.1: Schematic representation of the sites studied in this work. The 11 impact locations are denoted as O_1 to O_{11}. Locations O_7 and O_8, and O_{10} and O_{11} share the same site, but the impact position of the hydrocarbon radical on the site is different. The exact impact location is indicated by the arrows. The dots in the figure indicate surface carbon atoms, and the wavy lines symbolize dangling bonds.

Table 4.1: Main resonance contributors for the species investigated.

Species	Main Resonance Contributors			
C_2	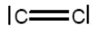	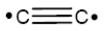		
C_3	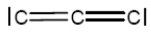	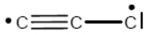	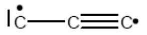	
l-C_3H	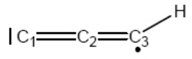	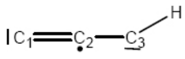	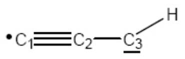	
c-C_3H	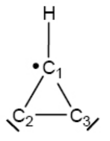	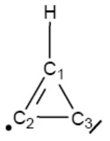	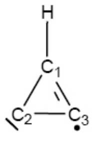	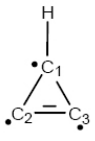

formed and individually analysed. Several trends in the mechanisms have been established. It will be shown that chemical resonance, steric hindrance and structural stability are the main factors affecting the reaction mechanisms. Also, the influence of site-specific factors is addressed. This information is important for a better understanding of the growth of thin a-C:H films from low-kinetic energy hydrocarbons. The results from this chapter have been submitted to Diamond and Related Materials.

4.2 Results and discussion

4.2.1 Sites O_1, O_2 and O_3

Site O_1 is a 3-coordinated carbon atom, i.e., a dangling bond, on the non-passivated diamond surface. Site O_2 is a dangling bond on the passivated diamond surface, created by H-abstraction from this surface. Site O_3 is a H-atom on the passivated, non-reconstructed diamond {111} surface. Note that all species investigated are reflected for 100% on site O_3. The results for sites O_1 and O_2 are summarised in Table 4.3.

Table 4.2: The investigated species and their calculated binding energies. The carbon atom to which the H-atom of the radical is bound, is denoted as C_3 in the *l*-C_3H radical and as C_1 in the *c*-C_3H radical. Note that the binding energy of a single, double and triple C-C bond typically corresponds to -3.60 eV, -6.36 eV and -8.70 eV, respectively.

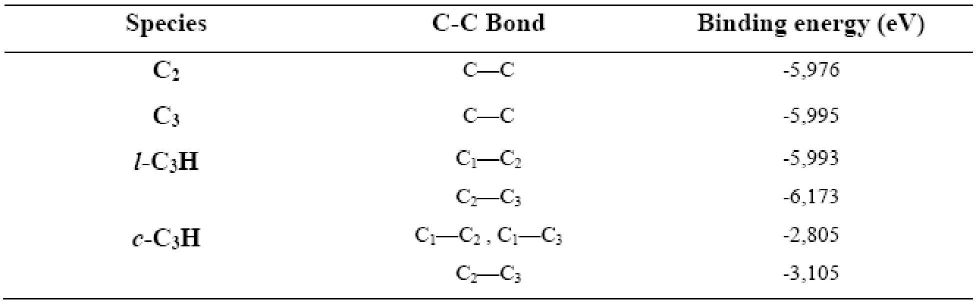

Species	C-C Bond	Binding energy (eV)
C_2	C—C	-5,976
C_3	C—C	-5,995
***l*-C_3H**	C_1—C_2	-5,993
	C_2—C_3	-6,173
***c*-C_3H**	C_1—C_2 , C_1—C_3	-2,805
	C_2—C_3	-3,105

Impact of C_2

The C_2 radicals show a sticking coefficient of 100% on sites O_1 and O_2. This is caused by the fact that C_2 is small (no steric hindrance), and both the carbon atoms of the C_2 radical, as well as the surface carbon atom, have a free electron to participate in the binding. The binding energy between the surface carbon (from here on denoted as "C_s") and the binding radical atom is calculated to be -3.57 eV, both for O_1 and O_2. Note that the average single C-C bond strength is about -3.60 eV, a double bond about -6.36 eV and a triple bond about -8.70 eV.

The intramolecular C-C bond of the radical becomes stronger upon sticking by more than 28% on both sites, to a value of -7.67 eV. Hence, there is a shift from the sp^2 resonance contributor (having a double bond) in the gas phase to the sp resonance contributor (having a triple bond) after sticking to the surface (see Fig. 4.2). An example of the evolution of the binding energy as a function of time is shown in Fig. 4.3 for the O_1 site.

Table 4.3: Calculated sticking and reflection coefficients, and sticking structures on sites O_1 and O_2.

O1 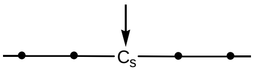				**O2** 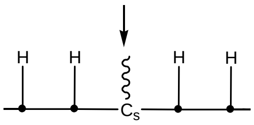			
Radical	**Reflec-tion**	***Sticking*-structures**	**sticking**	**Radical**	**Reflec-tion**	***Sticking*-structures**	**sticking**
C_2 C—C	**O1 :** 0.0 **O2 :** 0.0	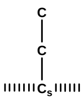	**O1 :** 1.0 **O2 :** 1.0	*l*-**C_3H** *continued*		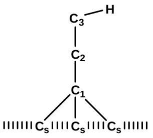	**O1 :** 0.02 **O2 :** 0.0
C_3 $C_2-C_1-C_3$	**O1 :** 0.01 **O2 :** 0.23	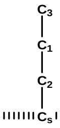	**O1 :** 0.61 **O2 :** 0.77			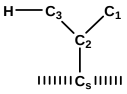	**O1 :** 0.23 **O2 :** 0.03
		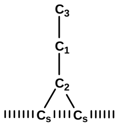	**O1 :** 0.05 **O2 :** 0.0			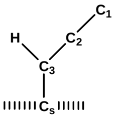	**O1 :** 0.03 **O2 :** 0.0
		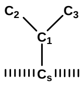	**O1 :** 0.12 **O2 :** 0.0			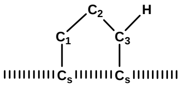	**O1 :** 0.28 **O2 :** 0.0
		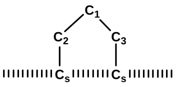	**O1 :** 0.17 **O2 :** 0.0			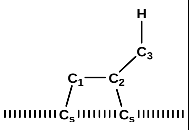	**O1 :** 0.06 **O2 :** 0.0
		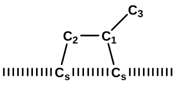	**O1 :** 0.04 **O2 :** 0.0			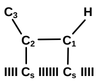	**O1 :** 0.01 **O2 :** 0.0
l-**C_3H** 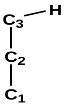	**O1 :** 0.03 **O2 :** 0.49	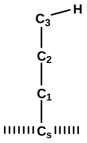	**O1 :** 0.32 **O2 :** 0.48			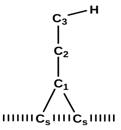	**O1 :** 0.02 **O2 :** 0.0

Table 4.3 continued

c-C_3H 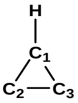	**O1 :** 0.0 **O2 :** 0.18	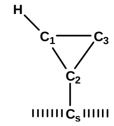	**O1 :** 0.22 **O2 :** 0.23	*c*-C_3H *continued*		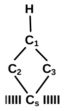	**O1 :** 0.04 **O2 :** 0.0
		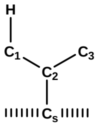	**O1 :** 0.24 **O2 :** 0.46			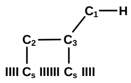	**O1 :** 0.03 **O2 :** 0.0
		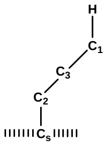	**O1 :** 0.19 **O2 :** 0.05			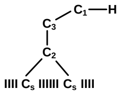	**O1 :** 0.03 **O2 :** 0.0
		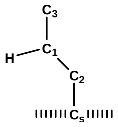	**O1 :** 0.09 **O2 :** 0.04			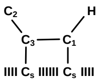	**O1 :** 0.03 **O2 :** 0.0
		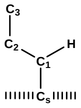	**O1 :** 0.04 **O2 :** 0.04			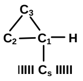	**O1 :** 0.02 **O2 :** 0.0
		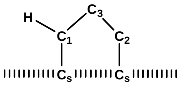	**O1 :** 0.07 **O2 :** 0.0				

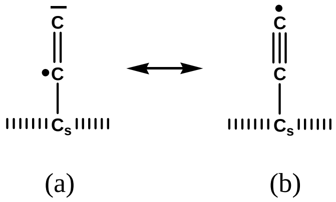

Figure 4.2: Resonance contributors for the C_2 radical after sticking to the surface. The sp^2 resonance contributor (a) shifts towards the sp contributor (b) after sticking.

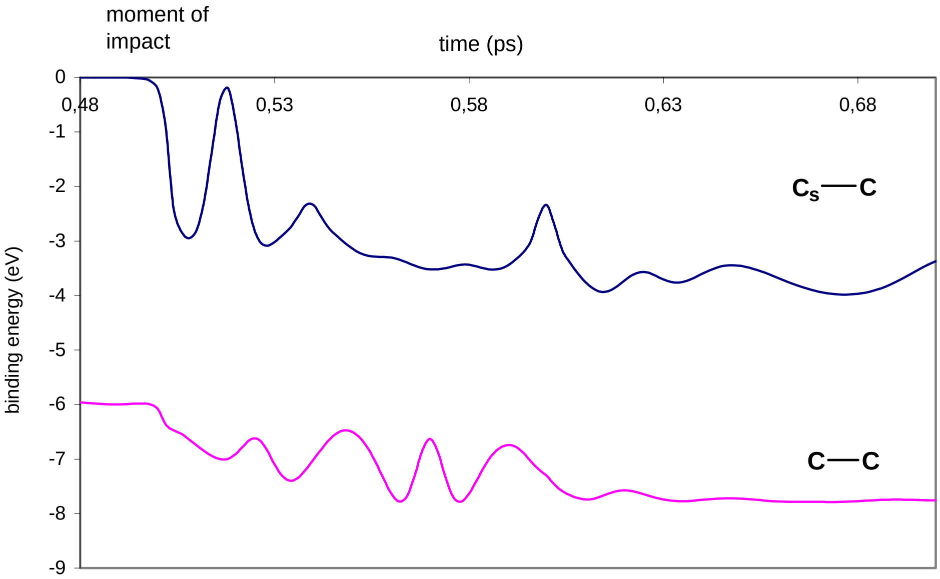

Figure 4.3: Evolution of the binding energy between a surface atom and an impinging C_2 radical (C_S-C), and the change from a double C-C bond in C_2 before the impact (∼ 6 eV) to a triple C-C bond after the impact (∼ 7.8 eV).

All species are reflected for 100% on site O_3 as mentioned above. However, in contrast to the other species, the C_2 radical causes the abstraction of the H-atoms in 56% of its impacts, creating a dangling bond. Indeed, while the other species feel no "advantage" in abstracting the H from the surface, the double bond in the C_2 radical becomes a triple bond in this process, in order to accommodate the extra electron, which explains why C_2 is so effective in H-abstraction. This result also suggests that C_2 radicals can make an a-C:H surface much more reactive, by abstraction of H from a H-passivated surface.

Impact of C_3

In contrast to the C_2 radical, the C_3 radical can bind to the surface in various ways on the O_1 site. Only 1% of the impacts on this site resulted in a reflection event. In 73% of the impacts, the C_3 radical binds to the surface with the formation of a single bond, and in the majority of these cases, this occurs with one of the terminating C_3 carbon atoms (61% vs. 12% with the middle carbon atom).

In the remaining 26% of the impacts, the radical binds to the surface with the formation of two bonds, either involving only the terminating carbon atoms (22%), or both with the middle carbon and one of the terminating carbon atoms (4%). Note that in 21% of the impacts, sticking occurs with the formation of a “bridge” structure.

On the O_2 site, however, 23% of the impacts leads to reflection, and the only occuring sticking mechanism (77%) is the binding of one of the outer carbon atoms with the surface. In this mechanism, the bond between the surface binding C_3 atom and the middle C_3 atom becomes slightly stronger (about +1.6%), while the bond between the other outer C_3 carbon atom and the middle C_3 atom becomes slightly weaker (about -1.0%), both on site O_1 and O_2. This result is a trend observed throughout all simulations presented in this work.

The reason for the much higher reflection coefficient of C_3 on the O_2 site is steric hindrance: the presence of the H-atoms on the O_2 site, allows the C_3 radical to stick on this site only vertically, and only with the formation of a bond between the surface atom with the dangling bond, as opposed to the several possibilities on the O_1 site.

Impact of l-C_3H

The impact of l-C_3H on O_1 and O_2 is comparable to the behaviour of C_3. Similar to C_3, l-C_3H shows a very low reflection coefficient of 3% on site O_1. In 32% of its impacts on O_1, the l-C_3H radical binds to the surface with its outer (non-hydrogen carrying) carbon atom, forming a single bond. This is about half compared to the same sticking event of C_3 on site O_1. Also, a larger fraction of the sticking events occurs through the middle carbon atom in l-C_3H as compared to C_3 (23% of its impacts compared to 12% for C_3). In 28% of the events, a bridge structure is formed between the surface and the two outer carbon atoms of the l-C_3H radical.

The formation of the bridge structures can be explained by the resonance contributors (Fig. 4.4): while in the case of C_3 the C-C bond between the middle carbon atom and the surface binding atom becomes sp-hybridised (triple bond, linear structure), this bond essentially remains a double bond in the case of l-C_3H (sp^2 hybridised, 120° angle). Hence, the other outer carbon atom remains physically close to the substrate atoms (carrying dangling bonds), and has a free electron left. This then promotes the formation of bridge structures, with almost equal occurrence as the single bond mechanism (i.e., 28% vs. 32%). Note that in Fig. 4.4, all three resonance contributors are shown. The main contributor, however, is the structure in which both the outer carbon atoms are sp^2 hybridized.

On the O_2 site, the reflection coefficient of l-C_3H is calculated to be 49%. Again, this is attributed to the same steric hindrance causing the reflection of C_3 on this site. Since the determining factor in this hindrance is the size of the impinging radical, the reflection should be larger than for C_3, as is indeed calculated. When the l-C_3H radicals are not reflected, they stick to the surface mostly with the outer, non-H-carrying C-atom, as is clear from Table 4.3.

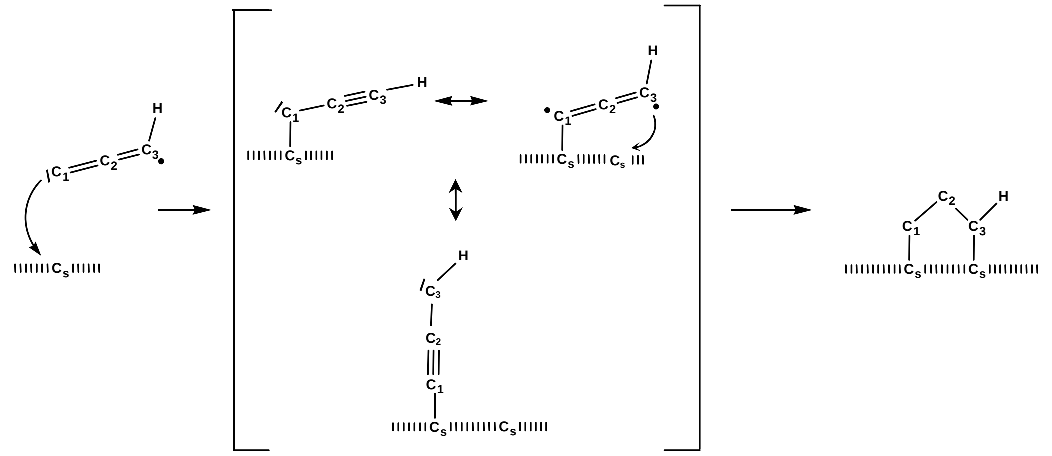

Figure 4.4: Bridge formation upon impact and sticking of a *l*-C_3H radical. The main resonance contributor (in the brackets) is on the top-right.

Impact of *c*-C_3H

The *c*-C_3H radical is much more reactive than the linear C_3H radical. It has a sticking coefficient of 1.0 on the O_1 site, and of 0.82 on the O_2 site. There are two factors responsible for this behaviour. First, it should be noted that the cyclic isomer is structurally unstable. In *e.g.* cyclopropane (cyclic C_3H_6), the C-C bonds are about 32% weaker than in the linear propane molecule, due to a severe ring strain of 117 kJ/mol. In *c*-C_3H, the effect is even more pronounced: the C-C bonds in *c*-C_3H are about 50% weaker than in *l*-C_3H. Hence, the release of this ring strain is a driving force for the radical to break up, enhancing drastically its reactivity. The second reason is the fact that in the *c*-C_3H radical, all three C-atoms bear electrons not participating in a bond, while in *l*-C_3H, the middle C-atom is fully bound. Hence, all three C-atoms in the *c*-C_3H radical can bind to the surface, while the middle C-atom in *l*-C_3H experiences repulsive forces from the surface upon impact [161]. Moreover, due to the fact that the *c*-C_3H radical breaks up easily, more binding configurations result. This break-up occurs in 76% of the sticking events on site O_1, and in 72% on site O_2 (or 59% of the impacts).

The breaking up can occur in several distinct ways. These mechanisms appear on all sites. Of course, the main effect of a break-up event, is the transformation of the cyclic structure into a linear structure. The remaining bonds are strenghtened, depending on which bond is broken and which atom sticks to the surface. As an example, the break-up of a *c*-C_3H radical resulting in a 3-coordinated surface binding atom is shown in Fig. 4.5. It is clear from Table 4.3 that this mechanism, illustrated in Fig. 4.5, is the most important sticking event of *c*-C_3H on the O_1 site and especially on the O_2 site.

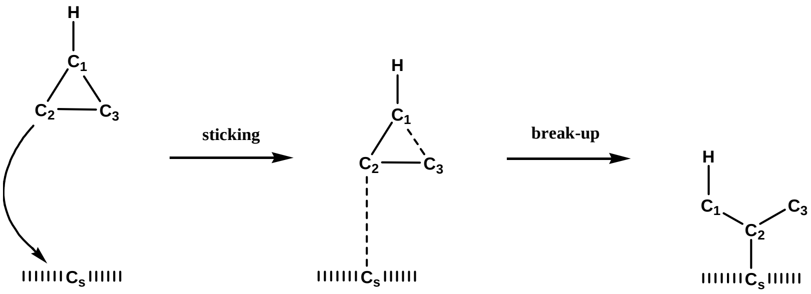

Figure 4.5: Schematic representation of the sticking and break-up mechanism of the *c*-C_3H radical, leaving the surface binding atom 3-coordinated.

4.2.2 Sites O_4 and O_5

In most cases, the sticking behaviour of the various radicals is very similar on both O_4 and O_5 sites. In general, the sticking coefficient on site O_5 is slightly higher than on O_4, due to steric hindrance on site O_4, caused by the H-atoms surrounding the site. The results are summarised in Table 4.4.

Impact of C_2

As already indicated above, the C_2 radical is very reactive. On the O_4 site it shows a sticking coefficient of 0.95, and a sticking coefficient of 1.0 on site O_5. In most

Table 4.4: Calculated sticking and reflection coefficients, and sticking structures on sites O_4 and O_5.

O4 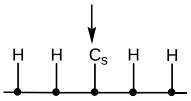

O5 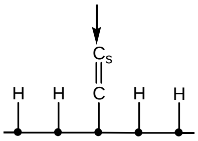

Radical	Reflec-tion	*Sticking*-structures	Sticking	Radical	Reflec-tion	*Sticking*-structures	Sticking
C_2 C—C	**O4 :** 0.05 **O5 :** 0.0	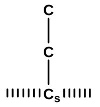	**O4 :** 0.91 **O5 :** 1.0	*c*-C_3H *continued*		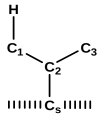	**O4 :** 0.06 **O5 :** 0.12
		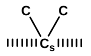	**O4 :** 0.04 **O5 :** 0.0			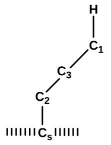	**O4 :** 0.28 **O5 :** 0.32
C_3 C_2—C_1–C_3	**O4 :** 0.23 **O5 :** 0.09	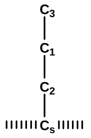	**O4 :** 0.77 **O5 :** 0.91			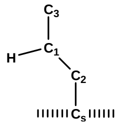	**O4 :** 0.13 **O5 :** 0.33
l-C_3H 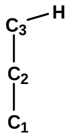	**O4 :** 0.35 **O5 :** 0.16	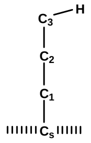	**O4 :** 0.55 **O5 :** 0.46			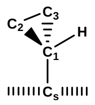	**O4 :** 0.0 **O5 :** 0.17
		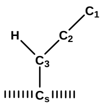	**O4 :** 0.10 **O5 :** 0.38			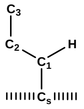	**O4 :** 0.01 **O5 :** 0.06
c-C_3H 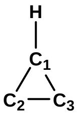	**O4 :** 0.04 **O5 :** 0.0	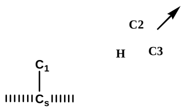	**O4 :** 0.37 **O5 :** 0.0			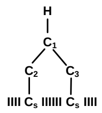	**O4 :** 0.02 **O5 :** 0.0
		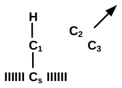	**O4 :** 0.08 **O5 :** 0.0			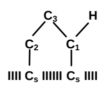	**O4 :** 0.01 **O5 :** 0.0

cases, the C_2 radical sticks on site O_4 with one of its atoms, but in a few cases, the C-C bond breaks, and both of the atoms bind to the same surface atom. This mechanism does not occur on the O_5 site, as appears from Table 4.4.

Impact of C_3

The sticking coefficient of C_3 is calculated to be very high on the O_5 site (0.91), and it is considerably less on the O_4 site (0.77). This is entirely due to steric hindrance by the surrounding H-atoms on the O_4 site. This radical invariably sticks with one of its outer C-atoms and thereby forms one double bond to the surface. The middle C-atom does not bind to the surface, as mentioned above, due to repulsive forces between this atom and the surface. Again, the bond between the middle C-atom and the surface binding atom becomes slightly stronger upon sticking (+1.4%), while the other C-C bond in the radical becomes slightly weaker (-1.3%).

Impact of *l*-C_3H

The sticking coefficient of *l*-C_3H is calculated to be 0.65 on the O_4 site, and 0.84 on the O_5 site. The lower value on the O_4 site compared to the O_5 site is, once again, due to steric hindrance. Moreover, the values are slightly lower than for C_3, due to the slightly larger radical, yielding a bit more steric hindrance.

In this case, two sticking mechanisms are possible: the radical binds to the surface either with the outer C-atom, not carrying the H-atom (55% on O_4, 46% on O_5), or it sticks to the surface with the H-carrying C-atom (10% on O_4, 38% on O_5). The first mechanism occurs more often than the second one, since the H-atom is shielding the C-atom from the surface. This is especially true on the O_4 site. On the O_5 site, this effect is diminished due to the fact that the surface atom on the O_5 site is not partially shielded by other surface atoms, as is the case on the O_4

site. Again, the middle C-atom cannot bind due to repulsive forces.

Impact of *c*-C_3H

It is seen in Table 4.4 that the *c*-C_3H radicals are again more reactive at the surface than the *l*-C_3H radicals, as the calculated reflection coefficients on sites O_4 and O_5 are much lower. On site O_4, only 4% of the *c*-C_3H radicals are reflected. Simple reflection of the *c*-C_3H radical occurred only in 1% on site O_4. In 3% of the cases, it also reflects, but at the same time it abstracts the surface C atom from the surface, thereby creating a C_4H species, which then moves away from the surface. In 37% of the impacts, only one of the C-atoms of the radical sticks to the surface, while the remaining H-atom and the two other C-atoms do not stick and are reflected back into the plasma. In another 8% of the impacts, a CH fragment sticks, while the other two carbon atoms reflect. In all other cases (51% of the impacts), the whole molecule sticks to the surface. In all cases investigated, one or several bonds of the *c*-C_3H radical break upon sticking on site O_4. Hence, the radical never stays intact upon sticking to the surface.

On site O_5, reflection does not occur at all. While on the O_4 site, partial sticking occurs regulary (45% of the impacts), this appears not to happen on the O_5 site. Also the fraction of impact events causing the break up of the radical decreases to 83%, thereby leaving an intact *c*-C_3H radical stick to the surface in 17% of the cases. In this case, *c*-C_3H sticks to the site with the carbon atom carrying the H-atom. This creates a 4-coordinated C-atom, while all the other mechanisms create either a 2-coordinated C-atom (65%), or a 3-coordinated C-atom (18%).

4.2.3 Site O_6

The O_6 site consists of a linear C_2H fragment at the surface. On this surface, only the C_2 radical seems to be reactive. The results are summarised in Table 4.5. C_2

reflects in 66% of its impacts. In 65% of these reflection events, the C_2 abstracts the H from the surface, and desorbs back into the plasma as a C_2H species. In the remaining 35% of the reflection events, it simply reflects. In only 7% of its impacts, it sticks directly on the upper C-atom of the site. In 27% of its impacts, however, the C_2 radical is "inserted" between the upper C-atom of the site, and the H-atom attached to it. This is a 2-step process: first, one of the C_2 C-atoms abstracts the H from the site. Then, the other C-atom of the C_2 radical (which has by then become a C_2H radical), binds to the C-atom of the site that was previously carrying the H-atom. In this way, the C_2 radical has inserted itself in the site. All the other radicals appear to give 100% simple reflection, due to the H-passivation (cfr. site O_3).

Table 4.5: Calculated sticking and reflection coefficients, and sticking structures on site O_6.

O6

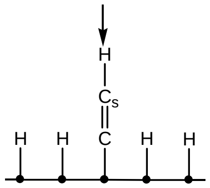

Radical	Reflection	*Sticking*-structures	Sticking
C_2 C—C	0.66	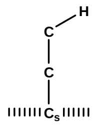	0.27
		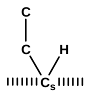	0.07
C_3 , l-C_3H and c-C_3H	100% reflection		

4.2.4 Sites O_7 and O_8

The O_7 and O_8 sites are identical. However, the position at which the radicals impinge on the site is different: on the O_7 site, the middle C-atom is bombarded, while on the O_8 site, the radical attacks one of the outer C-atoms. The results are summarized in Table 4.6.

Impact of C_2

Again, the C_2 radical is very reactive: it has a sticking coefficient of 1.0 on site O_7 and 0.98 on site O_8. The sticking energy is about -5.1 eV, which is lower than on the O_4 and O_5 sites, due to the fact that here, the C_s atom becomes 3-coordinated, so that a true double bond cannot be formed. Indeed, all three bonds to the C_s atom become more or less equal in strength. When impacting on site O_8, a bridge structure can be formed, although this was found to occur in only 3% of the impacts.

Impact of C_3 and l-C_3H

The C_3 radical is not very reactive on these sites, especially on the O_7 site, where 95% of its impacts result in reflection, yielding a sticking coefficient of 0.05. On the O_8 site, the sticking coefficient increases to 0.22. The only mechanism observed, consists of the C_3 radical sticking with one of its outer C-atoms to one of the site atoms.

The same is true for the l-C_3H radical. It has a sticking coefficient of 0.12 and 0.21 on sites O_7 and O_8, respectively. Again, it only sticks with one C-atom to one of the site atoms. In this case, the sticking atom is invariably the outer C-atom that is not connected to the H-atom.

Table 4.6: Calculated sticking and reflection coefficients, and sticking structures on sites O_7 and O_8.

O7	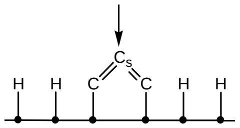			**O8**	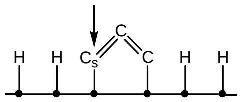		
Radical	**Reflec-tion**	***Sticking-*** **structures**	**Sticking**	**Radical**	**Reflec-tion**	***Sticking-*** **structures**	**Sticking**
C_2 C—C	**O7 :** 0.0 **O8 :** 0.02	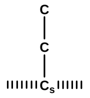	**O7 :** 1.0 **O8 :** 0.95	*c*-C_3H *continued*		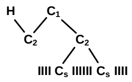	**O7 :** 0.08 **O8 :** 0.08
		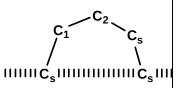	**O7 :** 0.0 **O8 :** 0.03			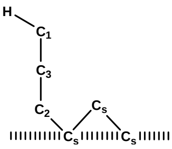	**O7 :** 0.0 **O8 :** 0.10
C_3 C_2—C_1–C_3	**O7 :** 0.95 **O8 :** 0.78	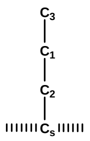	**O7 :** 0.05 **O8 :** 0.22			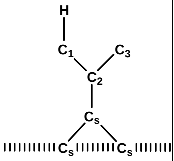	**O7 :** 0.07 **O8 :** 0.04
l-C_3H 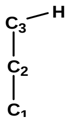	**O7 :** 0.88 **O8 :** 0.79	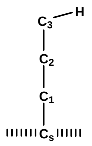	**O7 :** 0.12 **O8 :** 0.21			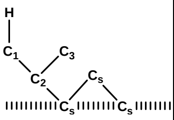	**O7 :** 0.0 **O8 :** 0.02
c-C_3H 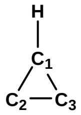	**O7 :** 0.71 **O8 :** 0.41	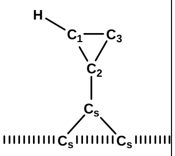	**O7 :** 0.06 **O8 :** 0.04			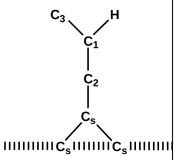	**O7 :** 0.08 **O8 :** 0.02
		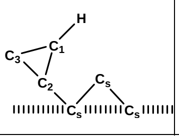	**O7 :** 0.0 **O8 :** 0.29				

Impact of *c*-C_3H

Again, the *c*-C_3H radical shows the most complex reaction behaviour. Its sticking coefficient is calculated to be 0.29 and 0.59 on site O_7 and O_8, respectively. While the position of impact on the O_8 site is one of the outer C-atoms of the site, the *c*-C_3H radical can also stick on the middle C-atom in this case. The opposite seems not to occur. The higher sticking coefficient on site O_8 than on site O_7, can be explained by considering the connectivity of the surface atoms. On site O_7, the surface atom under attack is the middle carbon atom. Since this atom is fully bound, the incoming radical will experience repulsive forces from this atom, effectively decreasing the reactivity on this site. On site O_8, however, the surface atom under attack is one of the atoms at the site, having a dangling bond, effectively enhancing the reactivity on this site.

On the O_8 site, two reaction mechanisms seem to be preferred: in 29% of its impacts, the radical sticks to the outer C-atom of the site, with one of the C-atoms not connected to the H-atom, and without breaking up. In 10% of its impacts, the same mechanism occurs, but now with breaking of the bond between the sticking C-atom and the C-atom that carries the H-atom. Further, it should be noted that in 26% of the impacts on O_8, the radical breaks up, and on site O_7 this happens in 23% of the impacts.

4.2.5 Site O_9

The O_9 site is identical to the O_7 site, except for the H-atom connected to one of the outer C-atoms of the site. The mechanisms occurring on this site, are identical to the ones on the O_7 and O_8 sites. Although the radicals now only impinge on the middle C-atom, some of them also bind to the C-atom at the side (i.e., the one which is not bound to the H-atom). The H-atom serves two functions in this respect: first, it shields the C-atom to which it is connected. Second, it also pushes impinging radicals to the other side of the site, due to repulsion between the H-atom and the incoming radical. The results are summarized in Table 4.7.

Table 4.7: Calculated sticking and reflection coefficients, and sticking structures on site O_9.

O9

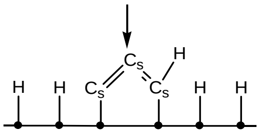

Radical	**Reflec -tion**	***Sticking*- structures**	**Sticking**	**Radical**	**Reflec -tion**	***Sticking*- structures**	**Sticking**
C_2 C—C	0.0	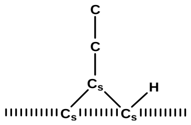	0.84	*c*-C_3H 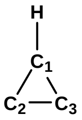	0.18	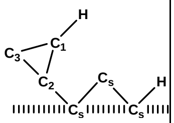	0.22
		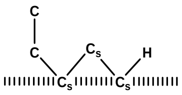	0.14			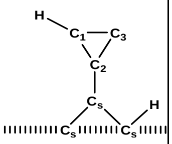	0.16
		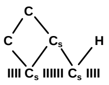	0.02			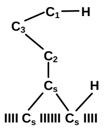	0.15
C_3 C_2—C_1–C_3	0.74	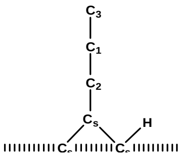	0.23			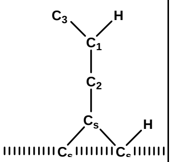	0.14
		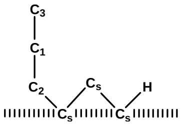	0.03			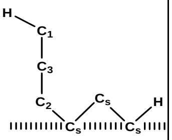	0.05
l-C_3H 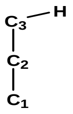	0.78	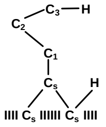	0.12			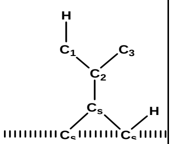	0.07
		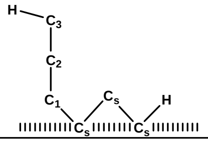	0.10			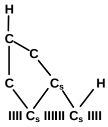	0.03

Impact of C_2

The C_2 radical appears to have a sticking coefficient of 1 on this site, and it sticks either on the middle (spotted) C-atom (84% of the impacts), or on the side C-atom which does not carry the H-atom (14%). In the remaining 2 impacts, a bridge structure was formed, in which the radicals stick with both atoms to both the available site atoms (i.e., not the H-carrying C-atom).

Impact of C_3 and *l*-C_3H

Entirely corresponding to the trend seen on the previous sites, the C_3 and *l*-C_3H radicals show a much lower sticking coefficient: 0.26 and 0.22, respectively. Again, they bind to the surface with the outer C-atom. The C_3 radical binds mostly on the middle C-atom (23% of its impacts), while the *l*-C_3H binds in about equal amounts on both the middle and the outer, non H-carrying C-atom of the site. This is caused by the H-atom of the radical: it interacts with the site atoms, resulting in a "push-effect". The radical is effectively pushed towards the side atom of the site.

The H-atom on the site itself also effectuates a push-effect. However, although the C_3 radical is pushed towards the side, it can still bind to the middle carbon atom more easily, due to the size of the molecule (it has 2 available C-atoms, at both sides), and due to the fact that the C-atom in the middle of the site is sterically more easily available.

Impact of *c*-C_3H

The difference in reactivity between the cyclic and the linear isomer of the C_3H radical is again clearly visible. The *c*-C_3H radical is reflected in only 18% of its impacts, to be compared with 78% of the *l*-C_3H impacts on this site. The same structures arise as on the previous two sites. In 38% of the impacts, the radical stays intact, and then it sticks a bit more easily at the side of the site (22% vs. 16% on the middle C-atom). If a bond is broken during the sticking event, then the radical will stick more easily on the middle atom of the site. In only 5% of all impacts, the radical will break up and stick on the available C-atom at the side.

4.2.6 Sites O_{10} and O_{11}

The last two sites we have simulated are a variation on the three previous sites. On both the outer carbon atoms of the site, a H is attached. Again, the radicals can impinge on both the middle carbon atom, and on one of the side carbon atoms. The results are summarized in Table 4.8.

Impact of C_2

As is already clear from the above, the C_2 radical is very reactive, and its reaction behaviour leads to structures not found for the other radicals, as will be shown below. The other radicals only stick on the middle carbon atom of the site (if they stick), but the C_2 radical can also stick on the outer C-atoms.

On the O_{10} site, the impact position of the radical is the middle C-atom of the site. The sticking coefficient of the C_2 radical is then calculated as 1.0. In all cases, the mechanism is straightforward: the C_2 radical simply sticks with one of its atoms on the middle C-atom of the site, with the formation of a medium strong bond of (on average) -4.88 eV. Recall that the average single C-C bond strength is about -3.60 eV, a double bond about -6.36 eV, and a triple bond about -8.70 eV. The C-C bond in the C_2 radical is weakened by about 3% compared to the gas phase.

On the O_{11} site, however, the impact position is one of the side atoms. The sticking coefficient remains very high (0.95), and most sticking events yield the

Table 4.8: Calculated sticking and reflection coefficients, and sticking structures on sites O_{10} and O_{11}.

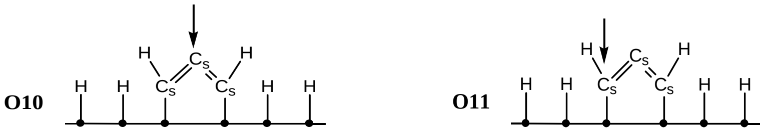

Radical	Reflection	*Sticking*-structures	Sticking	Radical	Reflection	*Sticking*-structures	Sticking
C_2 C—C	**O10 :** 0.0 **O11 :** 0.05	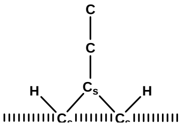	**O10 :** 1.0 **O11 :** 0.72	*c*-**C_3H** 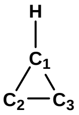	**O10 :** 0.03 **O11 :** 0.17	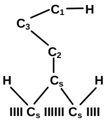	**O10 :** 0.38 **O11 :** 0.33
		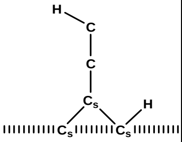	**O10 :** 0.0 **O11 :** 0.16			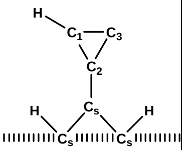	**O10 :** 0.21 **O11 :** 0.29
		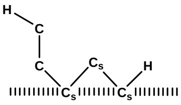	**O10 :** 0.0 **O11 :** 0.07			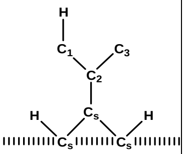	**O10 :** 0.21 **O11 :** 0.03
C_3 C_2—C_1–C_3	**O10 :** 0.48 **O11 :** 0.42	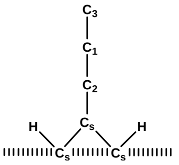	**O10 :** 0.52 **O11 :** 0.58			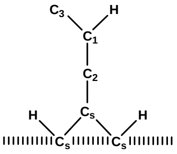	**O10 :** 0.14 **O11 :** 0.12
l-**C_3H** 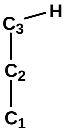	**O10 :** 0.69 **O11 :** 0.65	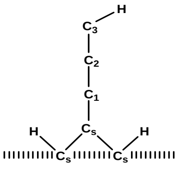	**O10 :** 0.31 **O11 :** 0.29			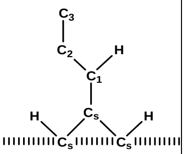	**O10 :** 0.03 **O11 :** 0.06
		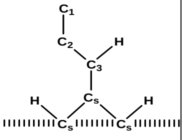	**O10 :** 0.0 **O11 :** 0.06				

same structure as sticking on O_{10}: the C_2 radical being bound to the central C-atom of the site (72% of its impacts). In 16% of its impacts, the radical also binds to the middle carbon atom, but the H-atom from the side has shifted from the side-atom to the upper C_2-atom. In the remaining 7% of its impacts, the C_2 radical sticks on the side atom. The H-atom is replaced by the C_2-radical, and becomes bound to the upper atom of the C_2 fragment, as was also the case on site O_6. In the events where the H-atom becomes bound to the C_2-radical, this H-shift stabilizes the C-C bond, and strengthens the bond between the site-atom and the radical, as compared to sticking on the O_{10} site. This can be explained by the fact that removal of the H-atom induces several resonance structures, donating electrons to the C_s-C_2 bond and the C_2 fragment.

Impact of C_3

The C_3 radical has a calculated sticking coefficient of 0.52 and 0.58 on site O_{10} and O_{11}, respectively. Only one structure it formed: one of the outer C-atoms becomes connected to the middle carbon atom of the site. Again, the C-C bond connecting the surface binding atom of the radical and the middle carbon atom of the radical becomes slightly stronger (about 1.5%), while the other bond of the radical becomes slightly weaker by about 1.2% and 1.7% on both sites, respectively. Remarkable however is the fact that the presence of H on the sites seems to enhance the sticking of this radical: the sticking coefficient of C_3 increases from 0.05 on site O_7, to 0.26 on site O_9, and to 0.52 on site O_{10} (same impact position).

Impact of *l*-C_3H

The stabilizing effect of the H-atom(s) on the site is also visible for the *l*-C_3H radical, although to a lesser extent. In the series of impacts on sites O_7, O_9 and O_{10}, its calculated sticking coefficient goes up from 0.12 to 0.22 to 0.31. On the

O_{10} site, the l-C_3H radical only sticks through its outer available non-H-carrying carbon atom, binding to the middle carbon atom of the site. On the O_{11} site, the sticking coefficient is calculated to be 0.35. In this case, 83% of its sticking events (or 29% of the impacts) occurs through the same mechanism as on the O_{10} site, whereas in the remaining events, the carbon atom carrying the H-atom of the radical, sticks to the middle carbon atom of the site. In this case, the C-C bond connecting the carbon atom of the radical that binds to the site, and the middle carbon atom of the radical, is weakened significantly by almost 20%.

Impact of c-C_3H

The c-C_3H radical is very reactive on the O_{10} site, showing a sticking coefficient of 0.97. In 38% of its impacts, the bond between the sticking atom and the H-carrying C-atom of the radical is broken. The surface sticking atom is one of the “available” radical carbon atoms. In this case, the surface sticking atom becomes 2-coordinated. In 21% of the impacts, the radical simply sticks, without the breaking of a bond. Now, the surface sticking atom becomes 3-coordinated. Two other mechanisms also leave the surface sticking atom 3-coordinated: in 21% of the sticking events, the bond between het H-carrying atom, and the carbon atom that is not bound to the surface breaks. The third carbon atom then binds to the surface. In a few cases (3% of the impacts), the H-carrying atom itself binds to the surface. The bond connecting this atom and one of the two other carbon atoms then breaks. Finally, one last mechanism is observed, in which the bond between the two carbon atoms that do not carry the H-atom breaks. The radical then sticks with one of these atoms (14% of the impacts). On the O_{11} site, the same reactions are observed. However, the sticking coefficient is now lower, with a calculated value of 0.83.

4.3 Conclusion

Molecular dynamics studies using the Brenner potential have been carried out to investigate the sticking behaviour of several radicals typically observed in the expanding thermal plasma. Specific sites have been built, to gain insight in the deposition mechanism of thin a-C:H films. The radicals studied here include C_2, C_3, *l*-C_3H and *c*-C_3H. These are experimentally shown to be important growth species in ETP deposition of thin a-C:H films [63, 65].

It is observed that C_2 is the most reactive of these species, and capable of H-abstraction from the surface. The C_3 radical shows a moderate sticking coefficient of on average about 0.5. The middle carbon atom never binds to the surface due to repulsive forces induced by the fully bound central atom. The two other carbon atoms, however, are available and reactive, and hence, bridge structures are easily formed.

Comparing the two C_3H isomers, it is clear that the cyclic variant is much more reactive, having a sticking coefficient of on average 0.73. The linear radical, on the other hand, is less reactive, with a sticking coefficient of about 0.42. This can be explained by the fact that (1) the cyclic radical easily breaks up, enhancing its reactivity; (2) the central carbon atom in the linear isomer is fully bound, inducing repulsive forces with the substrate (identical to C_3), leaving only the outer C-atoms available and reactive, whereas the cyclic variant does not have such a fully bound C-atom; and (3) the H-atom in the linear isomer shields one of the two outer carbons, leaving only one of the atoms available and reactive. Hence, the least reactive species is the linear C_3H radical.

These results are important for the study of the expanding thermal plasma, in which these species have been observed [7]. They allow us to gain insight into how the a-C:H films, grown with this source, are actually deposited. Second, these results are also relevant for film growth in general. For instance, it is clearly shown that sticking coefficients of hydrocarbons on a-C:H surfaces are site dependent. It is likely that this is also true on other covalently bound materials. Finally, these results are also important as input for plasma simulations, where knowledge of sticking coefficients is of great importance.

Chapter 5

Influence of internal energy and impact angle on the reaction mechanisms for a-C:H growth precursors

Abstract

In this chapter, we investigate the influence of the internal energy and the impact angle on the sticking coefficients of several hydrocarbon radicals on a hydrogenated amorphous carbon surface. The selected radical species and their kinetic energy were determined experimentally. However, no information is available regarding their internal energy, nor on their impact angles. It is shown that the internal energy has a considerable influence on the sticking coefficients, which is dependent on the kind of species. The impact angle, however, is shown to be of minor importance.

5.1 Introduction

Essentially, a deposited thin film exhibits certain properties due to the actual growth mechanism that produces the film. Therefore, a parameter study investigating the numerous factors governing the deposition mechanism should enable us to optimize the growth of the films in terms of their properties. In the present work, the influence of internal energy and impact angle of the bombarding species on their reaction probability (more specifically, their sticking coefficients) is investigated, because these parameters are often not exactly known from experiment. Sticking coefficients are also important input parameters in e.g. plasma simulations [162].

The selected radical species and their kinetic energy were determined experimentally [4, 62–65]. However, no information is available regarding their internal energy, nor on their impact angles.

The substrate on which the radical impacts were performed was a previously simulated thin a-C:H film, containing 610 atoms. The hydrogen content in the substrate is 9.5%. This substrate was created by sequential radical impacts on a clean diamond {111} surface until a thickness of 10 nm was reached. This structure was then 'relaxed', and the diamond layer was removed.

The selected species are CH, C_2, C_2H, linear C_3 (l-C_3), linear C_3H (l-C_3H), cyclic C_3 (c-C_3) and cyclic C_3H (c-C_3H). The kinetic energy of the species was set to 0.13 eV, corresponding to the experimentally measured gas temperature of about 1500K. No experimental information was available regarding the internal energy of the radicals. Therefore, we have chosen values over two orders of magnitude. The internal energy for each of the species was taken as 0.026 eV; 0.50 eV; 1.0 eV; 2.0 eV; 2.6 eV. The selected polar impact angles were $\theta = 0^o$; 15^o; 30^o; 45^o, while the azimuthal angle was chosen randomly. An integration time of 2 ps was chosen for the simulations using impact angles of 0^o and 15^o, while integration times of

2.2 ps and 2.4 ps were chosen for impact angles of 30° and 45°, respectively, to account for the longer path they travel before reaching the surface. The internal energy of the particles in the simulations using different impact angles was 0.026 eV.

Each calculation of the sticking coefficient for a species with a given impact angle and internal energy involved 500 impacts. As an example, the accumulated calculated sticking coefficients for the C_3H radical at an impact angle of 0° and different internal energies are shown in Fig. 5.1 as a function of the impact number. The plotted sticking coefficient s_i in this figure, at any impact number i, is given by:

$$s_i = \frac{\sum\limits_{j=1}^{i} \delta_j}{i} \tag{5.1}$$

where δ_j is the Kronecker delta. A particle is considered to stick if at least one of its constituent atoms is bound to the surface. It can be seen in the figure that after 500 impacts, the sticking coefficient has converged to its final value. Also shown in figure 1 is the procentual difference between the calculated sticking coefficient at impact i and the so-called final calculated value (i.e., after 500 impacts). The dashed horizontal lines indicate the ± 5% boundaries, relative to the final value. The full horizontal lines indicate the ± 2% boundaries. After about 200 impacts, the accumulated sticking coefficient has converged to within ± 5% of its final value. This value converges to within 2% after about 400 impacts. Similar results (but typically showing somewhat faster convergence) were obtained for the other species.

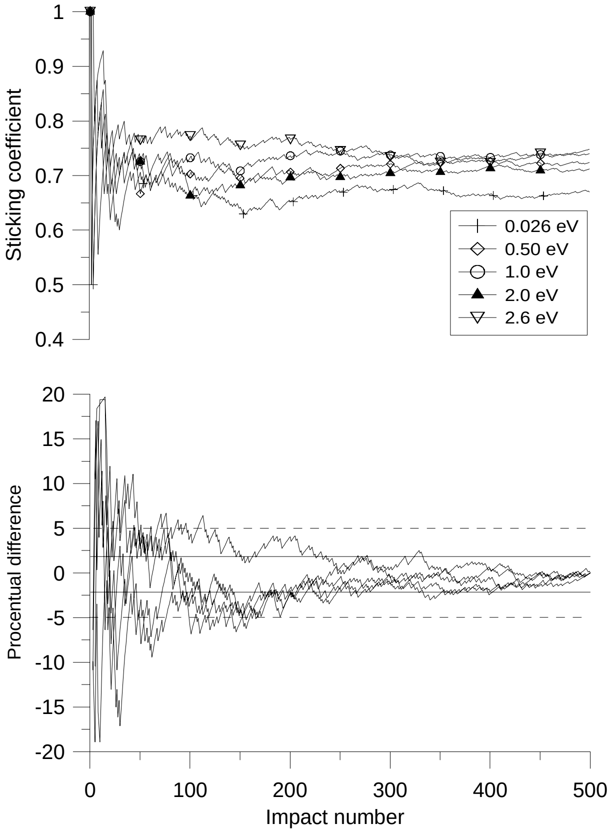

Figure 5.1: Calculated accumulated sticking coefficients for the C_3H radical at an impact angle of 0°, for different internal energies (top). Also shown is the procentual difference between the running accumulated sticking coefficient and the final value after 500 impacts (bottom). The dashed horizontal lines denote the ± 5% boundaries, and the full horizontal lines the ± 2% boundaries. The final sticking coefficients for the different energies are given in Fig. 5.2.

5.2 Results and discussion

5.2.1 Effect of the internal energy

In Fig. 5.2, the calculated sticking coefficients for the different species are shown as a function of their internal energies. It can be seen that CH, C_2H and *c*-C_3H show a decrease in their sticking coeffient for increasing internal energies. The

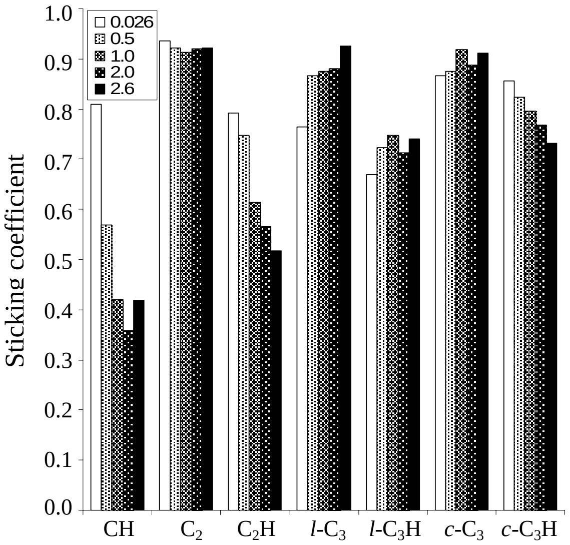

Figure 5.2: Calculated sticking coefficients of the different species as a function of their internal energy (in the legend given in eV), distributed among vibrational and rotational motion.

sticking coefficients of the l-C_3, l-C_3H and c-C_3 species on the other hand show a slight increase as a function their internal energy. Finally, the sticking coefficient of C_2 is nearly independent of its internal energy. In general, all species show a high sticking coefficient, varying between 0.4 and 0.9, due to their strong radical nature.

The species showing the highest sticking coefficient throughout the simulations is C_2, with a sticking coefficient of above 0.9. Indeed, both of the carbon atoms have an unpaired electron, ready to pair with a radical site at the surface (cfr. the previous chapter). Also, both C-atoms are “free”, i.e., unhindered and unshielded by a H-atom. Therefore, the exact rotational orientation of the species relative to the surface is unimportant: at least one of both C-atoms is entirely free to react with the surface atoms, independent of its exact orientation towards the surface upon impact. Also the vibrational part of the internal energy does not alter the sticking coefficient significantly, since only stretch vibrations are possible. This vibration mode does not affect the constituent atoms reaction probabilities.

The relevance of these effects become clear by comparison with C_2H. The sticking coefficient of C_2H is considerably lower than the C_2 sticking coefficient, and it is also much more dependent on the internal energy, varying from nearly 0.8 till about 0.5, for an internal energy between 0.026 eV and 2.6 eV, respectively. Indeed, while in C_2, both C-atoms can react with the surface, the C_2H radical will stick to the surface virtually always with the C-atom that is not carrying the H-atom. The other C-atom is shielded by the H-atom. Hence, in this case the orientation of the radical relative to the surface is limiting its reaction probability. Increasing the internal energy, and hence introducing more "violent" vibrations, results in a decrease in the sticking coefficient. Indeed, since the H-atom is very light, it moves much faster than the C-atoms. Increasing the internal energy allows the H-atom to cover a wider area around the C-atom it is attached to. When the radical now approaches the surface, the repulsive forces between the radical and the surface atoms will become more apparent, due to the wider action radius of the H-atom. In other terms: the H-atom that partially shields the radical from the surface, widens its repulsive interaction range with the surface due to its amplified motion resulting from the increase in internal energy.

The same effect also occurs for CH, which shows a very similar trend in its sticking coefficient behaviour as a function of its internal energy, varying from 0.8 at 0.026 eV, to about 0.35 at 2.0 eV. The slight increase for the highest internal energy chosen in this work, i.e., 2.6 eV, is due to the strong increase in the fraction of impacts in which the radical breaks up upon impact and subsequently reacts with the surface, as shown in Fig. 5.3 (see below).

The l-C_3 radical is similar to C_2 in the sense that it has 2 C-atoms which can freely react with the surface. The middle C-atom, which is fully bound, almost never reacts with the surface [161]. Hence, the reaction probability of C_3 is nearly

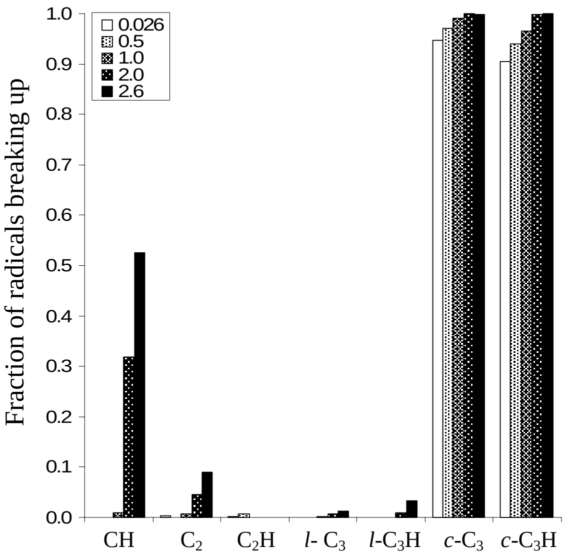

Figure 5.3: Calculated fraction of sticking radicals that break up upon impact for different internal energies (in eV).

independent of its rotational orientation relative to the surface, similar to C_2. In contrast to C_2, however, the sticking coefficient of l-C_3 shows an additional dependence on its internal energy. The higher internal energy increases the number of sticking events with one of the outer C-atoms, due to the lower influence of the middle carbon atom: as the molecule vibrates more, the radical is more non-linear, decreasing the repulsive interactions from the middle carbon atom with the surface. The same is true for the l-C_3H radical, although here this effect is reduced by the effect of the increased H-interaction. Overall, the H-atom is responsible for the lower sticking coefficient of l-C_3H as compared to l-C_3.

The c-C_3 and c-C_3H radicals are species with weak interatomic bonds, due to their structure: indeed, the 3-atom ring configuration introduces a ring stress lowering the interatomic bond strengths. Upon impact, most of these radicals break up, as shown in Fig. 5.3 and also in the previous chapter. Here, the fraction of the radicals is shown that break up upon impact and subsequently stick on the surface. In this process, the radicals are converted into their respective linear counterparts.

The calculated sticking coefficients for these species having high internal energies therefore correspond very closely to the values obtained for the linear species.

At lower internal energies, the calculated sticking coeffients are higher for the cyclic isomers as compared to the linear isomers (cfr. previous chapter). This is caused by the reactivity of the unpaired electrons in the cyclic radicals, and the absence of a fully bound central atom in the cyclic isomers. Therefore, the radicals can easily react with the surface, leading to a high sticking coefficient. As the internal energy increases, more radicals are converted into their linear counterparts (due to the increase in the break-up events), and a fully bound central C-atom is created, altering the sticking coefficient, such that it converges towards the value for the corresponding linear radical.

5.2.2 Effect of the impact angle

We have also investigated the effect of the impact angle in the range between 0^o and 45^o on the sticking coefficients of the different radicals. The results are shown in Fig. 5.4. It appears that the effect is minimal for all species. Furthermore, the reaction mechanisms for the different species remain unaltered, when changing the impact angle. Hence, the effects described above remain valid under these circumstances. Possibly, this is due to the low kinetic energy of the species: indeed, the impact angle hardly changes the interaction time between the radical and the surface. Hence, it appears that the assumption of normal incidence in our MD simulations can give a realistic picture, even if the exact impact angle is not known.

5.3 Conclusion

Molecular dynamics simulations have been performed to investigate the effect of the internal energy of a set of hydrocarbon radicals on their sticking coefficients

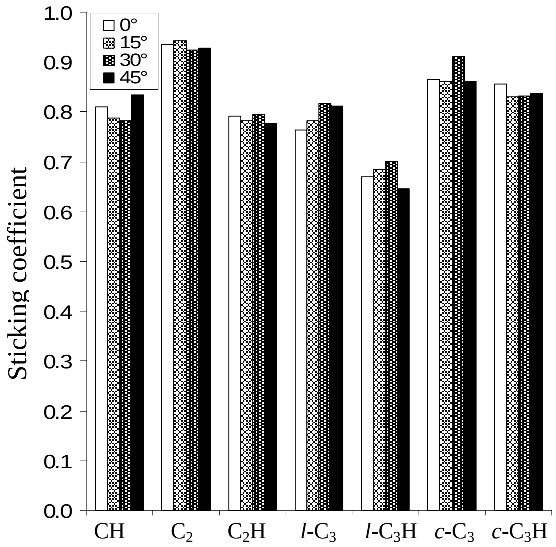

Figure 5.4: Calculated sticking coefficients of the different species as a function of their impact angle.

on a typical a-C:H surface. Additionally, the effect of the polar impact angle of the radicals was determined. The species and their translational energies were determined from an expanding thermal plasma experiment. It is found that the impact angle has no visible effect on the resulting sticking coefficients. The internal energy, on the other hand, has a pronounced effect on the calculated sticking coefficients. The effect is species dependent: while the sticking coefficient increases for the linear C_3, linear C_3H and cyclic C_3 species, it decreases strongly for CH, C_2H and cyclic C_3H. The sticking coefficient of C_2 shows no dependence on the internal energy. The results are explained in terms of the species structure, composition and reaction mechanism. These results are relevant for a-C:H film deposition techniques where growth proceeds through radical chemisorption, as *e.g.* in remote plasma sources. Furthermore, the sticking coefficients obtained can be used as input parameters in e.g. plasma simulations. The results also show that the reliability of MD simulations of thin film growth using low-kinetic energy species can be improved if experimental knowledge on the internal energies of the species is available. Finally, these results also substantiate the assumption of normal incidence made in the previous and the next chapers.

Chapter 6

Reaction behaviour of linear and cyclic C_3 and C_3H radicals and simulation of a-C:H film growth due to these species

Abstract

In this chapter, the simulated growth of thin a-C:H films is presented. The reaction mechanisms of both the linear and the cyclic isomers of C_3 and C_3H on an a-C:H surface are investigated. It is found that the cyclic species are always more reactive as compared to the linear species, due to their lower stability. The C_3 species are found to be more reactive than the C_3H species, due to steric hindrance of the H-atom, shielding the C-atom from the surface. The different mechanisms are discussed. The resulting film properties for different flux ratios of C_3 and C_3H have also been investigated. It is shown that films as deposited from C_3 and C_3H have a low density, and show low crosslinking. A clear change in microstructure is observed as the ratio between the cyclic and the linear species changes. These

simulations provide new insights into the reaction behaviour of the investigated species, and how this influences the resulting film properties.

6.1 Introduction

Different types of film can experimentally be deposited. Which kind of film is deposited in an ETP-based system is determined by the flux ratio of acetylene and Ar^+ ions. In Chapter 3, it was pointed out that a reasonable agreement with the experiment was achieved when considering low acetylene fluxes. However, simulation and experiment did not agree when considering higher acetylene fluxes. This result is not surprising, since the major growth species under this condition, C_3 and C_3H, were not yet included in the model presented in Chapter 3, as their role in the deposition process was only revealed in later experiments, carried out after these initial simulations. The present chapter therefore focusses primarily on these new species.

Indeed, it was experimentally established that the major growth species in the ETP-based deposition system depend on the ratio (F) between the C_2H_2 load and the Ar^+ and electron fluence emanating from the arc. At high C_2H_2 flows ($F > 1$), it was established that C_3 and C_3H are the major growth species, using Threshold Ionization Mass Spectrometry (TIMS) [4]. However, it was not established which isomers of C_3 and C_3H are actually present in the plasma and/or deposit on the surface of the growing film.

For both species, two relatively stable isomers can be distinguished: the linear isomers, l-C_3 and l-C_3H, and the cyclic isomers, c-C_3 and c-C_3H. In the gas phase, these species are relatively unreactive [163]. At an a-C:H surface, however, they become very reactive, as will be shown later. Also, due to their totally different structure, they will exhibit different reaction mechanisms with the surface. For example, the cyclic radicals are significantly less stable as compared to the linear species. Also, the carbon atoms in the cyclic radicals are more reactive than their counterparts in the linear species, due to their bonding configuration. Whether or not these radical dependent factors, and the corresponding reaction mechanisms co-determine the resulting film properties, has not yet been investigated. Furthermore, the investigation of the reaction behaviour of these species might also be important for other deposition techniques and in other fields, such as *e.g.* in interstellar space chemistry, since these species are relatively abundant in interstellar space [164].

Five different conditions have been investigated. These conditions are given in Table 6.1, showing the growth species used to deposit the film and their relative fluxes. For every impact, the choice of the impinging particle is determined using a random number and based on these relative fluxes. The conditions were chosen specifically to test how the deposition mechanism and the resulting film changes as the ratio between linear and cyclic growth species changes.

Table 6.1: Relative fluxes of the different growth species in the five films.

Film	linear C_3	linear C_3H	cyclic C_3	cyclic C_3H	linear total	cyclic total
Film 1	0.714	0.286	0.0	0.0	1.000	0.0
Film 2	0.714	0.143	0.0	0.143	0.857	0.143
Film 3	0.714	0.0	0.0	0.286	0.714	0.286
Film 4	0.357	0.143	0.357	0.143	0.500	0.500
Film 5	0.0	0.0	0.714	0.286	0.0	1.000

For the growth of the first film, simulated using l-C_3 and l-C_3H as the growth species, 2879 particle impacts were performed, of which 2065 l-C_3 impacts and 814 l-C_3H impacts. Hence, this film is deposited using only linear species for the growth process. In the deposition of the second film, using l-C_3 and both C_3H isomers, 2024 l-C_3, 410 l-C_3H and 385 c-C_3H were used, adding up to 2819 impacts in total. This adds up to about 14% of cyclic particles contributing to the film growth. For the third film, using l-C_3 and c-C_3H as growth species, 2331 impacts have been performed, of which 1636 l-C_3 and 695 c-C_3H impacts. For the growth of this film, the contribution of the cyclic species is now increased to about 29%. In the fourth film, using both C_3 isomers and both C_3H isomers, 2256 impacts were performed in total, of which 816 l-C_3 impacts, 320 l-C_3H impacts, 804 c-C_3 impacts and 316 c-C_3H impacts. Hence, about an equal amount of linear and cyclic species was used to deposit the film. Finally, 1802 impacts were performed to simulate the fifth film, of which 1295 c-C_3 impacts and 507 c-C_3H impacts. Hence, this film is entirely grown starting from cyclic particles.

The film deposited using l-C_3 and l-C_3H as growth species will be called “film 1” hereafter; the film deposited using l-C_3, l-C_3H and c-C_3H will be called “film 2”. Further, the simulated film using the l-C_3 and c-C_3H growth species is called “film 3”. The film simulated using l-C_3, c-C_3, l-C_3H and c-C_3H as growth species, is called “film 4”. The last film, deposited using c-C_3 and c-C_3H as growth species, will be called “film 5” hereafter. All films were grown until they reached a thickness around 18 nm.

From the impact numbers given above, it is already clear that the linear and the cyclic species have different sticking coefficients: almost 2900 impacts were needed to grow the first film, grown entirely from linear species; it has a thickness of about 17 nm. On the other hand, only 1800 impacts were needed to grow the fifth film, which was grown starting from cyclic species only, and which has a thickness of about 19 nm. Below we will discuss the sticking probabilities in detail. The results from this chapter are published in Journal of Applied Physics.

6.2 Results and discussion

6.2.1 Calculated film properties

In Fig. 6.1, the calculated structure of film 1 is shown as an example. The left hand side of the picture depicts the structure as it is deposited in total; the right hand side shows a more detailed view of two regions in the film. As can be seen, the film does not show much crosslinking (i.e., virtually no 4-coordinated C-atoms are present), but rather forms a chain-like network of sp and sp^2 bound carbon atoms, if we identify 1- and 2-coordinated C-atoms with sp carbons and 3-coordinated C-atoms with sp^2 carbons. This leads to porous structures. This is a general feature of the films deposited, which was observed in all five films grown (not shown). The microscopic details, however, depend on the applied conditions. While the overall structure of all five films is similar, they differ from each other in their microscopic structure. For example, in the first film, it can be seen from the detailed pictures (right hand side), that there are several transitions visible in the structure: very close to the substrate, a relatively dense structure is formed, followed by a region of very low density. Finally, the "equilibrium" structure is formed, showing a higher density. It should be emphasized that these structures are formed keeping the deposition conditions (temperature, species, species fluxes, ...) constant. Although different from one another, similar transitions are also observed in the other films.

Averaged over the bulk region of the films, the calculated density of the films is between 1.1 and 1.2 $g.cm^{-3}$ (cf. Table 6.2). A maximum film density is observed in the third film, which was grown using a ratio of about 70/30 between the linear and the cyclic radicals. Experimentally [4], the density was found to be in the range 1.5 $g.cm^{-3}$ and 1.7 $g.cm^{-3}$. However, the hydrogen content in the experimentally deposited films is about 30%, which can only be accounted for if an additional H-flux towards the substrate is present. In the next chapters, the effect of this

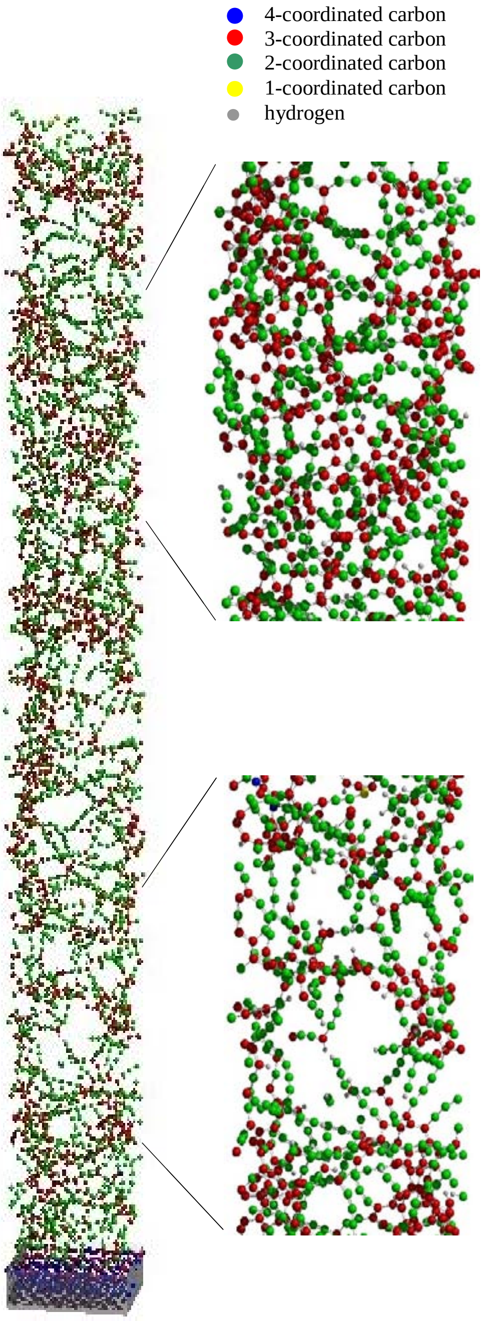
4-coordinated carbon
3-coordinated carbon
2-coordinated carbon
1-coordinated carbon
hydrogen

Figure 6.1: Calculated structure of film 1. The lefthand side shows the total structure. The righthand side shows two regions in detail, illustrating different structural properties.

additional H-flux will be thoroughly investigated. In the films deposited in this work, the H-content is about 8%. During the radical impacts, no H-atoms are eliminated from the surface. Hence, the stoichiometry of the film is entirely due to the stoichiometry within the particle fluxes.

The general structure of the films is further characterised by the coordination numbers of the carbon atoms. The average carbon coordination numbers Z_C and the sp^1 and sp^2 carbon fractions are given in Table 6.2. Z_C as a function of film thickness is shown in Fig. 6.2. It is clear from the table that the predicted structures are entirely composed of 2- and (especially) 3-coordinated C-atoms. Both Table 6.2 and Fig. 6.2 show, that the C-coordination number is the lowest in film 1, in agreement with the low density, increases as the fraction of cyclic species increases, and reaches a plateau when the flux of the cyclic species is about 30% of the total species flux towards the substrate.

Besides the C-coordination numbers, it is interesting to consider the distribution of C-C coordinations. For example, if a hard film is desired, one would try not only to maximize the sp^3 fraction in the film, but, more importantly, to increase the fraction of sp^3 C-atoms bound to other sp^3 C-atoms. In Fig. 6.3, the C-C coordination is shown for the five films. It can be seen in this figure that there

Table 6.2: Calculated mass density, average carbon coordination number, sp and sp^2 content of the five films.

Film	ρ (g.cm^{-3})	Z_C	sp^1	sp^2
Film 1	1.14	2.43	0.57	0.43
Film 2	1.15	2.52	0.48	0.52
Film 3	1.22	2.59	0.41	0.59
Film 4	1.13	2.59	0.41	0.59
Film 5	1.10	2.57	0.42	0.58

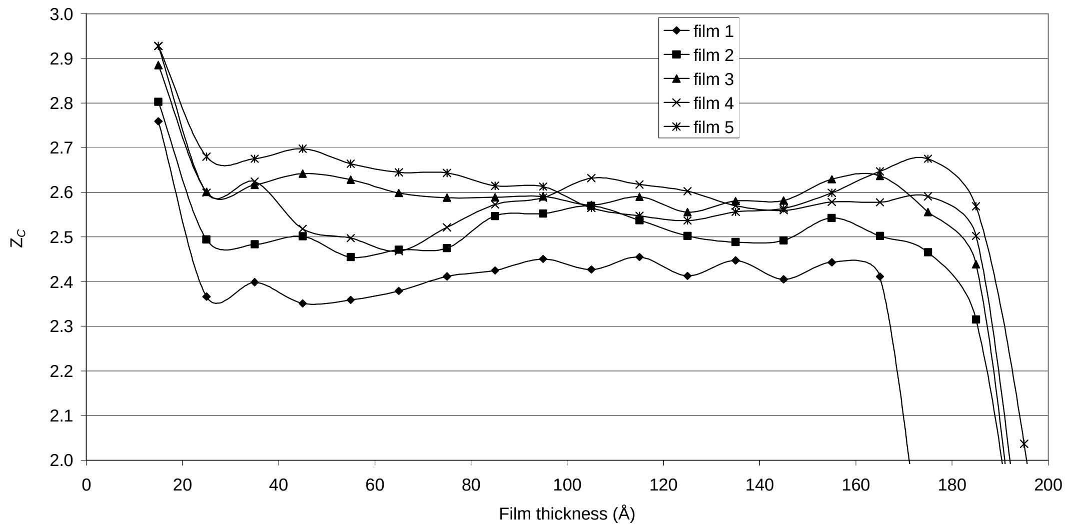

Figure 6.2: Average carbon coordination number Z_C as a function of the film thickness.

is a clear shift in their bond distributions. The fraction of 2-2 C-C bonds (i.e., the fraction of C-C bonds that connect a 2-coordinated carbon atom to another 2-coordinated carbon atom) decreases as the fraction of cyclic species sticking to the surface increases, corresponding to an increase in the fraction of 3-3 C-C bonds. This is directly related to the sticking mechanism of the different isomers, as will be explained in section 6.2.2.

Fig. 6.4 presents the calculated fractions of C-C bonds with a certain energy, relative to the total number of C-C bonds. Note that the single C-C bond as in ethane has a bond strength of about 3.6 eV, a double C-C bond as in ethene has an energy of 6.4 eV, a triple C-C bond as in ethyne 8.7 eV, a conjugated C-C bond as in benzene 5.2 eV and a C-H bond as in methane about 4.3 eV.

All films contain virtually only 2- and 3-coordinated C-atoms, and there are practically no C-C bonds stronger than 6.5 eV. Hence, triple bonds are entirely absent in all films. It is also clear from the figure that as the fraction of deposited linear species decreases, the fraction of "true" double C-C bonds decreases. While this

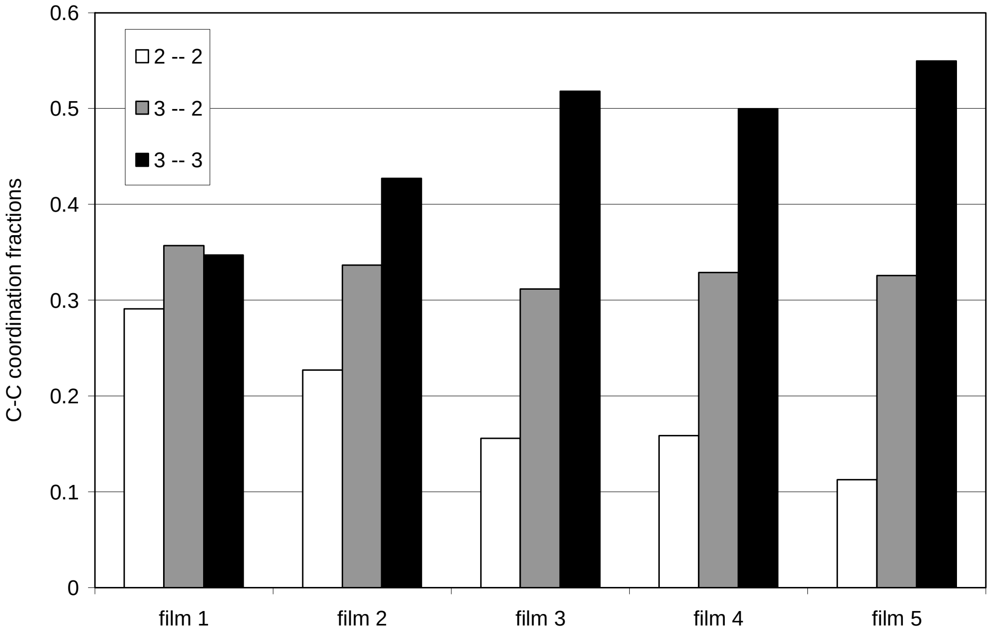

Figure 6.3: Calculated C-C coordination numbers in the five films.

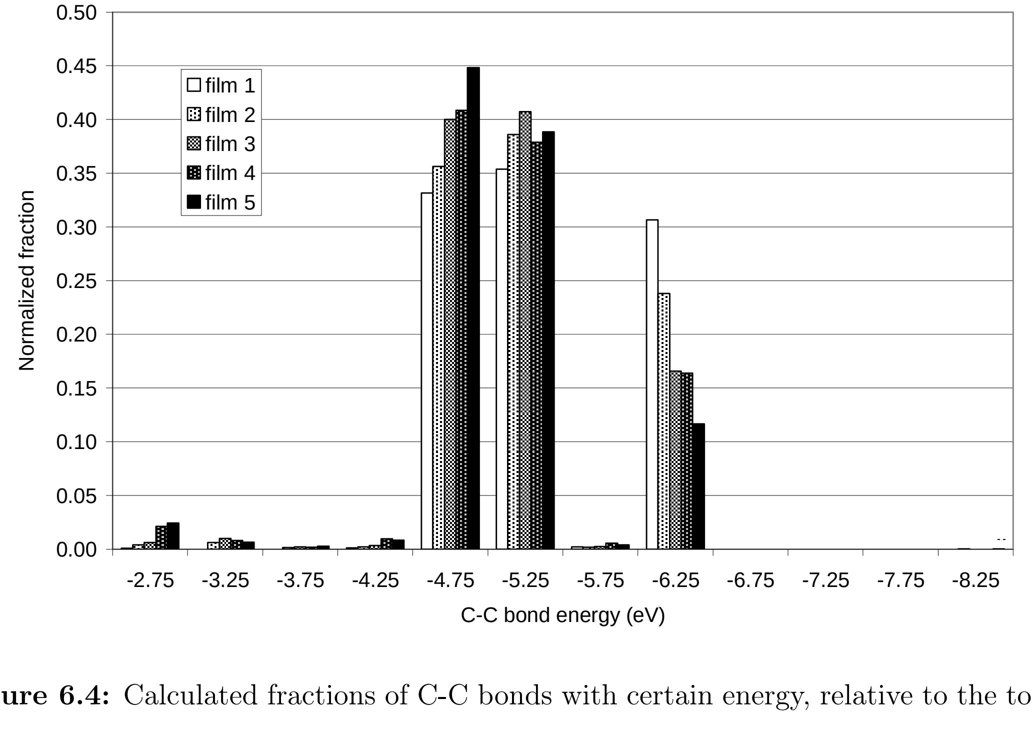

Figure 6.4: Calculated fractions of C-C bonds with certain energy, relative to the total number of C-C bonds, in the five structures.

fraction is about 0.32 in film 1 (deposited using only linear species), it is only about 0.12 in film 5 (deposited using only cyclic species). These double bonds can be attributed almost exclusively to 2-coordinated C-atoms. Although a 3-coordinated C-atom also forms either one double bond and two single bonds, or two double bonds, these bonds are conjugated, which explains the increasing fraction of bonds around 5.0 eV as the fraction of cyclic sticking species increases. Moreover, the fraction of single bonds, with an energy of about 3.5 eV, is negligible. Hence, it can be concluded that the 3-coordinated C-atoms form three similar bonds, resulting in a kind of polymeric structure.

6.2.2 Deposition characteristics of the *l*-C_3, *c*-C_3, *l*-C_3H and *c*-C_3H radicals

From the short analysis of the films given above, it becomes clear that the films are not very different from each other with respect to their general structure (i.e., comparable density and coordination fractions), but they do differ with respect to their microscopic structure (i.e., the C-C coordination distribution). Both the similarities and the differences can be explained by considering the actual growth of the film, and in particular the role of the reaction mechanisms of the different isomers with the surface structures formed.

The linear C_3 and C_3H radicals

The *l*-C_3 radical is a depositing species in films 1, 2, 3 and 4. It has a moderate sticking coefficient between 0.4 and 0.5. The *l*-C_3H species deposits in films 1, 2 and 4, and has a sticking coefficient between 0.3 and 0.4. The calculated values for the different films are given in Table 6.3. From this table, it is clear that their reactivity increases as the fraction of depositing cyclic species increases, as is especially clear for the C_3 radical. Moreover, when the fraction of depositing cyclic species increases, the *l*-C_3 radical sticks more with two atoms instead of one, indicative of a more reactive surface. In about 85% of its sticking events, it sticks with one of the outer carbon atoms, and in about 13% of the events with both of the outer carbon atoms. The middle carbon atom is fully bound, inducing repulsive forces between this atom and the surface during impact (cfr. Chapter 4). Hence, the middle carbon atom is virtually never involved in bonding to the surface [161]. The outer carbon atoms on the other hand have electrons not participating in the interatomic bonds in the gas phase, such that these are available for bonding to the surface. The average sticking energy for the C_3 radical is -5.29 eV when it sticks with one atom, and -9.96 eV when it sticks with both outer carbon atoms.

Table 6.3: Calculated sticking coefficients of the simulated species.

Film	linear C_3	linear C_3H	cyclic C_3	cyclic C_3H
Film 1	0.42	0.33	/	/
Film 2	0.43	0.36	/	0.56
Film 3	0.49	/	/	0.68
Film 4	0.52	0.38	0.66	0.62
Film 5	/	/	0.74	0.67

The situation is somewhat different for the *l*-C_3H radical. While the *l*-C_3 radical has two equivalent carbon atoms available for binding to the surface, one of the outer C_3H radical carbon atoms is shielded by the H-atom, leaving only one carbon atom readily available for binding to the surface. This explains its lower reactivity as compared to the C_3 radical. On average, its sticking energy is -5.21 eV.

When the *l*-C_3 radical sticks to the surface with one of its outer carbon atoms, the interatomic bond connecting the middle carbon atom and the surface binding atom becomes stronger with on average about 1.2%. The other bond, connecting the middle carbon atom and the atom that is not connected to the surface, becomes weaker with about 1.4%. When both outer carbon atoms are binding to the surface, both the intramolecular bonds become stronger, although only by about 0.5% or less. An example of the evolution as a function of time of the different *l*-C_3H bonds is shown in Fig. 6.5.

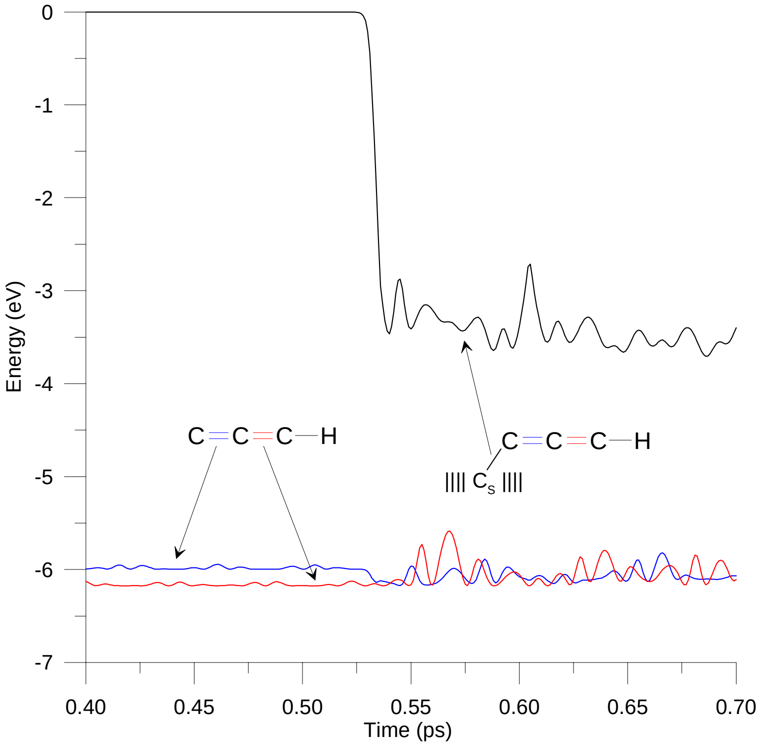

Figure 6.5: Time evolution of the bond energies in the C_3H radical upon impact and sticking on the surface.

In the case of the *l*-C_3H radical, the interatomic bond between the binding atom (almost invariably the outer, non-hydrogen carrying C-atom), and the central C-atom, becomes stronger with a value between 0.7% and 1.3%, increasing as the fraction of cyclic depositing species increases. The other interatomic C-C bond becomes weaker with about 1.6%.

If the linear C_3 radical sticks to the surface, the sticking atom becomes 2-coordinated. Hence, irrespective of how the radical sticks to the surface, the radical atoms do not become 3-coordinated upon impact. Obviously, they can become 3-coordinated as a result of later impacts. While the H-carrying C-atom in the linear C_3H radical could become 3-coordinated if it would bind to the surface, this mechanism almost never occurs, such that also the linear C_3H radical does not promote the sp^1 to sp^2 shift of one of its atoms. This explains the chain-like structures of films 1 and 2. (In film 2, only a fraction of 0.143 of the impacting species has a cyclic structure).

The cyclic C_3 and C_3H radicals

While the analysis of the impact behaviour of the linear isomers is relatively straightforward, the cyclic isomers show a more complex behaviour (cfr. Chapter 4). Nevertheless, several general trends can be observed. First of all, it should be pointed out that the cyclic radicals are structurally unstable. The ring strain in the cyclopropane molecule (cyclic C_3H_6), for example, is about 1.2 eV, lowering the bond strengths with about 32% as compared to the linear propane molecule. In c-C_3 and c-C_3H the bond strengths are lowered even more, by about 50% relative to the bonds in the linear isomers. Second, each carbon atom in the cyclic radicals has at least one electron available to share in chemical binding to the surface, contrary to the linear isomers. Hence, it is predicted that the reactivity of the cyclic isomers should be higher than the reactivity of the linear radicals. This is indeed substantiated by our simulations, as can be seen in Table 6.3. Further, the reactivity of c-C_3 should be higher than that of c-C_3H, since the H-atom on c-C_3H partially shields one carbon atom from binding to the surface. This effect is also seen in the simulations.

The cyclic C_3 radical is a growth species in films 4 and 5, showing a sticking coefficient of 0.67 and 0.74, respectively. In more than 70% of its sticking events, it sticks with one atom, to be compared with the value of 85% for the linear isomer. In the remaining 30% of its sticking events, the c-C_3 radical sticks with two atoms to the surface. This is a consequence of the fact that all of its carbon atoms are available for binding to the surface, contrary to the linear C_3 species. Hence, the reactivity and sticking behaviour of the cyclic radical are unaffected by the exact orientation of the radical relative to the surface, which is not the case for the linear isomer. When the *c*-C_3 radical sticks to the surface with one atom, the sticking energy is on average -5.37 eV; when two bonds to the surface are formed, the average sticking energy is -10.18 eV.

Upon impact, the *c*-C_3 molecule easily breaks up: in about 70% of its sticking events, the molecule first binds to the surface, immediately followed by breaking of one of the intramolecular bonds. An example of this process is shown schematically in Fig. 6.6. The figure shows that the *c*-C_3 radical can in fact become 3-coordinated upon impact, contrary to the linear isomer. Cyclic radicals that remain intact upon impact, can break up due to later impacts as well. Only a small fraction ($< 5\%$) will remain intact. As mentioned above, the driving force for this break up is the ring strain in this radical. When an intramolecular bond is broken, the ring strain is relieved, and a linear species is formed. Hence, the interatomic bond strengths in the radical are strongly increased, comparable to the bond strengths in the linear radicals (±5 eV). As a result, the single bonds of the gas phase cyclic radicals are converted into double bonds, leading to the bond energy histogram as shown in Fig. 6.4.

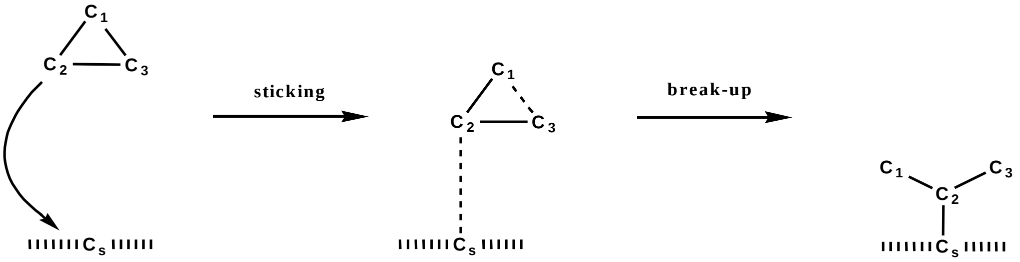

Figure 6.6: Schematic representation of the sticking and breaking up of an impacting cyclic C_3 radical. In this illustration, the C_1-C_3 bond breaks up, but obviously the C_1-C_2 or C_2-C_3 bonds can also break up upon impact.

As mentioned above, the linear C_3 radicals almost invariably stick with one of the outer carbon atoms, leading to 2-coordinated surface binding radical atoms upon impact. In contrast, in the case of a cyclic C_3 radical, the surface binding radical atom becomes 3-coordinated in more than 40% of the sticking events. This effect promotes the sp^1 to sp^2 shift of one of the atoms of the impacting c-C_3 radical. It can be concluded that this effect, together with the enhanced reactivity, induces the higher sp^2 fraction in the films deposited partially from cyclic radicals, as compared to the films deposited by mainly linear species.

The c-C_3H radical deposits in films 2, 3, 4 and 5. The general picture for c-C_3 remains largely unchanged when considering the c-C_3H radical. That is, a severe ring strain is present in the molecule, causing the molecule to break up easily upon impact, as well as the absence of a fully bound C-atom that would induce repulsive forces. Both factors enhance its reactivity as compared to the l-C_3H radical. Similar to the effect of the H-atom in l-C_3H, the H-atom in c-C_3H radical partially shields the carbon atom attached to it from the surface. Hence, most sticking events happen with one of the non H-carrying C-atoms ($>$ 80% in films 2 and 4). In film 3, this percentage of sticking with one atom is reduced to 77%, and in film 5 to 74%. Similar to the c-C_3 radical, the remainder of its sticking events involves the formation of two bonds, connecting two radical atoms to the surface. Sticking to the surface with one atom involves an energy of -5.30 eV, and -9.88 eV when sticking with two atoms.

The break-up mechanism occurs in only about 60% of its sticking events in films 2 and 4, to be compared with 70% for the c-C_3 radical. In the third film, the c-C_3H radical breaks up in 64% of its sticking events, and in 73% in the fifth film. Hence, except for the fifth film, the break-up percentage of c-C_3H is reduced by 5 to 10% as compared to the c-C_3 radical.

6.3 Conclusion

Molecular dynamics simulations have been performed to investigate the sticking behaviour and the reaction mechanisms of the deposition of the linear and cyclic isomers of C_3 and C_3H species at low impact energies. We have investigated how the different structure of the C_3 and C_3H species results in different sticking mechanisms on an a-C:H surface. We have shown that (1) the cyclic species are always more reactive as compared to the linear species, resulting in higher sticking coefficients; (2) the cyclic species always have one reactive carbon atom more than their linear counterparts, due to their bonding configuration; (3) the cyclic species are geometrically less stable than the linear species. This results in the cyclic radicals frequently breaking up, enhancing their reactivity; and (4) the C_3H radicals are less reactive than the C_3 radicals, due to steric hindrance by the H-atom, shielding the C-atom from the surface.

The resulting film properties for different flux ratios of cyclic C_3 and C_3H have also been investigated. It is shown that the deposited films have a low density and show low crosslinking. When predominantly linear growth species are used, a more chain-like structure evolves. Increasing the percentage of cyclic species impacting and sticking on the surface, the fraction of 3-coordinated C-atoms increases, at the expense of the 2-coordinated fraction. A maximum film density is obtained using a 70/30 mixture of linear and cyclic radicals.

Finally, under the growth conditions being considered, i.e. when only C_3 and C_3H contribute to growth, it has also been shown that H-elimination through incoming radicals does not occur; hence, the stoichiometry of the films is determined entirely through the stoichiometry of the sticking species. As mentioned above, the experimentally measured H-content of the films is about 30%, whereas the calculated H content is only about 8%. Moreover, the experimental density is higher than the simulated density (i.e., 1.7 g.cm^{-3} vs. 1.2 g.cm^{-3}). This illustrates that the physical picture of the a-C:H thin film deposition process is not yet complete, and it suggests that an additional H-flux, which cannot yet experimentally be determined, must be taken into account. Therefore, in the next chapters, the influence of the H-uptake during growth of the films is investigated.

Chapter 7

Influence of the H-flux on thin a-C:H film growth under $F < 1$ conditions

Abstract

In this chapter, MD simulations have been performed to investigate the growth of thin a-C:H films from radical species with thermal energy using additional H-fluxes towards the substrate. It is found that the incorporation of H into the film increases the mass density. The maximum mass density is reached for a H-flux of about 10%. The atom density of the films reaches a maximum at a H-flux of about 30%. It is shown that these effects are a result of the change in microstructure of the films, including a H-induced sp to sp^2 to sp^3 shift. These results are important for thin a-C:H film deposition techniques where chemisorption of radical species is the main growth mechanism.

7.1 Introduction

As mentioned in the previous chapter, the experimentally determined stoichiometry of the deposited films (i.e., with about 30% H-content) requires an additional H-flux towards the substrate. It is interesting to first study the influence of the H-flux on the film growth under the condition of low acetylene flux ($F < 1$, where $F = \Phi_{C_2H_2}/\Phi_{Ar^+}$), because under this condition the agreement between experiment and simulation was already reasonable (cfr. Chapter 3). Furthermore, recent CRDS and TIMS experiments revealed that under this condition, C_2H should also be considered as one of the growth species beside the species included already in Chapter 3. Therefore, in the present chapter the influence of an additional H-flux towards the substrate is first investigated for the condition $F < 1$, with the inclusion of C_2H in the model. In the next chapter, the influence of an additional H-flux will be investigated on film growth under conditions corresponding to a high acetylene flux (i.e., $F \gtrsim 1$).

It is well known that the hydrogen incorporation in the film is one of the key quantities determining the sp^2 and sp^3 proportions [165–167]. In order to better understand how H is incorporated into a growing film, and how this H incorporation influences the microstructure of the deposited a-C:H films, a series of simulations was performed in which thin a-C:H films were deposited under identical conditions, varying only the H-flux towards the substrate. Growth of the films was continued until the films reached a thickness of about 10 nm, each containing about 4000 atoms. After the growth phase, the films were allowed to relax for 10 ps. During the last picosecond of this relaxation, snapshots were taken of the configurations on the basis of which average quantities were calculated.

The relative particle fluxes as used in our model are given in Table 7.1. As mentioned above, the carbon containing growth species correspond to the experimental condition that the flux ratio $F < 1$. The hydrogen flux towards the substrate, however, could not be measured experimentally, and will therefore be varied in this study. We have chosen to allow an additional H particle flux towards the growing surface in the range between 0% and 45% of the total impacting particles flux. Here, we define the H particle flux as the number of H-impacts on the surface devided by the total number of particle impacts. In this way, we are able to monitor the change in microstructure and properties of the films grown, as a function of the H-incorporation in the film. In total, 13 different films have been deposited. The material from this chapter has been submitted to Applied Physics Letters.

Table 7.1: Relative fluxes for the different C-containing growth species, as obtained from experiment [4]. $\Phi_{H,rel}$ denotes the relative H-flux, varied in the range between 0.0 and 0.45.

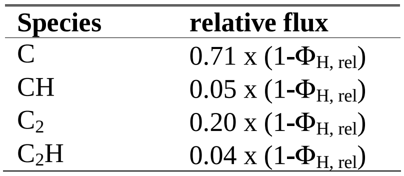

Species	relative flux
C	0.71 x (1-$\Phi_{H, rel}$)
CH	0.05 x (1-$\Phi_{H, rel}$)
C_2	0.20 x (1-$\Phi_{H, rel}$)
C_2H	0.04 x (1-$\Phi_{H, rel}$)

7.2 Results and discussion

Let us first consider how the different radicals interact with the growing surface. Since their kinetic energy is very low (0.13 eV), the subplantation mechanism does not occur, and the only process contributing to growth of the film is chemical reactions at the surface, i.e., chemisorption. This process is dependent on the structure of the surface itself. Hence, a given radical can react differently on different surfaces, leading to different films (cfr. Chapter 4). As the relative H-flux towards the substrate increases, the H-content (atomic fraction) in the film increases proportionally. There is an almost linear correspondence between the

H-flux and H-incorporation in the film, as can be seen in Fig. 7.1 (see inset). Vice versa, the H-flux towards the substrate, which is difficult to measure, can thus be estimated from the measured H-content in the film. Also, the H-distribution among the C-atoms in the films is directly related to the H-content, as can be seen in Fig. 7.1. Here, the calculated fractions of C, CH and CH_2 groups in the films are shown as a function of the H-content. As can be expected, the fraction of C-atoms carrying both 1 and 2 H-atoms increases as the H-flux towards the substrate increases. The fraction of chain-terminating CH_3 groups was found to be negligible in all simulated films.

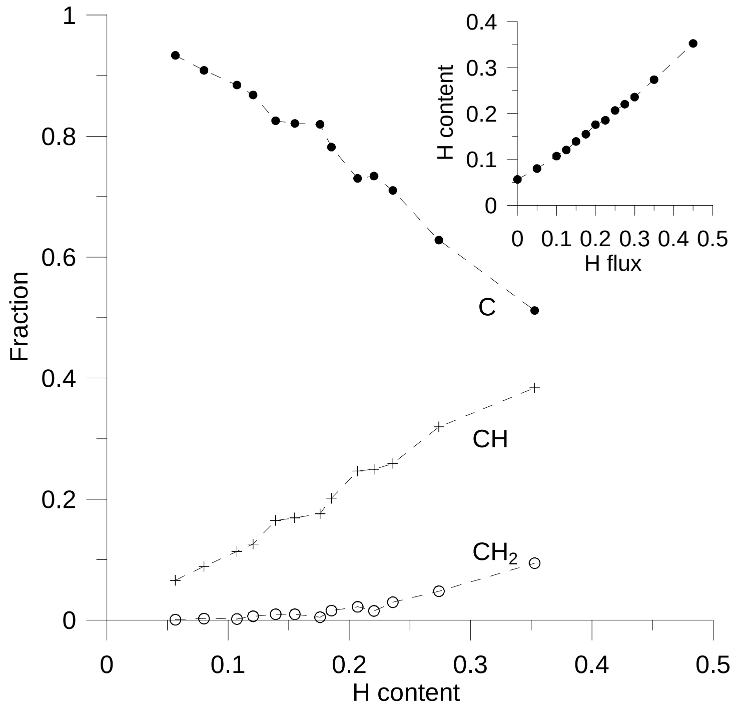

Figure 7.1: Calculated hydrogen distribution among the C-atoms as a function of the H content in the film; the calculated H content in the films as a function of the H-flux is shown in the inset.

Very high hydrogen fluxes make the resulting structure more porous and less dense, as will be shown below. The decrease in mass density of a-C:H films with increasing

H content has already been shown – see *e.g.* Ferrari *et al.* for films containing more than 40% sp^3 content [166], and references therein. In Fig. 7.2, it is shown that this effect also occurs under the conditions used in this study for high enough H-fluxes. However, at low H-fluxes, the mass density appears to increase with increasing H-flux. This figure shows the calculated mass density and atom density of the different films as a function of the H-content in the bulk of the film. A maximum in the mass density is found at a H-content of about 10% - 12.5%. The atom density, however, continues to increase as a function of the H-content. Indeed, a high hydrogen flux allows the incorporation of a large H-fraction into the carbon matrix, increasing the atom density. This does, however, not increase the mass density due to the low hydrogen mass. A maximum in the atom density is found at a H-content of about 22%, corresponding to a H-flux of about 30%, according to Fig. 7.1. The occurrence of bulky CH_2 groups (which occupy a large volume) at high H particle fluxes (see Fig. 7.1), accounts for the decrease in both the mass density and atom density at a H-content $> 25\%$. Also, as more H is incorporated into the film, relatively less C-atoms must accommodate relatively more H-atoms, increasing the average carbon coordination number, in the range 2.8 - 3.1 for a H particle flux varying from 0% to 45%.

Hydrogen also changes considerably the microstructure of the films. In Fig. 7.3, the evolution of the sp^1, sp^2 and sp^3 C-sites in the bulk of the film is plotted as a function of the H-content. Here, a carbon site is designated sp^1 if the carbon atom is 1- or 2-coordinated. Likewise, sp^2-sites and sp^3-sites are identified as 3-coordinated and 4-coordinated C-atoms, respectively. It can be seen in the figure that low H-fluxes lead to a lowering of the sp^1-content, an increase in the sp^2-content, and a slight increase in the sp^3-content. This transition from sp^1 to sp^2 as a function of the H-content in the film coincides with the maximum in the mass density. In this region, the film structure is composed of a network of sp^2-like C-C bonds, stabilized by chemical resonance. As the sp^1-sites occupy a larger volume

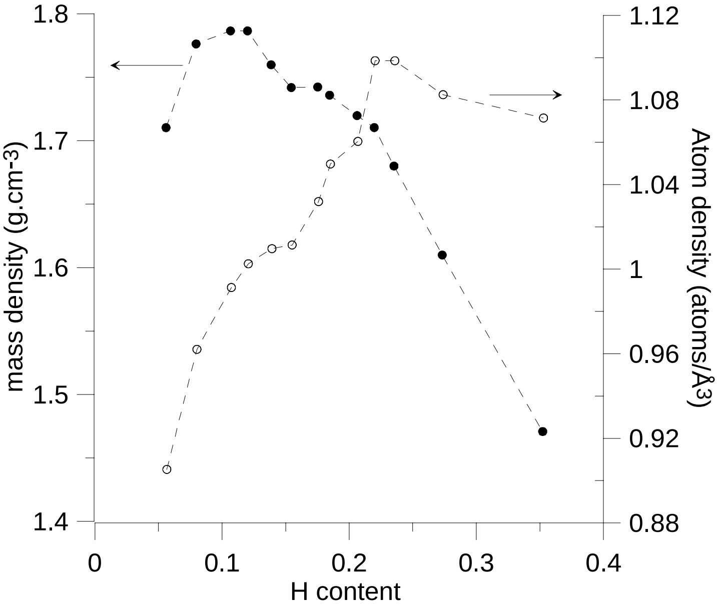

Figure 7.2: Calculated mass densities and atom densities as a function of the H content in the films.

per atom than sp^2-sites (sp^1-sites are linear 1-dimensional structures while sp^2-sites are 2-dimensional), the sp^1 to sp^2 transition effectively lowers the volume per atom, and hence increases the mass density.

Higher H-fluxes further lower the sp^1-content, and strongly increase the sp^3-content, whereas the sp^2 content remains more or less constant. In this region, a considerable fraction of the film volume is taken by the H-atoms, contributing only to the atom density, and hardly to the mass density. Hence, the films now become more porous and less dense.

At even higher H-fluxes ($\Phi_{H,rel} > 0.30$), the sp^2 carbon atoms are converted into sp^3 carbons, coinciding with the maximum found in the atom density. As can be seen in Fig. 7.1, the fraction of bulky CH$_2$ groups now becomes important. These groups repel each other, such that from this point on, both the atom density and the mass density decrease. Hence, as the H-flux towards the substrate increases,

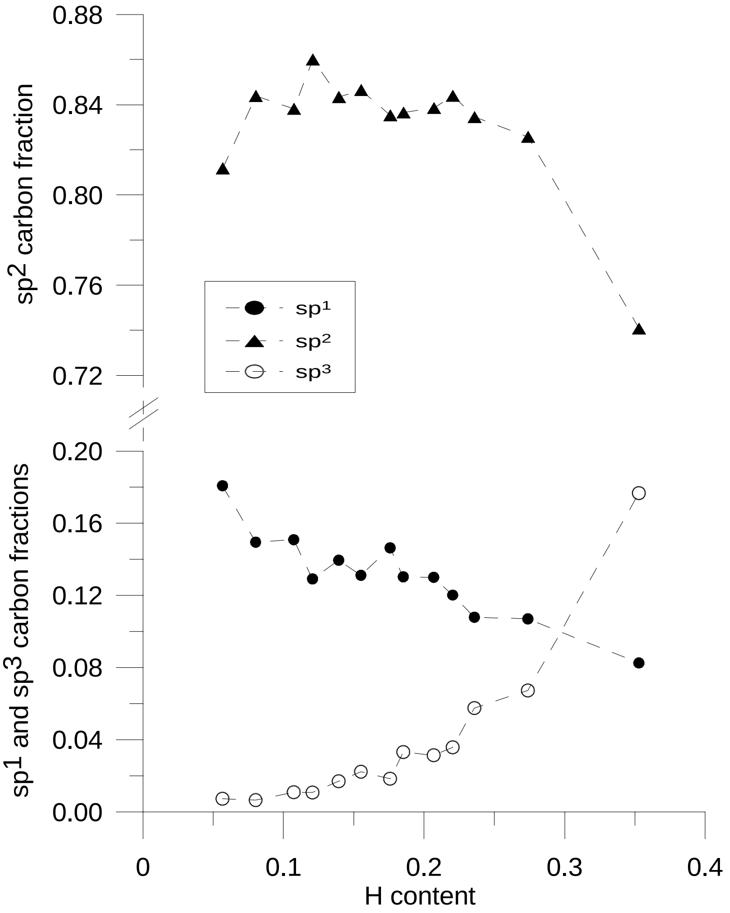

Figure 7.3: Calculated sp^1, sp^2 and sp^3 C-fractions as a function of the H-content in the films.

there is a H-induced sp^1 to sp^2 to sp^3 shift.

Finally, the calculated sticking coefficients of the different species are shown in Fig. 7.4. It can be seen that the sticking coefficients decrease as a function of the H-flux towards the substrate (or H-content in the film). The sticking coefficient of a specific radical with a specific energy depends on the availability of reactive C-sites at the surface, capable of accommodating the incoming radical. Since hydrogen passivates these reactive sites at the surface, less reaction sites remain as the H-content in the film increases, leading to the decrease in the sticking coefficients. Nevertheless, all sticking coefficients are calculated to be rather high (in the range

0.96 - 0.41), since the species under study are highly reactive radicals. It is found that C and C_2 are the most reactive species, due to their unshielded lone electrons. The C_2H radical is overall the least reactive species: the C-atom to which the H-atom is attached virtually never sticks to the surface, due to the shielding by the H-atom. Hence, its reaction probability is dependent on its orientation upon impact, in contrast to C_2. Although the C-atom in CH is also shielded by a H-atom, this radical is slightly more reactive than C_2H due to its higher radical character. The H-atoms show a sticking coeffient comparable to the CH and C_2H sticking coefficients throughout the different films.

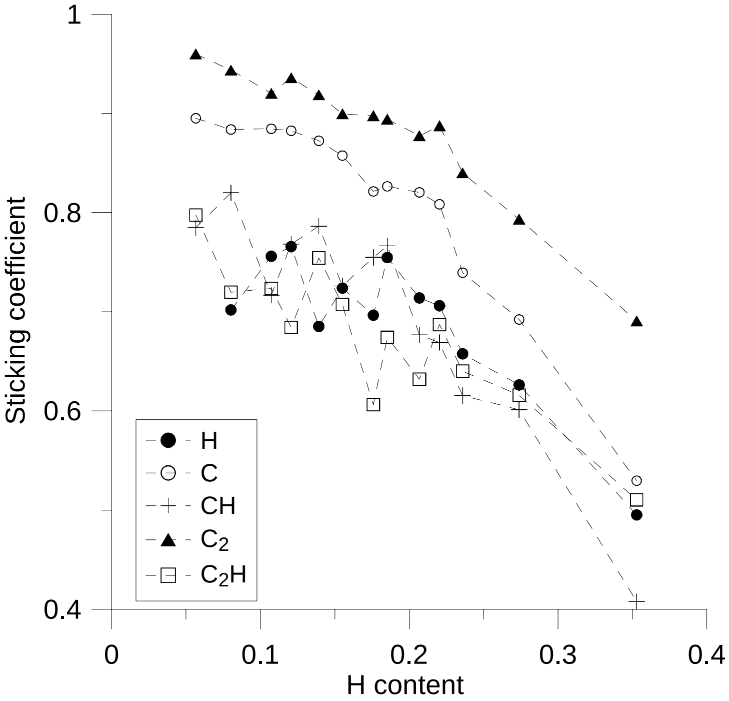

Figure 7.4: Calculated sticking coefficients of the various C-containing growth species, as a function of the H-content in the films.

7.3 Conclusion

Combining these data allows the following conclusions to be drawn. The sticking probability of the species is found to strongly depend on the H-content of the film. The H-uptake in the film is quasi linearly dependent on the H-flux. At low H-fluxes, some hydrogen is incorporated into the film, leading to an increase in the atom density. This also leads to a conversion of sp^1 to sp^2 carbon sites, coinciding with an increase in the mass density. The maximum mass density of 1.79 $g.cm^{-3}$ is found at a H content of about 10%. Higher H-fluxes bring more H into the film, leading to a higher atom density, but a lower mass density, while sp^1 C-sites are further converted to sp^2 sites, and sp^2 sites to sp^3 sites. Finally, at even higher H-fluxes, the mass density keeps decreasing, and a maximum is found in the atom density, at a H-flux of 30%. From this point on, the sp^2 content starts to decrease, coinciding with a decrease in the atom density and an increase in the fraction of CH_2 (see Fig. 7.1). Experimentally, a H content of about 33% was found and a mass density of about 1.5 $g.cm^{-3}$, corresponding very well with our simulations. From these results, the H-flux towards the substrate can be estimated by measuring the H-content in the films. Also, these results suggest how a-C:H films, grown from low-kinetic energy radicals, can be densified using low H-fluxes. In the next chapter, this effect will be shown to be of a more general nature.

Chapter 8

Generalized effect of an additional H-flux, as well as a C-fluxes on the growth of thin a-C:H films, under $F \geq 1$ conditions

Abstract

In this chapter, MD simulations have been performed to investigate the role of additional H- and C-fluxes on the structure and growth of thin a-C:H films under ETP conditions with high fluxes of acetylene. A first series of simulations was carried out based on experimentally observed hydrocarbon radicals and additional H-fluxes to grow the films. A second series of simulations was performed to investigate the influence of a fixed additional C particle flux towards the substrate. It is found that the H-incorporation into the film again considerably changes the microstructure of the film. An increase in the mass density is found at low H-flux, up to a value of 20%, while a decrease in the mass density is found when using higher H-fluxes. The additional C-flux increases the mass density further. The

results are explained in terms of the role of the H-atoms in the film and the deposition behaviour of the hydrocarbon radicals. These results provide information regarding the deposition and structure of thin a-C:H films grown in general from low-kinetic energy hydrocarbons, suggesting that densification, and hence hardening of the films is possible, even without additional ion bombardment, by applying an additional thermal H-flux and/or C-flux towards the substrate.

8.1 Introduction

In the previous chapter, it was shown how a low H-flux can induce microstructural changes in the film, including densification of the film, for ETP-conditions $F < 1$. In this chapter, this result is generalized to F-independent conditions. Recall the definition of F:

$$F = \frac{\Phi_{C_2H_2}}{\Phi_{Ar^+}} \tag{8.1}$$

In a first set of simulations, the influence of the H-flux on the film was studied for conditions corresponding to ETP ($F > 1$) conditions. From here on, we refer to these simulations as "simulation set 1". A second series of simulations, referred to as "simulation set 2" from here on, was also performed. Simulation set 2 was identical to simulation set 1, except for an additional C-flux of 10% towards the substrate, i.e., 10% of all the particle impacts on the substrate were C-atom impacts. Indeed, we want to investigate also the influence of an additional C-flux on the film properties. It is expected that the C-flux might increase the mass density relative to films deposited without the additional C-flux, because a free C-atom can accommodate up to 4 neighbors, while the accommodation of more than two neighbors by a C-atom originating from a C_3 radical requires a rehybridization of the C_3 radical during its surface chemistry, which is unlikely due to the low kinetic energy of the incoming particles. The relative particle fluxes of the selected growth species as obtained from experiment are given in Table 8.1.

Table 8.1: Selected growth species and their relative fluxes towards the substrate. $\Phi_{H,rel}$ is the relative H-flux towards the substrate, in the range between 0 and 0.45.

Species	Relative flux, 0% C (Simulation set 1)	Relative flux, 10% C (Simulation set 2)
C_3	0.714 x (1-$\Phi_{H, rel}$)	0.642 x (1-$\Phi_{H, rel}$)
C_3H	0.143 x (1-$\Phi_{H, rel}$)	0.129 x (1-$\Phi_{H, rel}$)
cyclic C_3H	0.143 x (1-$\Phi_{H, rel}$)	0.129 x (1-$\Phi_{H, rel}$)
H	$\Phi_{H, rel}$	$\Phi_{H, rel}$
C	0.0	0.10

Since the F-ratio determines the growth species, the films as deposited under $F < 1$ and $F > 1$ conditions are inherently different. We have already demonstrated how the H-atoms induce a sp^1 to sp^2 to sp^3 shift for $F < 1$ conditions. This in turn leads to a densification of the films deposited under $F < 1$ conditions. In this chapter, we demonstrate how the role of the H-atoms is of a more universal nature. Indeed, it appears that independent of the exact F-value, and hence of the exact growth species playing a role in the deposition process, the H-atoms change the microstructure of the deposited films, resulting in a densification of the films. The results are not only important for ETP-based deposition, but more generally for any experimental thin a-C:H film deposition technique in which low-kinetic energy hydrocarbon radicals are responsible for growth of the film.

Using relative H-fluxes in the range between 0 and 0.45 (defined as the number of H-atom impacts divided by the total number of particle impacts), in total 15 films were deposited for simulation set 1. For simulation set 2, H-fluxes in the range between 0 and 0.35 were chosen to simulate another 5 films. The results from this chapter have been submitted to Physical Chemistry - Chemical Physics.

8.2 Results and discussion

8.2.1 Simulation set 1: Influence of the H-flux without additional C-flux

The uptake of H-atoms into the film increases nearly linearly with the H-flux towards the substrate, as demonstrated in Fig. 8.1 (solid line). Note that when no additional H-flux towards the substrate is applied, the H-content in the film is about 9%. This results from the incorporated C_3H radicals in the film, and corresponds to the minimum H-content possible in films grown under the selected conditions. As will be shown in the following, the H-content in the film determines all other film properties.

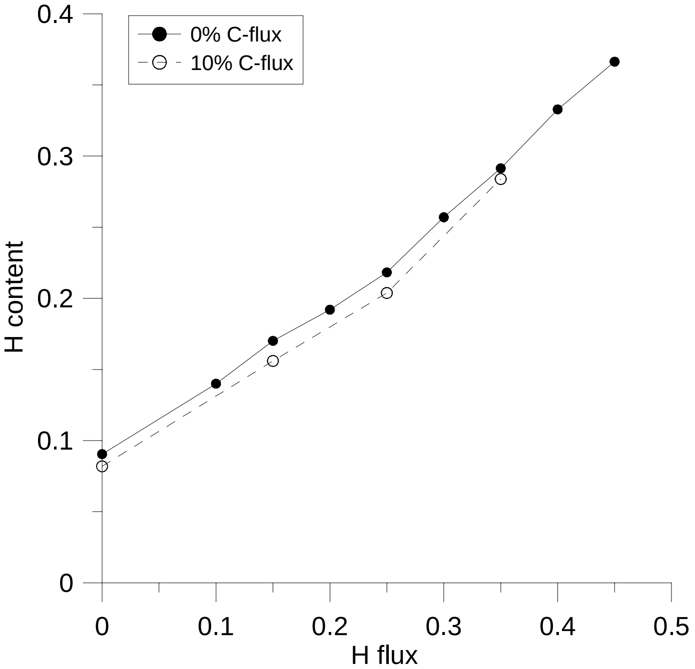

Figure 8.1: Calculated H content in the simulated films as a function of the H-flux towards the substrate, with and without additional C-flux.

In Fig. 8.2 (solid line), the calculated mass density of the simulated films is shown as a function of the H flux. Combining figures 1 and 2, it can be seen that increasing the H-flux, which results in a higher H-content in the film, also increases the mass density of the film. A maximum is found at a H-content of about 22%, corresponding to a relative H-flux of 0.25. At higher H-fluxes, a decrease in the mass density is observed. In the previous chapter, the increase in mass density of a-C:H films using low H-fluxes under $F < 1$ conditions was already demonstrated. This result is now generalized by these simulations, independent of the exact conditions and growth species. The decrease in mass density of a-C:H films with higher H-content has previously already been shown, *e.g.* by Ferrari *et al.* [166], and references therein. However, the fact that a low H-flux can yield a rise in mass density was, to our knowledge, not yet reported before, and can have important consequences for practical deposition techniques without additional substrate bias.

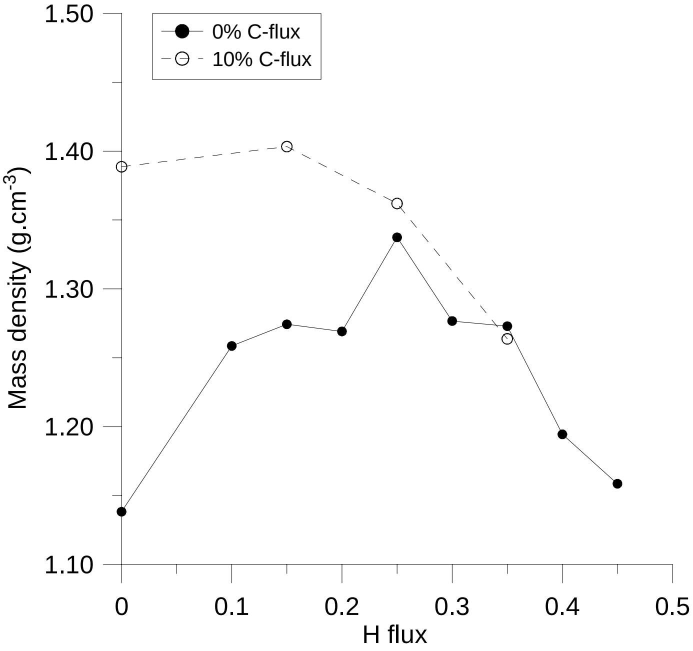

Figure 8.2: Calculated mass densities of the simulated films as a function of the H-flux towards the substrate, with and without additional C-flux.

In Fig. 8.3 (solid lines), the calculated average C-C bond energy (full circles) and the calculated average C-coordination number in the films (open circles) are plotted as a function of the H-flux. It is clear that as the H-flux towards the films, and hence the H-content in the film increases, the average C-C bond energy decreases (i.e., becomes less negative, from -5.2 till -4.9 eV) and the average C-coordination number increases in a similar fashion (i.e., from 2.5 till almost 3). This behaviour is closely related to the C-C coordination fractions, as shown in Fig. 8.4. Here, the fraction of m-coordinated C-atoms that is bound to an n-coordinated C-atom is shown for the films deposited under different H-fluxes. It can be seen how the fraction of binding to low-coordinated C-atoms decreases while the fraction of binding to higher coordinated C-atoms increases as the H-flux towards the films, and hence the H-content in the film increases. It appears that bonds between two 3-coordinated C-atoms are mostly present in the film, and especially at high H-fluxes (and H-content in the film). Bonds with 2-coordinated C-atoms are also present, but bonds with 4-coordinated C-atoms appear to be almost negligible.

As is clear from Fig. 8.5, the films are composed of essentially three types of C-C bonds: single bonds, having energies of about 3.5-4 eV, double bonds, with a binding energy of about 6-6.5 eV, and bonds in between, that are partially stabilized by chemical resonance. The strength of the latter bonds extends in the range between 4.5 eV and 5.5 eV. As the H-flux towards the films, and hence the H-content in the film, increases, the fraction of double bonds decreases, while the fraction of single bonds increases. Moreover, the fraction of bonds between 4.5 and 5 eV decreases, whereas the fraction between 5 and 5.5 eV increases as a function of the H-flux.

At low H-content, the fraction of 2-coordinated (sp^1) C-atoms is considerable (see Fig. 8.4), leading to the formation of strong double bonds (cf. Fig. 8.5), and the creation of linear structures. The formation of these linear structures leads to a low

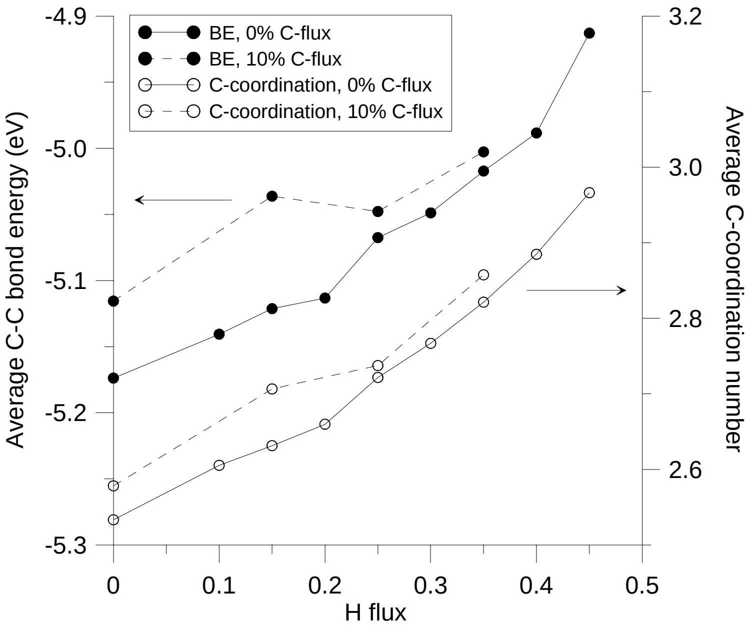

Figure 8.3: Calculated average C-C bond energy (BE) and average C-coordination number in the different simulated films, as a function of the H-flux towards the substrate, with and without additional C-flux.

mass density in the film. As the H-content increases, the fraction of 3-coordinated carbon atoms increases at the expense of the fraction of 2-coordinated C-atoms (see Fig. 8.4). This can also be seen in Fig. 8.6 (solid lines). From this figure, it is clear how the H-atoms convert the sp^1-type C-atoms into sp^2-type C-atoms. Note that sp^1-type C-atoms form either a triple bond and a single bond, or two double bonds. In the deposited films, however, there are almost no triple bonds formed. Sp^2-type C-atoms form a double bond and two single bonds. Hence, as the sp^1-type C-atoms are converted into sp^2-type C-atoms, the fraction of double bonds in the film decreases, and is replaced by a network of planar 3-neighbour structures, held together by resonantly stabilised bonds. This leads to an increase in the mass density, since these 3-neighbor structures have an increased mass-over-volume ratio as compared to the linear 2-neighbor structures.

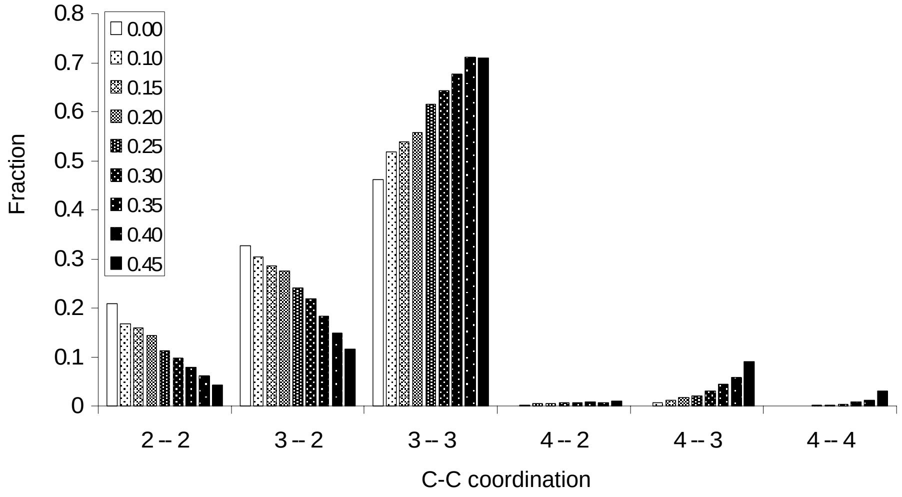

Figure 8.4: Calculated C-C coordination numbers of the different films, for different H-fluxes towards the substrate (as given in the legend), without additional C-flux. The bars show the fraction of m-coordinated C-atoms connected to n-coordinated C-atoms. The values on the abscissa denote m and n.

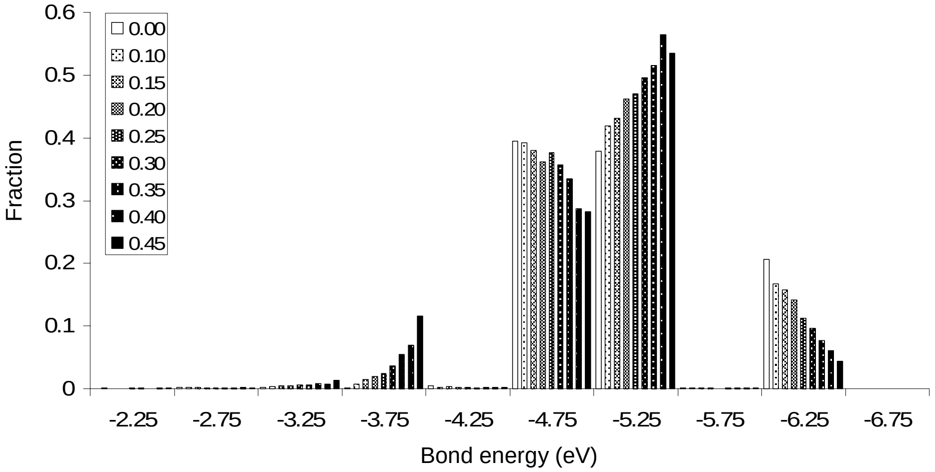

Figure 8.5: Calculated fraction of C-C bond energies in the different films, for different H-fluxes towards the substrate (as given in the legend), without additional C-flux. The bin interval is 0.5 eV.

At the same time, however, the fraction of CH and CH_2 fragments in the film increases. This can be seen in Fig. 8.7 (solid lines). These fragments occupy a much larger volume than a C-fragment does, while contributing only slightly more

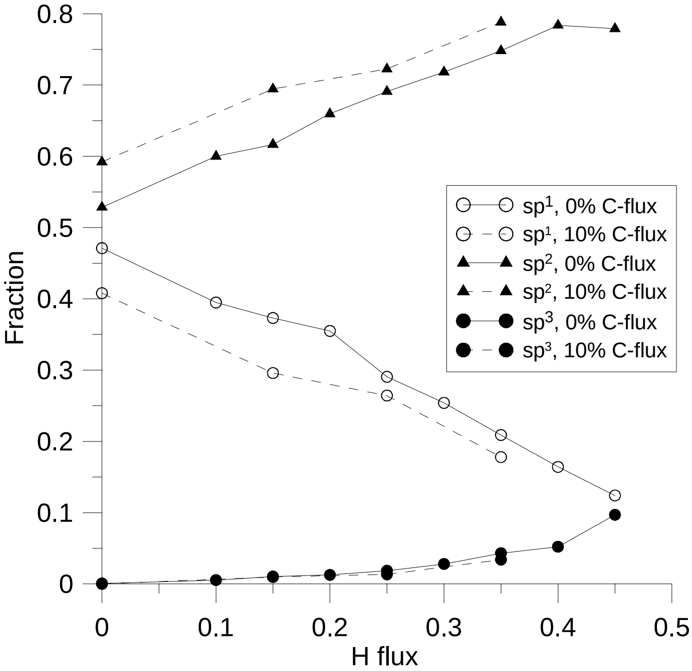

Figure 8.6: Calculated fractions of sp-type, sp^2-type and sp^3-type carbon atoms in the films, as a function of the H-flux towards the substrate, with and without additional C-flux. Here, the sp-hybridisation is identified with 1- and 2-coordinated C-atoms. Likewise, 3-coordinated C-atoms are denoted here as sp^2 and 4-coordinated C-atoms are denoted as sp^3 C-atoms.

to the mass of the film in comparison to a C-fragment. Hence, the increase in these CH and CH_2 fractions will lead to a decrease in the mass density. Therefore, the sp^1 to sp^2 conversion as a function of increasing H-flux, on one hand, and the increase in CH and CH_2 fractions, on the other hand, have the opposite effect. Consequently, a maximum in the mass density is found at a H-flux of 25% , since at low H-content, the importance of the CH and especially the CH_2 fragments is still of minor importance, while the fraction of sp^2 (i.e., non-linear) fragments is already considerable. At higher H-fluxes, however, the H-content in the film increases proportionally, and the mass-over-volume effect of the CH and CH_2 fragments becomes dominant. The role of the H-atoms is therefore to induce a microstructural shift in the films: as the fraction of C-fragments is converted into CH and CH_2 groups, the fraction of sp^1-like carbons is converted into sp^2-like carbons. This process increases the average C-coordination number, and, at low H-flux and H-content (< 20%), also the mass density. At higher H-content, the CH groups and CH_2 groups become ever more important, increasing the volume without adding additional mass. This then leads to a decrease in the mass density. Hence, using high H-fluxes, the films become more porous and less dense.

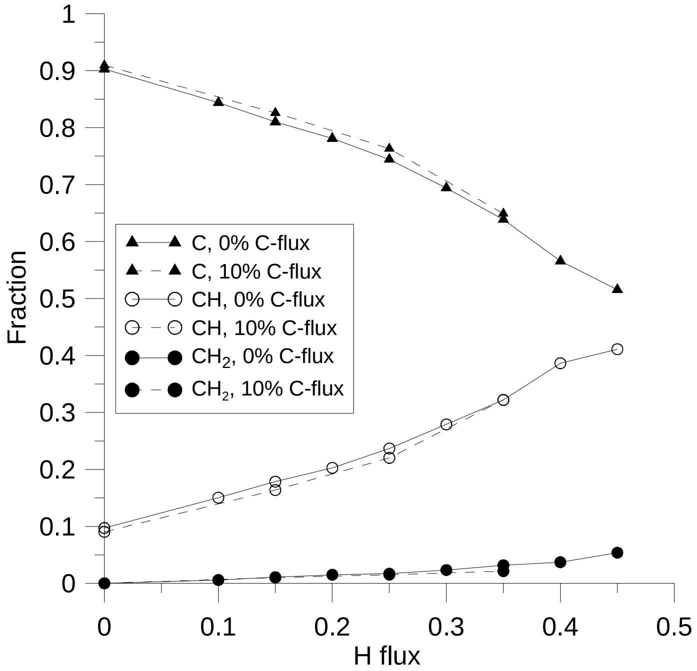

Figure 8.7: Calculated fractions of C, CH and CH_2 fragments in the films as a function of the H-flux towards the substrate, with and without additional C-flux.

8.2.2 Simulation set 2: Influence of the H-flux with additional C-flux of 10%

In general, our calculations predict that the influence of an additional C-flux towards the substrate is to promote the formation of an improved film, in terms of the mass density and the coordination in the film. The H-uptake in the film is virtually identical to simulation set 1, as can be seen in Fig. 8.1 (dashed line). Overall, the H-content in the films in simulation set 2 is only about 1.5% lower as compared to the films produced in simulation set 1. Hence, the total H-uptake in the film is not much influenced by the additional C-flux.

Fig. 8.2 (dashed line) shows that the mass density of the films simulated using low H-fluxes in simulation set 2 is considerably higher as compared to simulation set 1. A maximum mass density of 1.40 g.cm^{-3} is found at a H-flux of 15%, but this value is more or less the same as for the film obtained without additional H-flux. For H-fluxes higher than 15%, the mass density decreases again.

In Fig. 8.8, a representative section of the structure of three of the simulated films is shown. It can be seen that the film in the left panel, deposited without C- or H-flux, has the most porous structure. The mass density of this film was calculated to be 1.14 .cm^{-3}. The middle panel shows the most dense film obtained without the additional C-flux, i.e., using 25% H-flux. The mass density of this film was calculated to be 1.34 g.cm^{-3} (cfg. Fig. 8.2). The panel on the right shows the most dense film deposited using the additional C-flux, i.e., using 15% H-flux. The mass density of this film was calculated to be 1.40 g.cm^{-3}. From the figure, it is clearly visible that the films deposited using the additional C- and H-fluxes are more dense as compared to the film deposited without C- or H-flux.

The increase in mass density at low H-fluxes in simulation set 2 compared to simulation set 1 is consistent with the somewhat higher average carbon coordination number (Fig. 8.3), and the increased sp^2-fraction (Fig. 8.6). Indeed, our calculations predict that the C-atoms incorporated in the film in simulation set 2 take over the role of the H-atoms in simulation set 1, that is, to convert sp^1-sites into sp^2-sites, causing the increase in the mass density. The increase in the average C-coordination number is a direct consequence of the additional C-atom incorporation in the films.

8.3 Conclusion

Molecular dynamics simulations have been performed to investigate the role of H-atoms on the structural composition of thin a-C:H films grown from low-kinetic energy hydrocarbon radicals. It is found that increasing the H-flux towards the substrate leads to a nearly linear increase in the H-content in the film. At low H-content, an increase in the mass density is found, reaching a maximum at a H-flux of 25% and a H-content of about 0.22. This densification process is caused by the conversion of linear 2-coordinated structures (sp^1-type) into planar 3-neighbour structures (sp^2-type). As the H-flux towards the film increases further, and the H-content in the film exceeds about 25%, the fractions of CH- and CH_2-fragments occupy such a large volume, that the mass density starts to decrease. When an additional C-flux towards the substrate is applied, an increase in the mass density is observed at low H-fluxes, coinciding with an increase in the sp^2-fraction. These

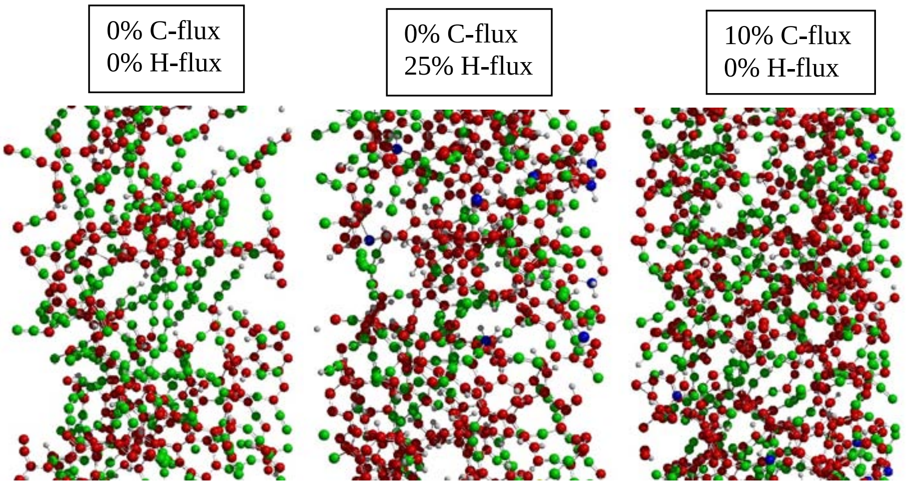

Figure 8.8: Schematic picture of the structure of three simulated films. For the sake of clarity, only a representative part of the films is shown. The red balls are three-coordinated C-atoms, and the green balls are two-coordinated C-atoms. Four-coordinated C-atoms appear to be absent. The small grey balls represent H-atoms.

results are of great importance for a-C:H thin film deposition with the ETP set-up. Moreover, they are more in general relevant for any deposition systems in which growth proceeds, or at least partially proceeds, through chemical surface reactions without subplantation. Indeed, they suggest that densification of the films is possible without substrate bias, by an additional H- and/or C-flux.

Chapter 9

General conclusions

The growth process of thin amorphous hydrogenated carbon (a-C:H) films was simulated using self-consistent molecular dynamics simulations. It was possible to elucidate the reaction behaviour of several hydrocarbon radicals on a-C:H surfaces, as well as the actual growth mechanisms of thin a-C:H films. The input parameters for several of the simulations performed in this work stem from the experimental expanding thermal plasma (ETP) deposition of thin a-C:H films [168]. In the ETP setup, low-kinetic energy hydrocarbons chemically react at the substrate creating a thin a-C:H film. Experimentally, it was established that a key parameter to determine the growth process is the ratio between the acetylene flux and the Ar^+ ion flux: $F = \Phi_{C_2H_2}/\Phi_{Ar^+}$. Under $F < 1$ conditions, the major growth species are C, CH, C_2, and C_2H, whereas under $F > 1$ conditions, the main growth species are presumed to be linear and cyclic C_3 (l-C_3 and c-C_3, respectively), and linear and cyclic C_3H (l-C_3H and c-C_3H, respectively).

It is important to realize, however, that the results presented in this work are of a more general nature. Indeed, the results are not only applicable to thin a-C:H film growth using the expanding thermal plasma (ETP) source, but also to any other deposition system in which low-energy radicals are responsible for growth of the films. Furthermore, the information on sticking coefficients, and on the reaction mechanisms in general, can be used as input parameters for *e.g.* plasma simulations, and on a more fundamental level for a better comprehension of the a-C:H surface chemistry, as well as in other fields, such as *e.g.* in interstellar space chemistry.

Regarding the *reaction behaviour* of the various investigated hydrocarbon species, several clear trends can be observed throughout the simulations, and the main outcomes of this work can be summarized as follows:

- The reaction mechanisms and the corresponding sticking coefficients of all species are site dependent;
- The surface reactivity in general is $C_2 > c\text{-}C_3 \geq c\text{-}C_3H > l\text{-}C_3$, C_2H, $CH > l\text{-}C_3H$;
- The impact angle has little or no effect on this sticking sequence in the investigated range 0^o to 45^o;
- The internal energy, distributed among the vibrational and rotational motion, on the other hand, has a considerable effect on the sticking behaviour, which is species dependent:
  - the sticking coefficients increase with increasing internal energy for l-C_3, c-C_3 and l-C_3H, while they decrease with increasing internal energy for CH, C_2H and c-C_3H. They remain constant for C_2;
  - when the species are given a higher internal energy, the reactivity sequence is changed as follows: C_2, l-C_3, $c\text{-}C_3 > l\text{-}C_3H$, $c\text{-}C_3H > C_2H >$ CH;
  - therefore, detailed knowledge regarding the internal energy of the reactive species is important input for MD simulations.
- Regarding the C_3 and C_3H species, the following conclusions can be drawn:

  - C_3 is more reactive than C_3H, due to steric hindrance of the H-atom.
  - c-C_3 and c-C_3H are always more reactive than their linear counterparts, resulting in higher sticking coefficients. This is caused by several factors:
    1. the cyclic species always have one reactive carbon atom more than their linear counterparts, due to their bonding configuration;
    2. the cyclic species are structurally less stable than their linear counterparts, resulting in a high break-up percentage upon impact, enhancing their sticking coefficients;
    3. the linear species have a fully bound central C-atom, inducing repulsive interaction with the surface; the cyclic C_3 species, on the other hand, do not have such a fully bound atom.

Besides elucidating the hydrocarbon surface reaction mechanisms, attention was also focussed on the *actual growth of thin a-C:H films.* In this respect, the main outcomes of this work can be summarized as follows:

- Early film growth simulations showed that C_2 and C_2H are major contributors to the growth, in agreement with the ETP $F < 1$ experiments. From these simulations, it was also clear that some additional H flux must also be incorporated in the growing film by some additional flux, in order to obtain the correct film stoichiometry.

- Also in agreement with the experiment, it was shown that C_4H_2 and C_6H_2 are of minor importance for the growth process.

- In correspondence to the literature, incoming H-atoms passivate dangling bonds at the growing surface, and dramatically increase the four-fold coordination. The simulations, however, show that this is possible without the formation of chain terminating segments.

- Films deposited from the C_3 and C_3H species alone (presumed to be the major growth species under ETP $F > 1$ conditions), invariably result in low-density films according to our simulations. The maximum film density is found for a 70/30 mixture of linear/cyclic species.
- The stoichiometry of the film is entirely determined by the sticking of the species, i.e., H-elimination does not occur.
- The H-uptake in the growing film is almost linearly dependent on the H-flux towards the substrate.
- Low additional H-fluxes can induce an increase in the film density. Higher H-fluxes lead to a lowering of the density. Under $F < 1$ conditions, a maximum in the mass density is found using a H-flux of about 10%. A maximum in the atom density is found at a H-flux of about 30%. The maximum mass density under $F > 1$ conditions is found at a H-flux of about 25%, coinciding with the maximum in the atom density. The changes in the density result from a H-induced phase shift in the film, converting sp^1 into sp^2 into sp^3 sites.
- An additional C-flux towards the substrate was found to further increase the mass density of the films.
- The sticking coefficients of the growth species are very much dependent on the actual H-content in the film.
- A lower density is found for the films deposited under $F > 1$ conditions as compared to the films deposited under $F < 1$ conditions, in contradiction with the experiment. This result suggests that, in view of the fact that good agreement was obtained under $F < 1$ conditions, one or several elements are still missing in the current model for $F > 1$ conditions.

Several possible reasons for this disagreement between simulation and experiments can be identified:

- Experimental fluxes (as used as input in this work) are subject to uncertainties [168];
- Possibly, other species might play a role in the deposition process under $F > 1$ conditions, which were not yet included in the model;
- On the other hand, a possible reason could also be the shortcomings of the Brenner potential as used in this work. For instance, it is known from the literature that the Brenner potential underestimates the sp^3 content of a-C:H films, possibly leading to an underestimation of the mass density.
- Ad-atom or any other type of diffusion between two impacts is not included in the MD model because of too long time scales. This also possibly influences the resulting film structure.

Nevertheless, it can be concluded that despite these shortcomings, many surface reaction mechanisms have already been identified and clarified. Also, a better understanding of the growth of thin a-C:H films from low-kinetic energy hydrocarbons is obtained.

Summary

The primary goal of this thesis was to investigate with molecular dynamics simulations the deposition characteristics of hydrocarbon radicals and the growth of thin amorphous hydrogenated carbon (a-C:H) films. More specifically, correspondence was sought between simulations on the one hand and experimental deposition of a-C:H films using the so-called expanding thermal plasma (ETP) on the other hand, which is the deposition technique developed at Eindhoven University of Technology. The results aimed for in this work, however, were not intended to be limited to the ETP set-up, but also to be applicable to other deposition sources, and hence be of a more general nature.

Since their first preparation, thin (hydrogenated) amorphous carbon films have been used in many applications, especially as protective coatings, but also for *e.g.* biomedical, tribological or electronic purposes. Although a lot of research has already been carried out to elucidate the growth of the films, to optimize the deposition process and to enhance the resulting film properties, a number of questions still remain. Indeed, the properties of the deposited film depend strongly on the deposition technique being used, and the exact depositions conditions. In this thesis, most of the attention has been focussed on the deposition characteristics of the so-called expanding thermal plasma (ETP) setup. In this setup, no substrate bias is applied, such that ions do not significantly contribute to growth, and hence growth of the films proceeds through chemisorption of low-energy radicals. Although the input data stem from ETP experiments, the results presented in this work are of a

more general nature, and can be applied to any source where low-energy radicals are responsible for growth. Several tendencies, trends and mechanisms have been elucidated for these conditions. This was accomplished using molecular dynamics simulations.

Molecular dynamics (MD) simulations have become a widespread tool to investigate atomic and molecular behaviour on the nm length scale and ns time scale. In an MD simulation, atoms are deterministically followed through space and time, integrating their equations of motion. The atoms can interact with each other according to the forces acting upon them, derived from an interatomic potential. The potential used in this work is the Brenner potential for hydrocarbons. The integration scheme used is the velocity-Verlet algorithm. The temperature was controlled using the Berendsen heat bath. Determination of reaction mechanisms, sticking coefficients, and thin layer growth, was accomplished by applying periodic boundaries in the ±x and ±y directions. More infomation about the simulation method can be found in Chapter 2.

The growth species in the simulations were determined from experimental data. These species were allowed to impinge on a substrate, where they can subsequently react. The surface reaction behaviour of the chosen radicals was investigated, on predefined substrates as in Chapter 5, on specific surface sites as in Chapter 4, as well as during growth, as in Chapters 3, 7 and 8. The results provide new insights into the exact deposition behaviour of the radicals. Their reaction mechanisms are explained in terms of their energies, chemical resonance, steric hindrance, the species structural stability, and surface dependent factors.

Second, growth of thin a-C:H films was also studied. Growth was accomplished by consecutive impacts of growth particles: the output from impact i is used as the input for impact $i+1$. Simulation of the growth of the films was continued until a desired thickness was reached. Film thicknesses in the range between 2.5 and 20 nm were obtained, requiring many thousands of particle impacts. It was established how film growth proceeds under different conditions. In the ETP source, it was elucidated that an important parameter determining the resulting type of film is the ratio between the flux of acetylene through the injection ring and the flux of Ar^+ ions emanating from the cascaded arc. This ratio F is therefore written:

$$F = \frac{\Phi_{C_2H_2}}{\Phi_{Ar^+}}$$

Simulations of thin film growth corresponding to experimental ETP conditions at $F < 1$ and $F > 1$, show how the different growth species lead to the formation of different films. Under $F < 1$ conditions, a good agreement with the experiment is obtained, in terms of the H-content, structure of the film and the density, as is illustrated in Chapter 3, and later in Chapter 7. Under $F > 1$ conditions, the agreement with the experiment was not so good, possibly indicating that one or several film determining factors were not yet included in the model. Consequently, simulations have also been carried out to investigate the influence of additional H- and C-fluxes towards the substrate (Chapter 8). It is found that these additional particle fluxes can induce a structural change in the film, leading to a densification of the film. This also yielded better agreement with experiment. Furthermore, these simulations also provide feedback information to the experiment regarding the H-uptake in the film, which could not be measured experimentally.

The general conclusion of this work is that each growth species contributes in its own distinctive way to growth of the film, each with its own reaction mechanisms, and as such co-determines the resulting film properties. Probably the most important conclusion of this work is that the simulations suggest that densification of a-C:H films can be accomplished without the use of a substrate bias, by applying an additional H- and/or C-flux towards the substrate. Therefore, exact knowledge of the species, their fluxes and their energies, are essential ingredients to optimize the deposition process.

Samenvatting

Het belangrijkste doel van dit doctoraatswerk was door middel van moleculaire dynamica simulaties een beter begrip te verkrijgen van de depositiekarakteristieken van koolwaterstof radicalen en de groei van dunne amorfe gehydrogeneerde koolstof (a-C:H) filmen. Meer specifiek werd overeenkomst gezocht tussen de simulaties en de experimentele depositie van dunne a-C:H filmen d.m.v. het zogenaamde expanderende thermische plasma (ETP), ontwikkeld aan de Technische Universiteit Eindhoven. De bekomen resultaten echter zijn niet gelimiteerd tot het ETP depositiesysteem, maar eveneens toepasbaar op andere depositie bronnen, en ze zijn dus van een meer algemene aard.

Dunne (gehydrogeneerde) amorfe koolstof filmen worden gebruikt in vele toepassingen, in het bijzonder als beschermende deklagen, maar eveneens voor bv. biomedische, tribologische en elektronische toepassingen. Hoewel reeds veel onderzoek verricht is om de groei van deze filmen te verduidelijken, het depositieproces te optimaliseren en de resulterende filmeigenschappen te verbeteren, blijven een aantal vragen vooralsnog onbeantwoord. Inderdaad, de eigenschappen van de afgezette film zijn sterk afhankelijk van de gebruikte depositietechniek, en de precieze depositie-omstandigheden. In dit werk kijken we vooral naar de depositiekarakteristieken van het zogeheten expanderende thermische plasma (ETP). In dit systeem wordt er geen substraat'bias' aangelegd, zodanig dat ionen nauwelijks bijdragen tot groei van de film, en de groei volledig gecontroleerd wordt door chemisorptie reacties van laag-energetische radicalen. Hoewel de input gegevens voor de simulaties afkomstig zijn van ETP experimenten, zijn de resultaten behaald in dit werk van een meer algemene aard, en kunnen ze toegepast worden op ieder depositiesysteem waarin laag-energetische radicalen verantwoordelijk zijn voor de groei van de film. Verscheidene tendensen, trends en mechanismen zijn opgehelderd voor deze groeivoorwaarden. Deze resultaten werden behaald door middel van moleculaire dynamica simulaties.

Moleculaire dynamica (MD) simulaties zijn een veelgebruikt instrument geworden om atomair en moleculair gedrag op nanometer lengteschaal en nanoseconde tijdsschaal te bestuderen. In een MD simulatie worden de atomen deterministisch gevolgd doorheen ruimte en tijd, door hun bewegingsvergelijkingen te integreren. De atomen kunnen met elkaar interageren door de krachten die op hen inwerken. Deze krachten zijn afgeleid van een interatomaire potentiaal. De potentiaal die gebruikt is in dit werk, is de Brenner potentiaal voor koolwaterstoffen. Het gebruikte integratieschema is het zgn. 'velocity-Verlet' algoritme. De temperatuur werd gecontroleerd dmv. het Berendsen warmtebad. Bepaling van de reactiemechanismen, sticking coëfficiënten en dunne film groei werd bereikt door periodische grenzen in de ± x en ± y richting aan te leggen. Meer informatie aangaande de simulatiemethode kan gevonden worden in hoofstuk 2.

De groeideeltjes in de simulaties werden bepaald a.d.h.v. experimentele data. Deze deeltjes vallen in de simulatie in op een substraat, waar ze vervolgens kunnen reageren. Het oppervlaktereactiegedrag van de gekozen radicalen is onderzocht, op voorafbepaalde substraten (hoofdstuk 5), op specifieke oppervlakte sites (hoofdstuk 4), alsook gedurende de groei (hoofdstukken 3,7 en 8). De resultaten geven nieuwe inzichten in het exacte depositieproces van de radicalen. Deze reactiemechanismen worden verklaard in termen van hun energie, chemische resonantie, sterische hinder, structurele stabiliteit, en oppervlakte-afhankelijke factoren.

Naast specifieke reactiemechanismen, is ook de groei zelf van dunne a-C:H filmen onderzocht. Groei werd verwezenlijkt door opeenvolgende impacts van groeideeltjes: het resultaat van impact i is de beginconfiguratie voor impact $i+1$. Simulatie van de groei van de filmen werd voortgezet totdat een gewenste dikte bereikt werd. Filmdiktes tussen 2.5 en 20 nm werden gesimuleerd, hetgeen de impact van duizenden deeltjes vereist. De simulaties hebben uitgewezen hoe de filmgroei tot stand komt onder verschillende omstandigheden. In de ETP bron is het experimenteel vastgesteld dat een belangrijke parameter voor de filmgroei de verhouding is tussen de acetyleen flux en de flux van de argon ionen uit de plasmabron. Deze verhouding F wordt gegeven door:

$$F = \frac{\Phi_{C_2H_2}}{\Phi_{Ar^+}}$$

Simulaties van filmgroei onder experimentele ETP voorwaarden voor $F < 1$ en $F > 1$, tonen hoe de verschillende groeideeltjes leiden tot de vorming van verschillende films. Onder $F < 1$ omstandigheden werd een bevredigende overeenkomst met het experiment bereikt in termen van de H-concentratie, de dichtheid en de structuur van de filmen (cfg. Hoofdstuk 3). Onder $F > 1$ voorwaarden was de overeenkomst met het experiment niet zo goed. Dit is mogelijkerwijze te wijten aan factoren die mede de film eigenschappen bepalen en die nog niet in het model zijn opgenomen. Simulaties zijn dan ook uitgevoerd om de invloed van bijkomende H- en C-fluxen naar het substraat te simuleren (Hoofdstuk 8). We hebben vastgesteld dat deze bijkomende deeltjesfluxen structurele veranderingen in de film kunnen induceren, hetgeen leidt tot een verdichting van de film. Dit leidde ook tot een betere overeenkomst met het experiment. Bovendien geven deze simulaties ook een terugkoppeling naar het experiment, in het bijzonder de H-flux naar het substraat, hetgeen experimenteel niet vastgesteld kon worden.

De algemene conclusie van dit werk is dat ieder groeideeltje bijdraagt op een eigen karakteristieke manier tot de groei van de film, met eigen reactiemechanismen, en als dusdanig mee de uiteindelijke filmeigenschappen bepaalt. Exacte kennis van de deeltjes, hun fluxen en hun energieën, zijn daarom essentiële ingrediënten om het depositieproces te optimalizeren. De belangrijkste conclusie van dit werk is wellicht dat verdichting van a-C:H films kan bereikt worden zonder een substaat'bias' aan te leggen, door middel van bijkomende H- en/of C-fluxen naar het substraat.

List of Publications

1. Neyts E., Bogaerts A., van de Sanden M.C.M., *Unraveling the deposition mechanism in a-C:H thin film growth: a Molecular Dynamics study for the reaction behaviour of* C_3 *and* C_3H *radicals with a-C:H surfaces*, J. Appl. Phys. **99**, 014902 (2006)

2. Bogaerts A., De Bleecker K., Georgieva V., Kolev I., Madani M., Neyts E., *Computer simulations for processing plasmas*, Plasma Process. Polym. **3**, 110 (2006)

3. Neyts E., Bogaerts A., Gijbels R., Benedikt J., van de Sanden M.C.M., *Molecular dynamics simulation of the impact behaviour of various hydrocarbon species on DLC*, NIMB **228**, 315 (2005)

4. Bogaerts A., De Bleecker K., Georgieve V., Herrebout D., Kolev I., Madani M., Neyts E., *Numerical modeling for a better understanding of gas discharge plasmas*, High Temp. Mater. Processes (New York) **9**, 321 (2005)

5. Neyts E., Bogaerts A., Gijbels R., Benedikt J., van de Sanden M.C.M., *Molecular dynamics simulations for the growth of diamond-like carbon films from low kinetic energy species*, Diam. Rel. Mat. **13**, 1873 (2004)

6. Neyts E., Yan M., Bogaerts A., Gijbels R., *Particle-in-cell/Monte Carlo simulations of a low-pressure capacitively coupled radio-frequency discharge: effect of adding* H_2 *to an Ar discharge*, J. Appl. Phys. **93**, 5025 (2003)

7. Neyts E., Yan M., Bogaerts A., Gijbels R., *PIC-MC simulation of an RF capacitively coupled* Ar/H_2 *discharge*, NIMB **202**, 300 (2003)

8. Bogaerts A., Neyts E., Gijbels R., van der Mullen J., *Gas discharge plasmas and their applications*, Spectrochim. Acta: Part B **57**, 609 (2002)

9. Liu Y., Neyts E., Bogaerts A., *Monte Carlo method for simulations of adsorbed atom diffusion on a surface*, Diam. Rel. Mat., Accepted for publication

10. Neyts E., Tacq M., Bogaerts A., *Reaction mechanisms of low-kinetic energy hydrocarbon radicals on typical hydrogenated amorphous carbon (a-C:H) sites: a Molecular Dynamics study*, Diam. Rel. Mat., *Submitted*

11. Neyts E., Bogaerts A., van de Sanden M.C.M., *Densification of thin a-C:H films grown from low-kinetic energy hydrocarbon radicals under the influence of H and C particle fluxes: a Molecular Dynamics study*, J. Phys. D: Appl. Phys., *Submitted*

12. Neyts E., Bogaerts A., van de Sanden M.C.M., *The effect of hydrogen on the growth of thin a-C:H films from thermal energy radicals*, Appl. Phys. Lett., *Submitted*

13. Neyts E., Bogaerts A., *Influence of internal energy and impact angle on the sticking behaviour of reactive radicals in thin a-C:H film growth: a molecular dynamics study*, Phys. Chem. Chem. Phys., *Submitted*

14. Neyts E., Bogaerts A., Gijbels R., Benedikt J., M. C. M. van de Sanden, *Molecular dynamics study of the growth mechanism of a-C:H layers deposited by an* Ar/C_2H_2 *expanding thermal plasma*, Proceedings of the XXVIIth ICPIG Conference, Eindhoven, The Netherlands, July 18-22, 2005

Contribution to conferences

1. Neyts E., Bogaerts A., Gijbels R., Benedikt J., van de Sanden M. C. M., *Molecular dynamics simulation of DLC growth for thermal expanding plasma conditions*, Oral presenation at the 'Summerschool of the Asociación Española del Vacio y sus Aplicaciones (ASEVA) on Reactive Plasmas: Physical and Chemical Processes in Reactive Hydrocarbon Plasmas in Contact with Surfaces', Avila, Spain, July 22-25, 2003
2. Benedikt J., R. V. Woen, van de Sanden M. C. M., Neyts E., Bogaerts A., *Plasma chemistry of* Ar/C_2H_2 *expanding thermal plasma*, Oral presenation at the 'Summerschool of the Asociación Española del Vacio y sus Aplicaciones (ASEVA) on Reactive Plasmas: Physical and Chemical Processes in Reactive Hydrocarbon Plasmas in Contact with Surfaces', Avila, Spain, July 22-25, 2003
3. Neyts E., Bogaerts A., Gijbels R., Benedikt J., van de Sanden M. C. M., *Growth of DLC layers using the ETP source: a quest for good growth precursors*, Oral presentation at the '7^th Workshop on the Exploration of Low Temperature Plasma Physics (WELTPP-7)', Kerkrade, The Netherlands, November 25-26, 2004
4. Bogaerts A., De Bleecker K., Georgieva V., Kolev I., Madani M., Neyts E., *Computer simulations for processing plasmas*, Invited Oral presentation at the 'Fourteenth International Summer School on Vacuum, Electron and Ion

Technologies (VEIT05)', Sunny Beach, Bulgaria, September 12-16, 2005

5. Neyts E., Bogaerts A., van de Sanden M. C. M., *Influence of H-content on the microstructure of thin a-C:H films: a Molecular Dynamics study* , Oral presentation at the '8^th Workshop on the Exploration of Low Temperature Plasma Physics (WELTPP-8)', Kerkrade, The Netherlands, November 24-25, 2005

6. Neyts E., Bogaerts A., Gijbels R., *Modelling of a low pressure capacitive RF discharge by a PIC-MCC simulation: effect of adding hydrogen to an argon discharge*, Poster presenation at the '6^th International Conference on Computer Simulation of Radiation Effects in Solids (COSIRES)', Dresden, Germany, June 23-27, 2002

7. Neyts E., Bogaerts A., Gijbels R., Benedikt J., van de Sanden M. C. M., *Molecular dynamics simulations of DLC deposition by a thermal expanding plasma*, Poster presentation at the '37^{th} International Union of Vacuum Science, Techniques and Applications Workshop on Plasma Deposition of Advanced Materials', Kerkrade, The Netherlands, September 14-18, 2003

8. Neyts E., Bogaerts A., Gijbels R., Benedikt J., Eijkman D. J., Vandamme W., van de Sanden M. C. M., *Molecular Dynamics studies to investigate possible growth precursors in the remote* Ar/C_2H_2 *plasma*, Poster presentation at the '7^th International Conference on Computer Simulation of Radiation Effects in Solids (COSIRES)', Helsinki, Finland, June 28 - July 2, 2004

9. Benedikt J., Eijkman D. J., Vandamme W., van de Sanden M. C. M., Agarwal S., Neyts E., Bogaerts A., *Hydrocarbon growth precursors in remote* Ar/C_2H_2 *plasma*, Poster presentation at the 'Gordon Research Conference: Plasma Processing Science', Plymouth, NH (USA), August 15-20, 2004

10. Neyts E., Bogaerts A., Gijbels R., Benedikt J., van de Sanden M. C. M.,

Molecular Dynamics study of the growth mechanism of a-C:H layers deposited by an Ar/C2H2 expanding thermal plasma, Poster presentation at the 'XXVII International Conference on Phenomena in Ionized Gases (ICPIG)', Eindhoven, The Netherlands, July 17-22, 2005

11. Titantah J. T., Lamoen D., Neyts E., Bogaerts A., *Density functional theory characterization of the bonding structure of hydrogenated and hydrogen-free amorphous carbon*, Poster presentation at the 'Ψ_k^{2005} conference', Schwäbisch Gmünd, Germany, September 17-21, 2005

Bibliography

[1] Jacob, W. and Moller, W. *Appl. Phys. Lett.* **63**, 1771 (1993).

[2] Robertson, J. *Mat. Sci. Eng. R* **37**, 129 (2002).

[3] Brenner, D. *Phys. Rev. B* **42**, 9458 (1990).

[4] Benedikt, J., Agarwal, S., Eijkman, D. J., Vandamme, W., Creatore, M., and van de Sanden, M. C. M. *J. Vac. Sci. Technol. A* **23**, 1400 (2005).

[5] Casiraghi, C., Piazza, F., Ferrari, A. C., Grambole, D., and Robertson, J. *Diam. Rel. Mat.* **14**, 1098 (2005).

[6] Koidl, P., Wagner, C., Dischler, B., Wagner, J., and Ramsteiner, M. *Mater. Sci. Forum* **52**, 41 (1990).

[7] Weiler, M., Sattel, S., Jung, K., Ehrhardt, H., Veerasamy, V. S., and Robertson, J. *Appl. Phys. Lett.* **64**, 2797 (1994).

[8] Robertson, J. *Adv. in Phys.* **35**, 317 (1986).

[9] Aisenberg, S. and Chabot, R. *J. Appl. Phys.* **42**, 2953 (1971).

[10] McKenzie, D. R. *Rep. Prog. Phys.* **59**, 1611 (1996).

[11] Lifshitz, Y. *Diam. Rel. Mat.* **5**, 388 (1996).

[12] Lifshitz, Y. *Diam. Rel. Mat.* **8**, 1659 (1999).

[13] Fallon, P. J., Veerasamy, V. S., Davis, C. A., Robertson, J., Amaratunga, G. A. J., Milne, W. I., and Koskinen, J. *Phys. Rev. B* **48**, 4777 (1993).

[14] Robertson, J. *Pure Appl. Chem.* **66**, 1789 (1994).

[15] Robertson, J. *Philos. Trans. R. Soc. London A* **342**, 277 (1993).

[16] Robertson, J. *Diam. Rel. Mat.* **3**, 361 (1994).

[17] Kaukonen, H. P. and Nieminen, R. M. *Phys. Rev. Lett.* **68**, 620 (1992).

[18] Kaukonen, H. P. and Nieminen, R. M. *Phys. Rev. B* **61**, 2806 (2000).

[19] Marks, N. A. *Phys. Rev. B* **56**, 2441 (1997).

[20] Uhlmann, S., Frauenheim, T., and Lifshitz, Y. *Phys. Rev. Lett.* **81**, 641 (1998).

[21] Catherine, Y. *Diamond and diamond-like carbon thin films.* NATO ASI 266, p. 193, (1991).

[22] Hopf, C., T. Schwarz-Sellinger, W. J., and von Keudell, A. *J. Appl. Phys.* **87**, 2719 (2000).

[23] von Keudell, A., Schwarz-Sellinger, T., and Jacob, W. *J. Appl. Phys.* **89**, 2979 (2001).

[24] von Keudell, A., Schwarz-Sellinger, T., and Jacob, W. *J. Vac. Sci. Technol. A* **19**, 101 (2001).

[25] Ugolini, D., Eitle, J., and Oelhafen, P. *Vacuum* **41**, 1374 (1990).

[26] Ugolini, D., Tuller, M. H., Eitle, J., Schelz, S., and Oelhafen, P. *Appl. Phys. A* **51**, 526 (1990).

[27] Dimigen, H. *Surf. Coatings Technol.* **49**, 453 (1991).

[28] Antilla, A., Lappalainen, R., Tiainen, V. M., and Hakovirta, M. *Acta Mater.* **9**, 1161 (1997).

[29] Erdemir, A., Eryilmaz, O. L., Nilufer, I. B., and Fenske, G. R. *Diam. Rel. Mat.* **9**, 632 (2000).

[30] Erdemir, A., Eryilmaz, O. L., and Fenske, G. R. *J. Vac. Sci. Technol. A* **18**, 1987 (2000).

[31] Fontaine, J., Belin, M., Mogne, T. L., and Grill, A. *Tribol. Int.* **37**, 869 (2004).

[32] Grill, A. *IBM J. Res. Develop.* **43**, 147 (1999).

[33] *Business Wire* April 18 (1998).

[34] Kimock, F. M. and Knapp, B. J. *Surf. Coatings Technol.* **56**, 273 (1993).

[35] Yang, P., Kwok, S. C. H., Fu, R. K. Y., Leng, Y. X., Wang, J., Wan, G. J., Huang, N., Leng, Y., and Chu, P. K. *Surf. Coatings Technol.* **177-178**, 747 (2004).

[36] Jones, M. I., McColl, I. R., Grant, D. M., Parker, K. G., and Parker, T. L. *Diam. Rel. Mat.* **8**, 457 (1999).

[37] Allen, M., Myer, B., and Rushton, N. *J. Biomed. Mater. Res.* **58**, 319 (2001).

[38] Liu, S., Lamp, D., Gangopadhyay, S., Sreenivas, G., Ang, S. S., and Naseem, H. A. *IEEE ED. Lett.* **19**, 317 (1998).

[39] McKenzie, D. R., Li, W. T., and Gerstner, E. G. *Diam. Rel. Mat.* **10**, 230 (2001).

[40] Druz, B., Zaritskiy, I., Yevtukhov, Y., Konchits, A., Valakh, M., Shanina, B., Kolesnik, S., Yanchuk, I., and Gromovoy, Y. *Diam. Rel. Mat.* **13**, 1592 (2004).

[41] Kaufmann, H. R. *J. Vac. Sci. Technol.* **15**, 272 (1978).

[42] Druz, B., Ostan, R., Distefano, S., Hayes, A., Kanarov, V., and Polyakov, V. *Diam. Rel. Mat.* **7**, 965 (1998).

[43] Ohno, H., van den Berg, J. A., Nagai, S., and Armour, D. G. *Nucl. Instr. and Meth. B* **148**, 673 (1999).

[44] Jansen, F., Mackonkin, M., Kaplan, S., and Hark, S. *J. Vac. Sci. Technol. A* **3**, 605 (1985).

[45] Logothetidis, S. *Appl. Phys. Lett.* **69**, 158 (1996).

[46] Ting, J. M. and Lee, H. *Diam. Rel. Mat.* **11**, 1119 (2002).

[47] Lacerda, R. G., Hammer, P., Jr., F. L. F., Alvarez, F., and Marques, F. C. *Diam. Rel. Mat.* **9**, 796 (2000).

[48] Ahmad, I., Roy, S. S., Maguire, P. D., Papakonstantinou, P., and McLaughlin, J. A. *Thin Solid Films* **482**, 45 (2005).

[49] Valentini, L., Kenny, J. M., Mariotto, G., and Tosi, P. *J. Mater. Sci.* **36**, 5295 (2001).

[50] Conway, N. M. J., Ferrari, A. C., Flewitt, A. J., Robertson, J., Milne, W. I., Tagliaferro, A., and Beyer, W. *Diam. Rel. Mat.* **9**, 765 (2000).

[51] Robertson, J. *Surf. Coatings Technol.* **50**, 185 (1992).

[52] Pramana, D. S., Ramachandran, K., Venkatramani, N., Pandey, M., and D'Cunha, R. *Pramana - J. Phys.* **55**, 933 (2000).

[53] Zhou, X. T., Lee, S. T., Bello, I., Cheung, A. C., Chiu, D. S., Lam, Y. W., Lee, C. S., and nd X. M. He, K. M. L. *Mat. Sci. Eng. B* **77**, 229 (2000).

[54] Martinu, L., Raveh, A., Boutard, D., Houle, S., and Wertheimer, M. *Diam. Rel. Mat.* **2**, 673 (1993).

[55] Zarrabian, M., Fourches-Coulon, N., and Turban, G. *Appl. Phys. Lett.* **70**, 2535 (1997).

[56] He, X. M., Lee, S., Bello, I., Cheung, A., Li, W., Chiu, D., Lam, Y., Lee, C., Leung, K., and Zhou, X. *J. Mater. Res.* **14**, 1617 (1999).

[57] Kroesen, G. M. W., Timmermans, C. J., and Schram, D. C. *Pure Appl. Chem.* **60**, 795 (1988).

[58] Gielen, J. W. A. M., van de Sanden, M. C. M., Kleuskens, P. R. M., and Schram, D. C. *Plasma Sources Sci. Technol.* **5**, 492 (1996).

[59] Gielen, J. W. A. M., van de Sanden, M. C. M., and Schram, D. C. *Appl. Phys. Lett.* **69**, 152 (1996).

[60] Gielen, J. W. A. M., Kleuskens, P. R. M., van de Sanden, M. C. M., van Ijzendoorn, L. J., Schram, D. C., Dekempeneer, E. H. A., and Meneve, J. *J. Appl. Phys.* **80**, 5986 (1996).

[61] Gielen, J. W. A. M., Kessels, W. M. M., van de Sanden, M. C. M., and Schram, D. C. *J. Appl. Phys.* **82**, 2643 (1997).

[62] Benedikt, J., Letourneur, K. G. Y., Wisse, M., Schram, D. C., and van de Sanden, M. C. M. *Diam. Rel. Mat.* **11**, 989 (2002).

[63] Benedikt, J., Woen, R. V., van Mensfoort, S. L. M., Perina, V., Hong, J., and van de Sanden, M. C. M. *Diam. Rel. Mat.* **12**, 90 (2003).

[64] Benedikt, J., Wisse, M., Woen, R. V., Engeln, R., and van de Sanden, M. C. M. *J. Appl. Phys.* **94**, 6932 (2003).

[65] Benedikt, J., Eijkman, D. J., Vandamme, W., Agarwal, S., and van de Sanden, M. C. M. *Chem. Phys. Lett.* **402**, 37 (2005).

[66] Philipps, V., Vietzke, E., and Flaskamp, K. *Surf. Sci.* **178**, 806 (1986).

[67] Blaudeck, P., Frauenheim, T., Jungnickel, G., and Stephan, U. *Solid State Commun.* **85**, 997 (1993).

[68] Iarlori, S., Galli, G., and Martini, O. *Phys. Rev. B* **49**, 7060 (1994).

[69] Jungnickel, G., Kohler, T., Frauenheim, T., Haase, M., Blaudeck, P., and Stephan, U. *Diam. Rel. Mat.* **5**, 175 (1996).

[70] Bilek, M. M. M., McKenzie, D. R., McCulloch, D. G., and Goringe, C. M. *Phys. Rev. B* **62**, 3071 (2000).

[71] Galli, G., Martin, R. M., Car, R., and Parrinello, M. *Phys. Rev. Lett.* **62**, 555 (1989).

[72] Marks, N., McKenzie, D., Pailthorpe, B., Bernasconi, M., and Parinello, M. *Phys. Rev. B* **54**, 9703 (1996).

[73] McCulloch, D. G., McKenzie, D. R., and Goringe, C. M. *Phys. Rev. B* **61**, 2349 (2000).

[74] Uhlmann, S. and Frauenheim, T. *Diam. Rel. Mat.* **5**, 169 (1995).

[75] Kohary, K., Kugler, S., and Lazlo, I. *J. Non-Cryst. Solids* **227-230**, 594 (1998).

[76] Kohary, K. and Kugler, S. *Phys. Rev. B* **63**, 193404 (2001).

[77] Kohary, K., Kugler, S., and Lazlo, I. *J. Non-Cryst. Solids* **299-302**, 824 (2002).

[78] Cooper, N. C., Fagan, M. S., Goringe, C. M., Marks, N. A., and McKenzie, D. R. *J. Phys.: Condens. Matter* **14**, 723 (2002).

[79] Belov, A. Y. *Comput. Mater. Sci.* **27**, 30 (2003).

[80] Jäger, H. U. and Albe, K. *J. Appl. Phys.* **88**, 1129 (2000).

[81] Belov, A. Y. and Jäger, H. U. *Diam. Rel. Mat.* **14**, 1014 (2005).

[82] Belov, A. Y. and Jäger, H. U. *Thin Solid Films* **482**, 74 (2005).

[83] Belov, A. Y. and Jäger, H. U. *Comput. Mater. Sci.* **27**, 16 (2003).

[84] Jäger, H. U. and Belov, A. Y. *Phys. Rev. B* **68**, 024201 (2003).

[85] Belov, A. Y. and Jäger, H. U. *Mat. Res. Soc. Symp. Proc.* **648**, 6.53.1 (2001).

[86] Jäger, H. U. and Weiler, M. *Diam. Rel. Mat.* **7**, 858 (1998).

[87] Marks, N. A., Bell, J. M., Pearce, G. K., McKenzie, D. R., and Bilek, M. M. M. *Diam. Rel. Mat.* **12**, 2003 (2003).

[88] Marks, N. A. *Diam. Rel. Mat.* **14**, 1223 (2005).

[89] Marks, N. A. *J. Phys.: Condens. Matter* **14**, 2901 (2002).

[90] Marks, N. A. *Phys. Rev. B* **63**, 035401 (2000).

[91] Plaisted, T. A. and Sinnott, S. B. *J. Vac. Sci. Technol. A* **19**, 262 (2001).

[92] Zoppi, L., Colombo, L., and Donadio, D. *Eur. Phys. J. B* **27**, 335 (2002).

[93] Plaisted, T. A., Ni, B., Zahrt, J. D., and Sinnott, S. B. *Thin Solid Films* **381**, 73 (2001).

[94] Halac, E. B., Reinoso, M., Dall'Asen, A. G., and Burgos, E. *Phys. Rev. B* **71**, 115431 (2005).

[95] Gao, G. T., Mikulski, P. T., Chateauneuf, G. M., and Harrison, J. A. *J. Phys. Chem. B* **107**, 11082 (2003).

[96] Lee, S.-H., Lee, C.-S., Lee, S.-C., and Lee, K.-R. *Surf. Coatings Technol.* **177-178**, 812 (2004).

[97] Sinnott, S. B., Colton, R. J., White, C. T., Shenderova, O. A., Brenner, D. W., and Harrison, J. A. *J. Vac. Sci. Technol. A* **15**, 936 (1997).

[98] Pearce, G. K., Marks, N. A., McKenzie, D. R., and Bilek, M. M. M. *Diam. Rel. Mat.* **14**, 921 (2005).

[99] Zhang, S., Wagner, G., Medyanik, S. N., Liu, W.-K., Yu, Y.-H., and Chung, Y.-W. *Surf. Coatings Technol.* **177-178**, 818 (2004).

[100] Gago, R., Vinnichenko, M., Jäger, H. U., Belov, A. Y., Jimenez, I., Huang, N., Sun, H., and Maitz, M. F. *Phys. Rev. B* **72**, 014120 (2005).

[101] Garrison, B. J., Dawnkaski, E. J., Srivastava, D., and Brenner, D. W. *Science* **255**, 835 (1992).

[102] Träskelin, P., Salonen, E., Nordlund, K., Kraheninnikov, A. V., and Wu, C. H. *J. Appl. Phys.* **93**, 1826 (2003).

[103] Perry, M. D. and Raff, L. M. *J. Phys. Chem.* **98**, 8128 (1994).

[104] Perry, M. D. and Raff, L. M. *J. Phys. Chem.* **98**, 4375 (1994).

[105] Voter, A. F., Montalenti, F., and Germann, T. C. *Annu. Rev. Mater. Res.* **32**, 321 (2002).

[106] Voter, A. F. *Phys. Rev. Lett.* **78**, 3908 (1997).

[107] Voter, A. F. *J. Chem. Phys.* **106**, 4665 (1997).

[108] Miyagawa, Y., Nakadate, N., Ikeyama, M., Nakao, S., and Miyagawa, S. *Diam. Rel. Mat.* **12**, 927 (2003).

[109] Patsalas, P., Logothetidis, S., and Kelires, P. C. *Diam. Rel. Mat.* **14**, 1241 (2005).

[110] Xing, J. and Scott, H. L. *Phys. Rev. B* **48**, 4806 (1993).

[111] Battaile, C. C., Srolovitz, D. J., and Butler, J. E. *J. Appl. Phys.* **82**, 6293 (1997).

[112] Dawnkaski, E. J., Srivastava, D., and Garrison, B. J. *J. Chem. Phys.* **102**, 9401 (1995).

[113] Dawnkaski, E. J., Srivastava, D., and Garrison, B. J. *Chem. Phys. Lett.* **232**, 524 (1995).

[114] Johnson, M. D., Caturla, M.-J., and de la Rubia, T. D. *J. Appl. Phys.* **84**, 1963 (1998).

[115] Kaukonen, M., Perajoki, J., Nieminen, R. M., Jungnickel, G., and Frauenheim, T. *Phys. Rev. B* **61**, 980 (2000).

[116] Mousseau, N. and Barkema, G. T. *Phys. Rev. B* **61**, 1898 (2000).

[117] Barkema, G. T. and Mousseau, N. *Phys. Rev. Lett.* **77**, 4358 (1996).

[118] Mousseau, N. and Barkema, G. T. *Phys. Rev. E* **57**, 2419 (1998).

[119] Ercolessi, F. Spring College in Computational Physics, Trieste, june 1997.

[120] Tolman, R. C. *Principles of Statistical Mechanics.* Dover Publications, (1979).

[121] Rapaport, D. C. *The art of molecular dynamics simulation.* Cambridge University Press, (2002).

[122] Brenner, D. W. *Phys. Stat. Sol. B* **217**, 23 (2000).

[123] Heermann, D. W. *Computer simulation methods.* Springer, (1986).

[124] Daw, M. S. and Baskes, M. I. *Phys. Rev. Lett.* **50**, 285 (1983).

[125] Stuart, S. J., Tutein, A. B., and Harrison, J. A. *J. Chem. Phys.* **112**, 6472 (2000).

[126] Liew, K. M., Wong, C. H., and Tan, M. J. *Acta Mater.* **54**, 225 (2006).

[127] Mielke, S. L., Troya, D., Zhang, S., Li, J.-L., Xiao, S., Car, R., Ruoff, R. S., Schatz, G. C., and Belytschko, T. *Chem. Phys. Lett.* **390**, 413 (2004).

[128] Swope, W. C., Anderson, H. C., Berens, P. H., and Wilson, K. R. *J. Chem. Phys.* **76**, 637 (1982).

[129] Allen, M. P. and Tildesley, D. J. *Computer Simulation of Liquids.* New York: Oxford University Press, (1987).

[130] Nordlund, K. Lecture notes "introduction to atomistic simulations", University of Helsinki, 2003.

[131] Berendsen, H. J. C., Postma, J. P. M., van Gunsteren, W. F., DiNola, A., and Haak, J. R. *J. Chem. Phys.* **81**, 3684 (1984).

[132] Paci, E. and Marchi, M. *J. Chem. Phys.* **100**, 4314 (1996).

[133] Cheng, A. and Jr., K. M. M. *J. Chem. Phys.* **100**, 1927 (1996).

[134] Morishita, T. *J. Chem. Phys.* **113**, 2982 (2000).

[135] Ferrante, J., Smith, J., and Rose, J. *Phys. Rev. Lett.* **50**, 1385 (1983).

[136] Abell, G. *Phys. Rev. B* **31**, 6184 (1985).

[137] Tersoff, J. *Phys. Rev. Lett.* **56**, 632 (1986).

[138] Tersoff, J. *Phys. Rev. B* **37**, 6991 (1988).

[139] Tersoff, J. *Phys. Rev. Lett.* **61**, 2879 (1988).

[140] Brenner, D. *Phys. Rev. B* **46**, 1948 (1992).

[141] Abrams, C. private communication .

[142] Murty, M. V. R. and Atwater, H. A. *Phys. Rev. B* **51**, 4889 (1995).

[143] Herzberg, G. and Johns, J. W. C. *J. Chem. Phys.* **54**, 2276 (1971).

[144] Wasserman, E., Kuck, V. J., Hutton, R. S., Anderson, E. D., and Yager, W. A. *J. Chem. Phys.* **54**, 4120 (1971).

[145] Beardmore, K. and Smith, R. *Phil. Mag. A* **74**, 1439 (1996).

[146] Molière, G. *Z. Naturforsch. A* **2**, 133 (1947).

[147] Yastrebov, S. and Smith, R. *Nucl. Instr. and Meth. B* **180**, 145 (2001).

[148] Nordlund, K., Keikonen, J., and Mattila, T. *Phys. Rev. Lett.* **77**, 699 (1996).

[149] Brenner, D. W., Shenderova, O. A., Harrison, J. A., Stuart, S. J., Ni, B., and Sinnott, S. B. *J. Phys.: Condens. Matter* **14**, 783 (2002).

[150] Smith, R. and Beardmore, K. *Thin Solid Films* **272**, 255 (1996).

[151] Nyden, M. R., Coley, R. R., and Mumby, S. *Polym. Eng. Sci.* **37**, 1496 (1997).

[152] Che, J. W., Çağin, T., and Goddard, W. A. *Theor. Chem. Acc.* **102**, 346 (1999).

[153] Stillinger, F. H. and Weber, T. A. *Phys. Rev. B* **31**, 5262 (1985).

[154] Lee, B.-J. and Lee, J. W. *Calphad* **29**, 7 (2005).

[155] Press, W. H., Teukolsky, S. A., Vetterling, W. T., and Flannery, B., editors. *Numerical Recipes in C.* Cambridge University Press, (1992).

[156] Abrams, C. private communication .

[157] Merritt, E. A. and Bacon, D. J. *Meth. Enzymol.* **277**, 505 (1997).

[158] Serikov, V., Kawamoto, S., Abrams, C., and Graves, D. APS Proceedings of the 22nd Symposium on Rarefied Gas Dynamics, Sydney 2000.

[159] Benedikt, J. private communication .

[160] Hamon, A.-L., Verbeeck, J., Schryvers, D., Benedikt, J., and van den Sanden, M. *J. Mater. Sci.* **14**, 2030 (2004).

[161] Ruzic, D. N. and Alman, D. A. presentation at the 10th International Workshop on Carbon Materials for Fusion Application, Jülich, Germany, 17-19 september 2003.

[162] Tsai, D.-S., Chang, T.-C., Hsin, W.-C., Hamamura, H., and Shimogaki, Y. *Thin Solid Films* **411**, 177 (2002).

[163] Nelson, H. H., Helvajian, H., Pasternack, L., and McDonald, J. R. *Chem. Phys.* **73**, 431 (1982).

[164] Yamagishi, H., Taiko, H., Shimogawara, S., Murakami, A., Noro, T., and Tanaka, K. *Chem. Phys. Lett.* **250**, 165 (1996).

[165] Som, T., Malhotra, M., Kulkarni, V. N., and Kumar, S. *Physica B* **355**, 72 (2005).

[166] Ferrari, A. C., Libassi, A., Tanner, B. K., Stolojan, V., Yuan, J., Brown, L. M., Rodil, S. E., Kleinsorge, B., and Robertson, J. *Phys. Rev. B* **62**, 11089 (2000).

[167] Findeisen, E., Feidenhans, R., Vigild, M. E., Clausen, K. N., Hansen, J. B., Bentzon, M. D., and Goff, J. P. *J. Appl. Phys.* **76**, 4636 (1994).

[168] Benedikt, J. Ph.D. thesis, Eindhoven University of Technology, 2004.